LASER-ACTIVATED PERFLUOROCARBON NANODROPLETS AS A TOOL IN NEUROLOGICAL APPLICATIONS

A Dissertation
Presented to
The Academic Faculty

by

Kristina Alexandra Hallam

In Partial Fulfillment
of the Requirements for the Degree
Doctor of Philosophy in the
Wallace H. Coulter Department of Biomedical Engineering

Georgia Institute of Technology
Emory University
May 2020

COPYRIGHT © 2020 BY KRISTINA ALEXANDRA HALLAM

LASER-ACTIVATED PERFLUOROCARBON NANODROPLETS AS A TOOL IN NEUROLOGICAL APPLICATIONS

Approved by:

Dr. Stanislav Emelianov, Advisor
School of Electrical and Computer Engineering, Wallace H. Coulter Department of Biomedical Engineering
Georgia Institute of Technology and Emory University School of Medicine

Dr. Ravi Kane
School of Chemical & Biomolecular Engineering, Wallace H. Coulter Department of Biomedical Engineering
Georgia Institute of Technology and Emory University School of Medicine Georgia Institute of Technology

Dr. Costas Arvanitis
The George W. Woodruff School of Mechanical Engineering, Wallace H. Coulter Department of Biomedical Engineering
Georgia Institute of Technology and Emory University School of Medicine

Dr. Hui Mao
Department of Radiology and Imaging Sciences, Wallace H. Coulter Department of Biomedical Engineering
Emory University School of Medicine and Georgia Institute of Technology

Dr. Eleanor Barber
The Graduate Entry Medical School
University of Limerick

Dr. Levi Wood
The George W. Woodruff School of Mechanical Engineering, Wallace H. Coulter Department of Biomedical Engineering
Georgia Institute of Technology and Emory University School of Medicine

Date Approved: November 25, 2019

To my parents for their unwavering support and encouragement

ACKNOWLEDGEMENTS

First and foremost, I would like to thank my family. My parents have been a driving force, encouraging me and supporting me, emotionally and financially, throughout this entire process. I would not here today without them. I would also like to thank my sisters, Katy and Kara, and my brother-in-law Jeremy for their support as well as their curiosity and enthusiasm of my pursuits in science. I would also like to thank my college friend and APO brother Tammy Kim for her help reviewing my dissertation. Finally, I would also like to thank the fluffy members of my family, Kandi, Kosmo, Gundy, Kash, and especially my dog-daughter Luna Rey for their constant friendliness and positivity that always made any day better.

I would like to thank my advisor, Stas, for all his support throughout this process. His commitment to his students provided us with so many opportunities to develop as researchers and as people. I sincerely appreciate his mentorship and his understanding over the last six years. I would also like to thank my committee members, Dr. Arvanitis, Dr. Kane, Dr. Mao, Dr. Wood, and Dr. Barber for their insight, enthusiasm, and extremely valuable feedback. I would especially like to thank Dr. Barber for her mentorship, encouragement, and support over the past three years.

I also wish to thank many lab members, past and present, who have been helpful and supportive. Alex Hannah was key to helping me understand the principles and concepts of laser-activated perfluorocarbon nanodroplets, a main component of my dissertation. Robin Hartman taught me much about ultrasound and photoacoustic delivery and imaging in the CNS, the main area of which my research studies were focused. Without these two

helpful and encouraging lab members, my progress and research would be severely lacking. I would also like to thank Daniela Santiesteban for her positivity and thoughtfulness as a lab member and co-collaborator. I would like to thank Heechul Yoon and Diego Dumani for their helpfulness with any issue that I would come across. I would especially like to thank my lab twin, Kelsey Kubelick, who has started and ended this process with me. I would like to thank current lab members Steve Yarmoska, Andrew Zhao, Tim Sowers, Yiying Zhu, Jinfei Liu, Andrei Karpiouk, Anthony Yu, and Brandyn Orr for their collaboration, help, and support. I would also like to thank all current and past lab members of the Ultrasound Imaging and Therapeutics Laboratory who have worked to create a helpful and creative lab environment. Thanks also to all of my undergraduate students and especially to Davis Palmie who worked hard and was enthusiastic to learn and help with my research endeavors.

Additionally, I would like to thank the Georgia Tech staff who were extremely helpful throughout this process. I would to thank Andrew Shaw at the microcopy core for his willingness to train and help me capture the best microscopy images. I would also like to thank Dr. Noel, Dr. O'Farrell, and the staff at the PRL. Their helpfulness and willingness to answer any question is greatly appreciated.

Finally, I would like to thank God for the opportunities I have been given, for the ability to pursue biomedical research, and for making any of this possible.

TABLE OF CONTENTS

LIST OF FIGURES

LIST OF SYMBOLS AND ABBREVIATIONS

ADV	Acoustic droplet vaporization
ALS	Amyotrophic lateral sclerosis
AuNR	Gold nanorod
BBB	Blood brain barrier
BSCB	Blood spinal cord barrier
CNS	Central nervous system
CuS	Copper Sulfide
Da	Daltons
DAPI	4',6-diamidino-2-phenylindole
DSPC	1,2-distearoyl-sn-glycero-3-phosphocholine
DSPE	1,2-distearoyl-sn-glycero-3-phosphoethanolamine
EB	Evans Blue
FUS	Focused ultrasound
H&E	Hematoxylin and eosin
IBA1	Ionized calcium-binding adapter molecule 1
IgG	Immunoglobulin G
IHC	Immunohistochemistry
IP	Intraperitoneal
IPA	Isopropyl alcohol
MRI	Magnetic resonance imaging
NA	Numerical aperture
Nd:YAG	Neodymium-doped yttrium aluminum garnet

NIR	Near infrared
NP	Nanoparticle
OD	Optical density
PA	Photoacoustic
PBS	Phosphate buffered saline
PET	Positron emission tomography
PFA	Paraformaldehyde
PFCnD	Perfluorocarbon nanodroplet
PFH	Perfluorohexane
PFP	Perfluoropentane
PLL	Poly-L-lysine
PRF	Pulse repetition frequency
RBC	Red blood cell
ROI	Region of interest
US	Ultrasound
US/PA	Ultrasound and photoacoustic
UV	Ultra-violet
ΔUS	Ultrasound difference signal

SUMMARY

Perfluorocarbon nanodroplets (PFCnDs) are an emerging class of nanoagents for biomedical applications. These nanoparticles are unique in their ability to phase change from liquid nanodroplet to gas microbubble when activated by electromagnetic energy. The ability of PFCnDs to phase change when triggered via an energy source has been utilized widely in the field of ultrasound (US) imaging and therapy. Upon phase change from a liquid nanodroplet to a gas microbubble by an ultrasound pulse, PFCnDs can provide US imaging contrast and can act as delivery vehicles for various types of cargo. PFCnDs used in US therapy have also been employed to act as mechanical agents, creating pores in cell membranes and interrogating biological barriers. Recently, laser-activated PFCnDs have been investigated. This subset of PFCnDs are vaporized optically and require a highly absorbing optical trigger contained within the droplet to induce phase change. The dual ultrasound and photoacoustic (PA) imaging contrast inherently provided by laser-activated PFCnDs is used in a variety of imaging techniques, from super-resolution imaging to molecular and functional imaging. In addition, applications of laser-activated PFCnDs as a therapeutic agent are currently being explored.

Due to their versatile nature and dual imaging contrast, laser-activated PFCnDs present themselves as a promising biomedical imaging and therapy tool. In particular, laser-activated PFCnDs can be used to address certain challenges involved in treating diseases and disorders of the central nervous system (CNS). One major roadblock to successful treatment of neurological diseases is the blood brain barrier (BBB), a semipermeable barrier that often prevents extravasation of therapeutics or imaging contrast

from the vasculature into brain tissue. To address this challenge, laser-activated PFCnDs can be developed as mechanical agents, to open the BBB noninvasively. Furthermore, laser-activated PFCnD US/PA imaging contrast can also be utilized for *in vivo* neuroimaging techniques. Therefore, the goal of this work is to develop laser-activated PFCnDs as a tool in neurological applications, ranging from opening biological barriers to providing US/PA imaging contrast within the CNS.

Specifically, PFCnDs are synthesized to open the BBB and are evaluated qualitatively, histologically, and through US/PA imaging techniques. In addition, laser parameters used to trigger PFCnD vaporization are optimized to ensure safe and effective laser-activated PFCnD induced BBB opening. Laser-activated PFCnDs are also evaluated as a US/PA neuroimaging contrast agent through *in vitro* and *in vivo* studies. Overall, the results of these studies showcase the far-reaching capabilities of laser-activated PFCnDs in neurological applications.

CHAPTER 1. INTRODUCTION

1.1 Current challenges in treatment and monitoring of neurological diseases

Diseases and disorders of the central nervous system present a unique set of challenges to researchers and clinicians when it comes to diagnosis, imaging, and therapy. One challenge of the CNS is the protective layer of bone surrounding the brain [1]. As a result, imaging of the CNS is limited to modalities such as MRI, PET, and fluorescence imaging [1-3]. Although these techniques provide insight, they still have limitations. MRI is costly, bulky, and requires dual imaging with a modality like PET, which uses ionizing radiation, to obtain both functional and anatomical information [2]. Fluorescence imaging is limited to depths of about 1 mm and requires an invasive optical window to enable visualization of the tissue, thus limiting its utility in whole brain imaging [3]. Not only does the skull make imaging a challenge, but it also creates difficulties during treatment. Localized treatments often require direct injections or incisions into the brain [4]. To perform these treatments, portions of the skull must be removed to reach the tissue [1, 4-6]. As a result, these treatments are invasive and create the possibility for infection to occur post-surgery [5, 6]. Furthermore, if re-treatment is needed, bone may need to be removed again, creating further complications [6].

In addition to the complications caused by the skull when treating diseases of the brain, there is also a physiological barrier that prevents successful monitoring and therapy of the brain. The blood brain barrier (BBB) is a physiological barrier that prevents noninvasive delivery of therapeutics to the brain and imaging of contrast agents in the brain [4-7]. This biological barrier can be described as a non-permeable barrier that limits the

access of molecules into the cells of the brain [4, 8]. It consists of endothelial cells connected by tight junctions that prevent the passage of large molecules. The function of the BBB is to prevent toxins and pathogens from entering the brain tissue [9]. Although toxin blockage is desirable, the barrier creates a challenge for therapeutic drugs intended to treat diseases that occur in the brain. Since only small molecule drugs with molecular weights under 500 Daltons (Da) can pass through the barrier in therapeutic amounts, the range of treatable diseases is limited [5, 9, 10]. Furthermore, the application of contrast agents in the CNS has also been limited due to their size [4, 10]. To address these challenges, there have been many approaches to opening the BBB, including biopharmaceutical methods and invasive procedures [5]. As aforementioned, invasive procedures often require the removal of bone to enable direct injections or incisions into the tissue, leaving the body vulnerable to infection [4]. Biopharmaceutical methods like mannitol enable noninvasive opening, however, their effects are not local but widespread [8]. As a result, there is a need for a more efficient method of noninvasive neurological treatment and monitoring.

1.2 Noninvasive blood brain barrier opening using focused ultrasound

A noninvasive method that has been recently developed to overcome these challenges is microbubble assisted focused ultrasound (FUS) opening of the BBB [11]. FUS enables transient opening of the BBB by geometrically targeting a localized area of the tissue for opening [9]. A focused ultrasound pulse, in conjunction with microbubbles, can be used to temporarily permeabilize the BBB, allowing for transport of larger molecules across the barrier [4, 11]. While the mechanisms of this disruption are not fully understood, it is hypothesized that the interaction between oscillating microbubbles and

the endothelial tight junctions results in stretching of tight junctions and an increase in uptake of larger molecules through mechanotransduction pathways [9, 12]. This method of focused ultrasound is often described as therapeutic ultrasound, as it is typically lower in frequency, higher in intensity, and composed of longer pulses in comparison to ultrasound for medical imaging [13, 14]. Furthermore, microbubble assisted FUS is categorized as non-thermal therapeutic ultrasound, which is characterized by acoustic cavitation, i.e., the formation, growth, and collapse of gas bubbles [13, 14].

Microbubble assisted FUS for BBB opening is a technique that has been evaluated for safety and efficacy [15-18]. FUS frequency, pulse duration, pulse repetition frequency (PRF), and pressure amplitude, as well as microbubble composition and dose have been examined to determine the optimal range of parameters [10, 19-26]. Consequently, this technology is used in applications ranging from small animal studies to clinical trials [27, 28]. As such, microbubble assisted FUS BBB opening has the potential to treat various neurological disorders such as Alzheimer's, ALS, Huntington's, stroke, and Parkinson's [29].

Although FUS opening of the BBB has made great progress, the approach is limited in its use of microbubbles. Microbubbles are micrometer sized gas bubbles typically made of a perfluorocarbon gas and a lipid shell [29]. These particles are used widely as an ultrasonic contrast agent because the gas core of the bubble provides strong ultrasound contrast. However, microbubbles have short circulation times, which makes it difficult to use these bubbles for an extended FUS opening or imaging session [30]. Furthermore, their micrometer size prevents them from leaving the vasculature, which also limits their use to the circulatory system. Given their gas core, microbubbles cannot encapsulate any sort of

cargo, making them less efficient drug carriers. Overall, they are capable of opening biological barriers and providing intravascular contrast but otherwise do not perform any other tasks for the CNS.

1.3 Ultrasound imaging and applications in the brain

Ultrasound (US) imaging is a widely used imaging modality in clinical applications due to its low-cost, portability, and safe use of non-ionizing radiation [31]. US imaging of tissue is achieved by sending and receiving acoustic waves, with the resulting interaction of the waves and tissue providing an anatomical map. Ultrasound irradiates tissue with high-frequency sound waves, above 20 kHz. The images that are generated using ultrasound are dependent upon the properties of the tissue, defined by acoustic impedance [31]. Acoustic impedance (Z) is described by the density of the tissue (ρ, kg/m^3) and the speed of sound of the tissue (c, m/s) as shown in (1).

$$Z = \rho \cdot c \tag{1}$$

When ultrasound is transmitted and interacts with tissue, the portion of the ultrasound wave reflected back and the resulting portion that is scattered or continues to propagate is proportional to the difference in acoustic impedance between the two materials. Larger acoustic impedance mismatches result in a higher percentage of reflected ultrasound waves and appear brighter on grayscale images. Bone, for example, has an acoustic impedance of 7.75 kg/(s·m^2) whereas brain tissue has an acoustic impedance of 1.60 kg/(s·m^2) [32], resulting in a large impedance mismatch between the skull and brain. Additionally, the attenuation coefficient, used to describe the amplitude loss of propagating

ultrasound waves through a medium, of bone is also high, resulting in many challenges when it comes to employing ultrasound as a neuroimaging modality [32].

Currently, ultrasound imaging of the brain has been limited due to the acoustic characteristics of the skull. Common clinical neuroimaging methods rely on imaging situations where skull interference is reduced. For example, prenatal and pediatric imaging is capable of US imaging due to the open space in the fontanel prior to hardening [33-37]. Transcranial Doppler is also capable of capturing signal through the thinner temporal bone to evaluate concussions or traumatic brain injury [36, 38-41]. Additionally, when cranial windows are employed and the skull is partially removed, invasive ultrasound imaging can be employed [42]. Despite these current limitations, pre-clinical studies are exploring ways to improve ultrasound brain imaging: by reducing ultrasound probe size for implantation, by developing improved US beamforming techniques, and by optimizing ultrasound imaging for guidance during neurosurgery [43, 44].

1.4 Photoacoustic imaging and applications in the brain

Photoacoustic (PA) imaging is an established imaging method based on properties of light and sound. PA imaging uses light to interrogate a target of interest. The irradiated region absorbs light and subsequently undergoes thermal expansion which produces transient photoacoustic waves [45, 46]. The produced acoustic wave is localized and dependent on the optical properties of the irradiated volume. The resulting acoustic pressure wave (2) can be described by the optical absorption coefficient of the irradiated target (μ_a, cm^{-1}), the light fluence (F, J/cm^2), and the Grüneisen parameter (Γ), which is a

temperature dependent variable that accounts for volume expansion, specific heat, and the speed of sound [47]. That is,

$$p_0 = \mu_a \cdot F \cdot \Gamma \tag{2}$$

Because of the dependence of the photoacoustic wave on the absorption properties and light fluence used to irradiate a material of interest, medical photoacoustic imaging is contingent upon the optical properties of tissue. To reduce scattering and increase depth penetration into the tissue, light in the near-infrared (NIR) range is used (Figure 1) [48]. This comprises of wavelengths between 600-1200 nm and allows for PA imaging of endogenous absorbers of the tissue as well as exogenous absorbers, i.e., PA contrast agents [49].

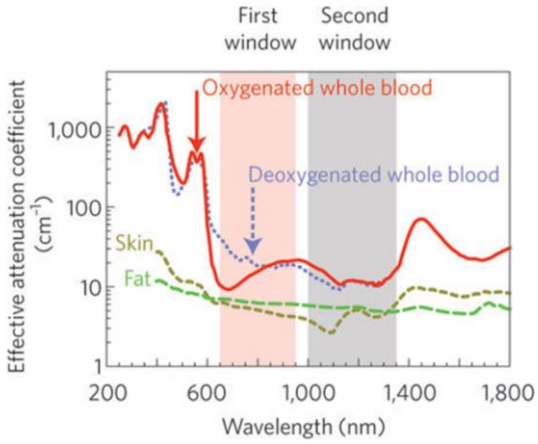

Figure 1. The first and second optical windows, NIR-I and NIR-II provide optimal wavelengths for *in vivo* photoacoustic imaging [49].

Photoacoustic imaging of endogenous absorbers such as deoxygenated and oxygenated blood, melanin, and fat can provide important functional information without

the need for additional contrast. By tuning the wavelength of light used to optimize for a specific endogenous absorbers' optical spectrum, PA imaging can collect relevant information about physiological properties such as oxygen saturation or skin cancer [50, 51]. Although endogenous absorbers can help to uncover biological properties, exogenous photoabsorbers can be employed to further enhance contrast and allow for more advanced diagnostic imaging [52]. Exogenous contrast agents typically include dyes and nanoparticles (NPs) [52, 53]. There are a wide variety of NPs which are capable of being synthesized in various sizes with surface modifications and functionalized for molecularly specific imaging [54, 55]. By altering nanoparticle size and shape, NPs can often be synthesized at a specific wavelength to optimize their PA contrast while reducing contrast caused by background endogenous absorbers [47]. In addition, PA imaging has the capability to image and identify multiple distinct photoabsorbers at once. This process is performed by analyzing acoustic waves received at various excitation wavelengths followed by spectral unmixing techniques used to resolve the photoabsorbers, exogenous and endogenous, within the region of interest [56].

The unique characteristics of PA imaging allow it to be a purposeful tool for neuroimaging. Because of PA imaging's dependence on optical absorption, it transmits light that is mostly ignored by bone to interrogate tissue, an advantage over other current CNS imaging modalities [57]. As a result, PA neuroimaging has been able to make use of a wide range of PA imaging methods such as spectroscopic PA, PA tomography, and PA microscopy [58-62]. For example, PA tomography has been used to visualize cerebral vessels and measure oxygen saturation, which has been further applied to functional imaging studies [63, 64]. Additionally, PA imaging has been used to detect targeted

nanoparticles in a brain tumor of a mouse model [65]. In PA microscopy, amyloid plaques, a hallmark of Alzheimer's, were detected *in vivo* through a cranial window [66].

As a result, PA neuroimaging has the potential to encompass a wide range of applications. Used in conjunction with US imaging, both morphological and functional information can be discerned. Furthermore, the two modalities are cost-effective, portable, and easily integrated as they can utilize the same US sensor and receiver electronics. Neither modality uses ionizing radiation, making them safer than those that do, such as CT, PET, and SPECT [67, 68]. Therefore, combining these synergistic modalities allows for real-time and effective neuroimaging.

1.5 Perfluorocarbon nanodroplets (PFCnDs)

Perfluorocarbon nanodroplets (PFCnDs) are a class of phase change agents that have been primarily investigated for contrast enhanced ultrasound imaging [69]. They are presented as an alternative to contrast enhanced imaging with microbubbles [69]. PFCnDs are attractive due to their triggered phase change ability from liquid nanodroplet to gas microbubble. As such, they present themselves as a versatile tool not only for imaging but also for localized delivery and opening of biological barriers [70, 71].

1.5.1 General characteristics

PFCnDs are unique particles in that, when activated by laser or acoustic energy, can phase change from liquid to gas [72, 73]. As a result, and unlike microbubbles, their contrast is localized to the area in which they are activated [30, 74]. In addition, their circulation time is much longer than that of microbubbles, making them useful in longer

imaging and therapeutic sessions [30].They are composed of a liquid core, a shell, and when activated via laser energy, an optical trigger [72, 75]. For laser activation, this optical trigger is key, as the laser interaction with the trigger causes an increase in local temperature and an acoustic pressure wave which together synergistically enable the droplet phase change [72]. Both acoustically activated and laser-activated PFCnDs behave similarly with regard to their phase change ability. In particular, phase change of PFCnDs results in a volumetric expansion of the PFCnDs to a gas microbubble on the order of four to five times the original diameter [76]. Additionally, phase change behavior for both acoustically activated and laser-activated PFCnDs is governed by their composition, the species of perfluorocarbon used and the droplet size, as well as energy parameters used, such as peak negative pressure for acoustic activation and light fluence for laser-activated droplets [73, 75, 77].

The physical mechanism of PFCnD phase change is not well understood, although a few hypotheses have been considered, focusing on the thermodynamics and kinetics of the perfluorocarbon core [78, 79]. One theory relies on Laplace pressure, suggesting that PFC droplets become superheated when synthesized on the nanoscale, shifting their equilibrium saturation curve to higher temperatures and lower pressures. As a result, PFCnDs remain stable at temperatures and pressures in which they should thermodynamically vaporize [79]. Another theory posits that suppression of droplet vaporization at thermodynamically expected temperatures and pressures is due to kinetics. That is, PFCnDs are homogeneously nucleated and require considerable activation energy to phase change, resulting in superheated, kinetically metastable PFCnDs. Thus, spontaneous vaporization within the droplet population would be minimal [78].

Composition and synthesis of PFCnDs have been explored extensively [30, 76, 80-82]. Various perfluorocarbon cores have been utilized, with the primary focus on perfluorohexane (C_6F_{14} – boiling point 57 ºC), perfluoropentane (C_5F_{12} – boiling point 29 ºC), and perfluorobutane (C_4F_{10} – boiling point -2 ºC) for PFCnD synthesis [76, 83]. Biocompatible shells such as lipid and albumin have been used in addition to polymer and fluorosurfactant shells [30, 80, 82, 84]. In the case of laser-activated PFCnDs, optical triggers have covered a wide variety of optically absorbing particles, from organic dyes to metallic nanoparticles [30, 80, 85-87]. Furthermore, methods of synthesizing small, monodisperse droplet populations have been developed. Microfluidics, co-solvent evaporation techniques, the ouzo method, microbubble condensation, extrusion, and sonication and centrifugation are employed [76, 87]. Overall, a wide variety of materials and methods can be used to generate PFCnDs for biomedical applications.

1.5.2 Applications of PFCnDs

Biomedical applications of PFCnDs are far-reaching, with use in both imaging and therapy. As an imaging agent, PFCnDs are capable of providing diagnostic information. For example, PFCnD shells can be modified to include targeting ligands for molecular imaging [79, 88, 89]. Examples include vascular targeting or HER-2 targeting for cancer detection [82, 89]. Furthermore, PFCnDs can be combined with custom imaging sequences to improve image contrast, and the distinct behavior of droplets can be tracked to achieve super-resolution imaging [74, 85, 90, 91]. Although contrast enhancement and diagnostic capabilities can be achieved with acoustically activated droplets, laser-activated PFCnDs provide additional advantages. For laser-activated PFCnDs, the interaction of the optical trigger and laser allows laser-activated PFCnDs to act both as an ultrasound (US) and

photoacoustic (PA) contrast agent [30, 74]. Ultrasound and photoacoustic (US/PA) imaging of PFCnDs can provide localized, functional, and morphological imaging from the PA and US generated PFCnD signals [30, 74]. Although the skull can provide some challenges to US imaging, US and PA work together to overcome these potential gaps in functional imaging. In addition, PFCnD signal is dynamically captured in both US and PA imaging, and the unique characteristics of these particles can be exploited in the process of developing US/PA image-guidance of CNS barrier opening and delivery of cargo.

Therapeutic applications of PFCnDs have been widely investigated since the early 2000s [92]. By encapsulating cargo within a PFCnD and locally releasing it via the phase change triggered by acoustic or laser energy, PFCnDs can reduce unwanted effects from systemic release while increasing therapeutic efficacy [93]. Cargo loading is primarily contained to the PFCnD shell, as the perfluorocarbon core of the droplet is both hydrophobic and lipophobic [94, 95]. Therapeutic delivery using PFCnDs has been demonstrated with delivery of doxorubicin for cancer treatment as well as delivery of gases such as oxygen to the tissue [70, 71]. Transfection of genes has also been enhanced by the use of PFCnDs by delivering gene therapy agents via targeted PFCnD constructs [71].

The ability of PFCnDs to cavitate can also be used as a means of non-thermal therapy. Phase change nanodroplets have been used in applications such as tumor ablation and sonothrombolysis as well as more recently for sonoporation [71]. In neuroscience applications, acoustically activated PFCnDs have been used to open the BBB [96]. As laser-activated PFCnDs share similar behavior to acoustically activated PFCnDs, exploration of laser-activated PFCnDs to do the same is warranted. In particular, laser activation of PFCnDs is possible with higher boiling point species that would require

significantly high acoustic pressures to vaporize [76]. Thus, neuroscience applications using laser activation can utilize higher boiling point PFCnDs, reducing *in vivo* spontaneous vaporization that can occur with PFCs with boiling points lower than physiological temperature [70]. For example, when a high boiling point perfluorocarbon core is used, such as perfluorohexane (PFH), droplets transiently vaporize and recondense [74]. This characteristic nature of laser-activated PFHnDs to continuously phase change, i.e., expand and contract, can therefore be harnessed to open the BBB similar to cavitation and acoustic vaporization of PFCnDs with focused ultrasound.

Consequently, the unique characteristics of laser-activated PFCnDs as an US/PA imaging and therapeutic agent support the investigation of laser-activated PFCnDs in neurological applications, specifically for BBB opening and US/PA neuroimaging.

1.6 Summary of research goals

The objective of this research is to develop laser-activated perfluorocarbon nanodroplets for applications in neuroscience. The versatility of laser-activated PFCnDs enables them to act as a multifaceted tool. PFCnDs can act as a mechanical agent to open biological barriers, a delivery vehicle, and a dual ultrasound and photoacoustic imaging contrast agent. The capabilities of laser-activated PFCnDs in the context of the brain is explored through these studies, and the usefulness of PFCnDs as mechanical agent, delivery vehicle, and US/PA imaging contrast agent is shown.

In CHAPTER 2, laser-activated perfluorohexane nanodroplets are investigated as a noninvasive means to open the blood brain barrier. BBB opening is evaluated through Evans Blue dye extravasation into the tissue along with histology and

immunohistochemistry. *Ex vivo* ultrasound and photoacoustic imaging after BBB opening is also demonstrated and establishes PA imaging after BBB opening as a means for evaluating the extent of BBB opening caused by laser-activated PFHnDs. CHAPTER 3 continues to examine laser-activated PFHnD induced BBB opening by evaluating the laser parameter effects on the extent of BBB opening. Qualitative and quantitative analyses are performed to understand how laser fluence and number of laser pulses used influences BBB opening area and volume.

After the laser-activated PFHnD BBB opening is optimized for safety and efficacy, delivery of extravascular PA contrast agents to the brain for *in vivo* US/PA imaging is investigated. CHAPTER 4 determines the optimal PA contrast agents for short term and long term US/PA imaging studies through the use of *in vitro* cell studies. CHAPTER 5 addresses *in vivo* US/PA imaging capabilities after laser-activated PFHnD induced BBB opening. *In vivo* imaging is shown to provide the ability to monitor the extent of BBB opening over time. In addition, PFCnDs are evaluated for their ability to provide dynamic US/PA imaging contrast in the brain. Specifically, a set of laser-activated perfluoropentane nanodroplets is delivered to the brain post BBB opening to examine multiplexed delivery of PA imaging contrast.

Finally, CHAPTER 6 discusses the conclusions drawn by investigating laser-activated PFCnDs for neurological applications and comments on the future work to be completed with this nanoagent. First, challenges of the current studies are addressed and next steps are presented. Next steps, ranging from utilizing laser-activated PFCnDs to open other biological barriers to longitudinal US/PA neuroimaging are described, providing an overall outlook for laser-activated PFCnDs in neuroscience.

CHAPTER 2. NON-INVASIVE BLOOD BRAIN BARRIER OPENING USING LASER-ACTIVATED PERFLUOROCARBON NANODROPLETS

2.1 Introduction

Noninvasive treatment and monitoring of neurological disease is greatly hindered by the blood brain barrier (BBB), which often blocks delivery of therapeutics and contrast agents to the brain tissue [9, 97]. To overcome this barrier, many methods of delivering contrast and therapeutics to the brain for disease diagnosis and treatment have been developed and are currently used in the clinic [5, 6, 9]. However, the methods developed, such as surgical resection, device implantation, or chemical manipulation of tissue via pharmacological substances, have challenges and pitfalls. These methods can be invasive, and their effects can result in widespread opening of the BBB, which is not always desirable, as this greatly increases the risk of complications such as infection [5, 9]. Furthermore, these interventions often do little to prevent the recurrence rate of high mortality diseases, like glioblastoma [6]. This main challenge of overcoming the BBB is difficult, as it prevents the passage of large molecules (>500 Da) from entering into the brain tissue [9, 97]. In recent years, focused ultrasound (FUS) has been developed as an alternative method to transiently open the BBB by using the interaction between the FUS field and microbubbles [5, 11, 18, 97, 98]. Although the biological mechanisms of this method are not fully understood, it is widely believed that the oscillation or cavitation of microbubbles, which interact with the endothelial lining of the brain vasculature, stretch tight junctions and increase the uptake through mechanotransduction pathways, allowing

for larger molecules to pass through the BBB [12, 97, 98]. Because of its localized effect, BBB opening occurs only where the FUS field and microbubbles are present, and delivery of contrast and therapeutic agents can be targeted to precise locations. FUS mediated delivery of therapeutics to the brain has shown promise, resulting in initial clinical trials [27, 99].

Another possible, noninvasive means of opening the BBB is through the use of perfluorocarbon nanodroplets (PFCnDs). PFCnDs are unique particles, that when activated by electromagnetic or acoustic energy, can phase change from liquid to gas [72, 73, 75]. They are composed of a liquid core, a shell, and when activated via laser light, an optical trigger [72, 75]. PFCnDs, activated by a FUS field and converted to gas microbubble *in situ* have been investigated to examine their ability to open the blood brain barrier [96, 100]. Acoustically activated PFCnDs phase change to microbubbles when exposed to sufficient rarefractional pressure provided by FUS and are capable of providing BBB opening through the phase change and stable cavitation of the produced microbubbles [96]. Because of their similarity to microbubbles in their gaseous state, it was demonstrated that PFCnDs are capable of producing similar BBB opening effects [96, 100]. Although acoustic droplet vaporization (ADV) enables BBB opening, it involves the use of below body temperature perfluorocarbon such as perfluorobutane (boiling point -1.7°C) or octafluoropropane (boiling point -36.7°C) which can result in premature, spontaneous droplet vaporization *in vivo* [100]. These lower boiling point PFCs are used for acoustic droplet vaporization because PFCs with boiling points above body temperature would require potentially unsafe, higher pressure acoustic waves to cause phase change [73]. Thus, there are limitations to the use of ADV as a means to open the BBB.

In general, PFCnDs are multifaceted as they are small in size (i.e., hundreds of nanometers) in their liquid state and are capable of carrying therapeutics or other particles, which are either encapsulated or attached to the droplet shell [70]. More importantly, PFCnDs act as a versatile agent when activated to their gaseous phase via multiple forms of energy including electromagnetic waves such as pulsed laser light [73, 75, 80]. Specifically, the absorption of laser energy by the droplet's optical trigger causes localized heating and expansion and produces a photoacoustic pressure wave, and together these phenomena phase change a PFCnD from liquid to gas [75]. Vaporization under a laser pulse of low and, therefore, safe fluence produces ultrasound (US) and photoacoustic (PA) contrast, resulting in the development of laser-activated PFCnDs as dynamic US and PA imaging contrast agents [30, 73, 75, 80, 90]. Laser activation of PFCnDs due to the optical trigger located within the droplet allows for implementation of higher boiling point PFCnDs, such as perfluoropentane (boiling point 29°C) or perfluorohexane (boiling point 57°C) [83]. Thus, laser-activated PFCnDs can be synthesized with many different components, using varying combinations of photoabsorbers, perfluorocarbon (PFC) species, as well as PFCnD sizes, creating application-specific PFCnDs [30, 75, 80, 86].

Laser-activated PFCnDs have the potential to aid in the diagnosis and treatment of neurological diseases. Indeed, optically activated PFCnDs are an attractive tool for BBB opening, as they can be selectively and repeatedly vaporized at the particular wavelength at which their optical trigger absorbs the most laser light energy [30, 75, 80]. To enable successful BBB opening, PFCnD parameters (size, PFC species, and concentration) and laser parameters (fluence and lasing duration) must be selected appropriately in order to achieve BBB opening.

In this work, the characteristics of NIR dye loaded perfluorohexane nanodroplets (PFHnDs) were harnessed to open the BBB and deliver substances to the tissue. BBB opening was evaluated qualitatively on both the macroscopic and microscopic level by examining Evans Blue extravasation, *ex vivo* US/PA imaging, and histology.

2.2 Materials and methods

2.2.1 Laser-activated perfluorohexane nanodroplet (PFHnD) synthesis

With a boiling point being above body temperature (57°C), perfluorohexane (FluoroMed, L.P.) was used as the core of the synthesized PFCnDs [83]. In addition to 0.3 mL of perfluorohexane (PFH), 3 mL 1X PBS, 1 mL Zonyl FSO fluorosurfactant (1% v/v, Sigma Aldrich), and 2 mg Epolight 3072 dye (Epolin, Inc.) – a near infrared (NIR) dye with a peak absorption around 1064 nm – were used. All materials were added to a 7 mL scintillation vial and vortexed for 10 seconds (Vortex Mixer, Fisher Scientific). The vial was placed in an ice bath and sonicated using a probe sonicator (Q500, QSonica LLC) for a total of 60 seconds at the lowest sonicator amplitude of 1. The emulsion was then transferred to two, 2 mL tubes and spun in a mini centrifuge (Mini-Spin, Eppendorf) at 400 rcf for 2 minutes to remove excess dye and size separate PFHnDs. The supernatant containing smaller sized PFHnDs was transferred to another 2 mL tube and spun again at 400 rcf for 4 minutes. To concentrate the droplets, the supernatant resulting from this second centrifugation step was removed and the pellet was resuspended in 0.5 mL 1X PBS using a water bath sonicator (VWR, 180 W). When preparing larger sized PFHnDs for BBB opening that would enable larger (i.e., micrometer) sized constructs to extravasate, droplets were sonicated and size separated as described above, but the pellet of the first

centrifugation step was kept, resuspended in 1 mL 1X PBS, and the supernatant discarded. For *in vivo* experiments, the droplets were left under UV light for 30 minutes for sterilization. A spectrophotometer (Evolution 220, Thermo Scientific) was used to measure the absorbance of PFHnDs both with and without NIR dye, and the blank droplet spectrum was subtracted from the spectrum of the PFHnDs containing NIR dye. Droplet zeta potential and size were measured in PBS using a dynamic light scattering (DLS) instrument (Zetasizer Nano ZS, Malvern Instruments Ltd.).

2.2.2 US/PA imaging of a phantom containing laser-activated PFHnDs

To evaluate droplet vaporization and recondenstation dynamics, a polyacrylamide phantom containing solely PFHnDs was fabricated. The polyacrylamide phantom was prepared by first adding 127 mL nanopure water (Thermo Scientific), 42.5 mL 40% polyacrylamide solution (VWR), and 1.7 mL 10% aqueous ammonium persulfate (Sigma Aldrich) to a Büchner flask and mixing with a magnetic stir bar and stir plate. The solution was degassed by sealing the top of the flask with a rubber stopper, attaching the flask to a vacuum, and sonicating using the water bath sonicator for 10 minutes. The solution was returned to the stir plate and 170 µL PFHnDs were added to the solution followed by 212.5 µL of tetramethylethylenediamine (Sigma Aldrich). The phantom was poured into a plastic container and allowed to solidify before removal from the mold.

2.2.3 Imaging and processing of laser-activated PFHnD vaporization and recondensation dynamics

To visualize the phase change dynamics of PFHnDs, the prepared polyacrylamide phantom embedded with PFHnDs was imaged using a Verasonics Vantage 256 ultrasound

system (Verasonics Inc.) and an Nd:YAG Phocus laser (10 Hz, 5-7 ns pulse length, Opotek Inc.) operating at 1064 nm and a fluence of 46 mJ/cm². An array transducer operating at 5 MHz (L11-4v, Verasonics Inc.) was used to capture ultrasound at a frame rate of 500 frames per second. Photoacoustic signal was captured at the rate of 10 Hz (laser PRF). Ultrasound data was collected for six frames after each laser pulse (12 milliseconds total), and pixels containing droplets were identified using compounded harmonic ultrasound difference images, similar to a previously described method [91]. To visualize PFHnD recondensation dynamics over time, linear ultrasound intensity of the identified droplet pixels was plotted over multiple laser pulses.

2.2.4 Laser-activated PFHnD induced blood brain barrier opening

All animal studies were conducted under the protocol approved by the Institutional Animal Care and Use Committee at Georgia Institute of Technology. Prior to anesthesia, an injection of sustained released buprenorphine (IP, 0.8 mg/kg) was administered to each animal (C57BL/6 mouse). Mice were anesthetized using a combination of isoflurane (2%) and oxygen (0.6 L/min). Mice were positioned in a stereotax in the prone position, on a heating pad (Stoelting Co). Hair from the scalp was removed through shaving and depilatory cream. Proparacaine (0.5%, Henry Schein) was applied to the eyes and a retro-orbital injection of 50 µL of 3% w/v sterile filtered Evans Blue (EB) (Sigma Aldrich) was administered with or without a co-injection of 50 µL PFHnDs (~10^8 droplets, measured using a Malvern NanoSight NS300), depending on the animal group. The animal groups included mice irradiated with 1064 nm light and co-injected with EB dye and PFHnDs (experimental group, n=10), mice irradiated with 1064 nm light and injected with EB dye only (i.e., no PFHnDs, control group, n=3), and mice co-injected with EB dye and PFHnDs

but not irradiated (another control group, n=3). Animals were positioned beneath an unfocused 1.5 mm core diameter optical fiber (0.39 NA, Thorlabs, Inc.) to enable irradiation of the right side of the brain. Irradiation was performed using a Vibrant laser (10 Hz, 5-7 ns pulse length, Opotek Inc.) with a wavelength of 1064 nm and a fluence of 70 mJ/cm^2. Irradiation was performed for 60 seconds, falling within a similar time range to that of sonication for microbubble assisted FUS BBB opening (Figure 2) [5, 17]. After laser irradiation, mice were observed for 4 hours, with no gross behavioral damage observed. Animals were then sacrificed and perfused with 1X PBS (pH 6.8) followed by 4% paraformaldehyde (PFA). Heads were removed and post-fixed overnight in 4% PFA solution. After 24 hours, brains were excised and whole brain photographs were taken (Figure 3).

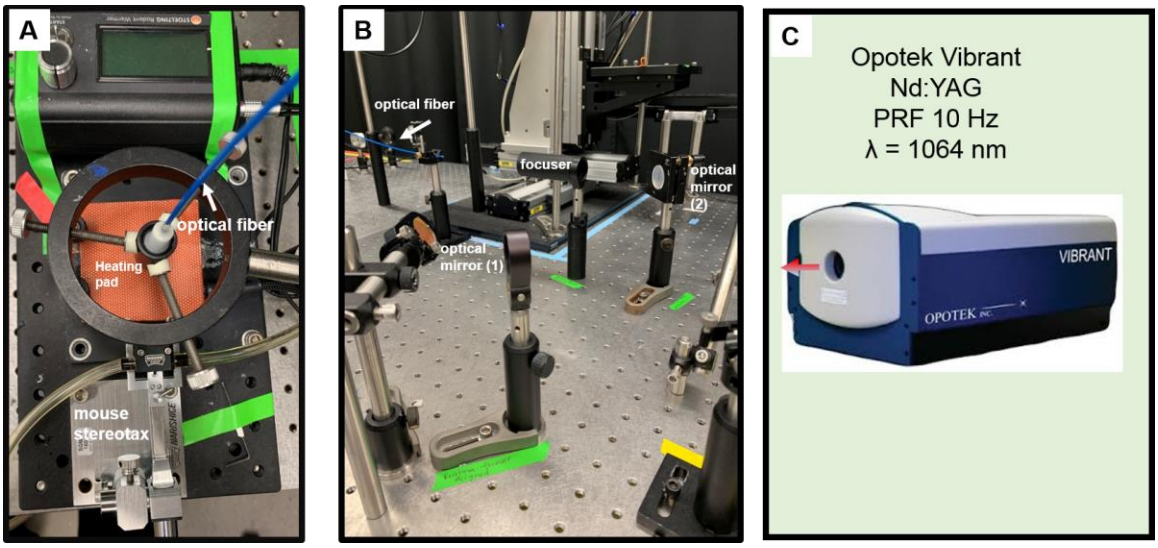

Figure 2. Laser irradiation setup for blood brain barrier (BBB) opening. (A) View of the optical fiber placed above the mouse stereotax and heating pad. (B) Optical path of the laser beam to the optical fiber. (C) Laser system used for BBB opening and its specifications.

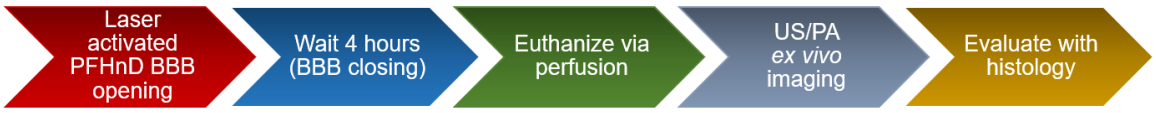

Figure 3. Timeline for laser-activated PFHnD induced BBB opening procedure and evaluation.

2.2.5 Ex vivo ultrasound and photoacoustic imaging

Fixed, excised mouse brains were imaged using a photoacoustic and ultrasound imaging system (Vevo LAZR, FUJIFILM VisualSonics Inc.) with a 40 MHz ultrasound and photoacoustic imaging probe (LZ-550, FUJIFILM VisualSonics Inc.). The system's tunable Nd:YAG laser (20 Hz, 5-7 ns pulse length) was operated at a wavelength of 1064 nm and at a fluence of 10-12 mJ/cm², and specimens were imaged at a US/PA frame rate

of 5 frames per second. Tissue samples were placed on top of an 8% gelatin base in a container filled with degassed water. Images were acquired by performing coronal and sagittal 3D US/PA imaging with a distance step size of 0.1 mm. 3D US/PA imaging at 1064 nm was performed both for the experimental and two control groups.

2.2.6 Histology and immunohistochemistry

After remaining in 4% PFA solution for 24 hours at 4°C, brains were transferred to a solution of 30% sucrose and stored at 4°C for 5 days. Brains were snap frozen, and 20 µm coronal sections were cut using a cryostat (Leica CM 1860, Leica Biosystems). For each brain, 72 sections were cut and analyzed, spanning a total volume of 1.44 mm. Standard hematoxylin (Sigma Aldrich, Gill No.2) and eosin (VWR) (H&E) staining was performed. H&E photomicrographs were captured using the bright field mode of a Zeiss AxioObserver Z1 Microscope. IHC was also performed using DAPI (4',6-diamidino-2-phenylindole, Invitrogen) and a secondary antibody of goat anti-mouse IgG (H+L) tagged with Alexa Fluor 488 (Invitrogen). IHC photomicrographs were captured using a Zeiss Laser Scanning Confocal Microscope 700.

2.3 Results

2.3.1 Characterization of laser-activated PFHnDs

The results of PFHnD characterization including size, absorbance, charge, and dynamic ultrasound behavior are shown (Figure 4). The synthesized PFHnDs had a diameter of 340 nm ± 170 nm (Figure 4A), an order of magnitude smaller than typical microbubbles used for BBB opening [97]. Due to optical NIR dye embedded into PFHnDs,

the droplets exhibit peak optical absorption at around 1064 nm (Figure 4B). A dye absorbing near the 1064 nm wavelength was specifically selected because of the deep penetration of light in tissue at this wavelength, readily available from an energy-efficient nanosecond pulsed laser system [75]. Evans Blue had a peak optical absorption of 600 nm, thus there was minimal optical interaction between the 1064 nm light from the Nd:YAG laser and Evans Blue dye. A fluorosurfactant shell was used to encapsulate liquid PFH and the NIR dye, resulting in a droplet with a negative zeta potential when measured in PBS (-21 mV, Figure 4C).

The synthesized PFHnDs produced a repeatable vaporization and recondensation response to pulsed laser irradiation (Figure 4D). This liquid-gas-liquid phase change dynamic is shown via the linear ultrasound intensity of a PFHnD over time and for multiple laser pulses, with dashed lines indicating time between acquisitions. In the presence of laser irradiation, PFHnDs quickly change from liquid to gas, denoted by an increase in ultrasound amplitude. During this phase change process, PFHnDs expand to 4-5 times their droplet size, making these particular droplets 1-2 μm in size in their gaseous sate [72]. After 10 milliseconds, the PFHnD recondenses, resulting in a lower observed ultrasound intensity. This vaporization and recondensation cycle is repeated every 0.1 seconds, which corresponds to the laser PRF of 10 Hz. As a result, laser activation of PFHnDs enables the creation of repeatable, transient microbubbles, which can be observed via their ultrasound behavior.

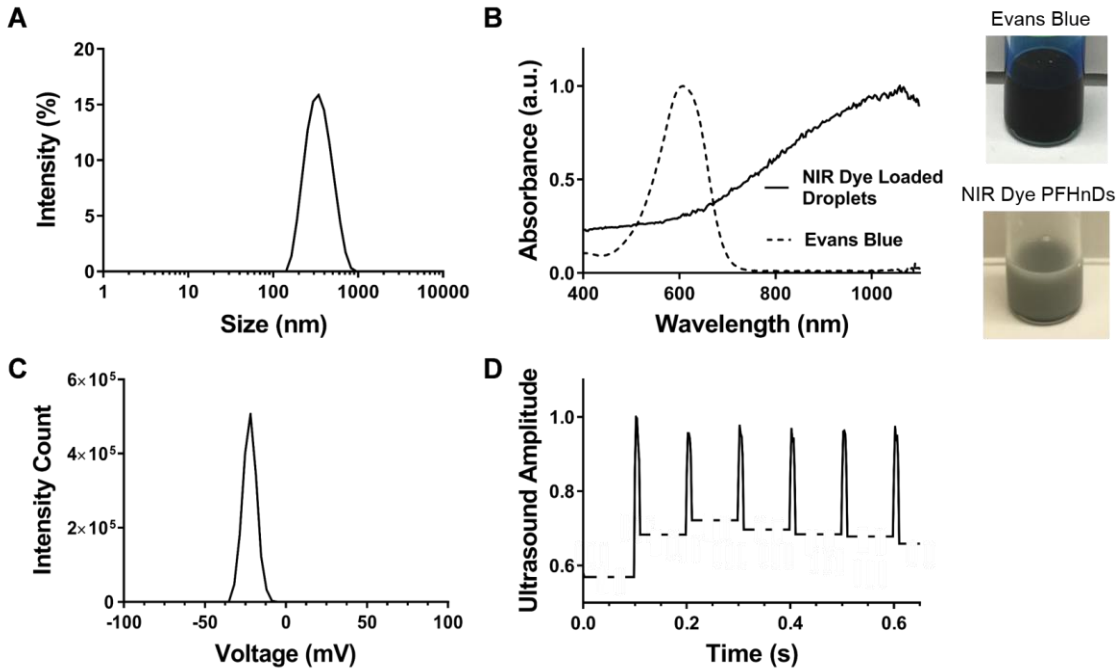

Figure 4. Characterization of perfluorohexane nanodroplets (PFHnDs). (A) Size distribution of droplets (340 nm ± 170 nm). (B) Normalized absorbance spectra of droplets containing a near-infrared (NIR) dye with a peak absorption at 1064 nm and Evans Blue dye with a peak optical absorption at 600 nm, both of which are used for *in vivo* experiments of blood brain barrier opening. Images to the right show appearance of Evans Blue and NIR dye loaded PFHnDs. (C) Zeta Potential of the fluorosurfactant shell of the PFHnDs, with a peak at -21 mV. (D) Normalized ultrasound signal produced by PFHnDs as they repeatedly vaporize in response to pulsed laser irradiation and then immediately recondense after each laser pulse.

2.3.2 Evans Blue staining confirms BBB opening via laser-activated PFHnDs

Validation of BBB opening was confirmed through visual examination of EB dye staining, US/PA imaging, and histology. EB dye extravasation was evaluated through inspection of the whole brain followed by inspection of coronal cross-sections for each animal group (Figure 5). The differences in brain tissue coloration results from the lighting in which images were taken. EB dye is a commonly used substance for determining BBB opening, as it attaches itself to albumin and will cross the BBB only when the barrier has been opened [101]. When Evans Blue dye has extravasated, it is visibly evident in the

tissue. After laser irradiation, EB dye was allowed to extravasate for four hours prior to animal perfusion, as the BBB likely begins to close at this time point [5, 102]. For the experimental group, when EB dye was co-injected with PFHnDs and the laser irradiation was applied, EB dye extravasation into tissue is apparent in both whole brain and coronal cross section images (Figure 5A-B). This staining is located on the right side where the pulsed laser irradiation was applied. It appears greatest at the top of the brain corresponding to where laser fluence is the highest. However, when EB dye and PFHnDs were co-injected and no laser irradiation was applied, the brain tissue remains unstained (Figure 5C-D). Finally, the combination of laser irradiation and EB dye administration but no injection of PFHnDs also results in tissue with no EB dye extravasation (Figure 5E-F). Thus, these results demonstrate that PFHnDs combined with laser irradiation are capable of opening the BBB and delivering substances to the brain.

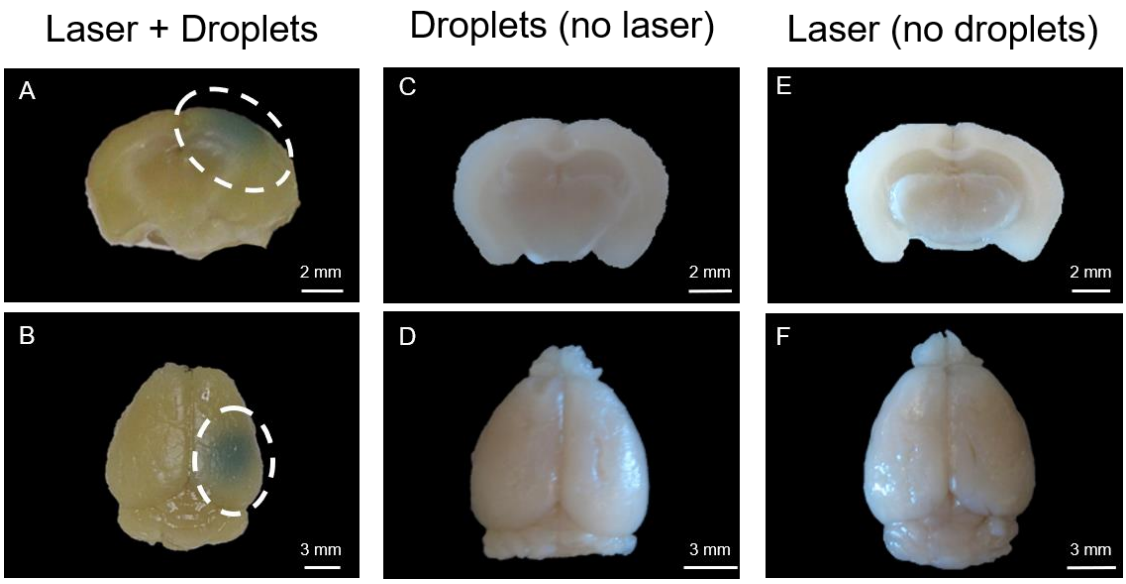

Figure 5. Photographs of Evans Blue (EB) dye extravasation into tissue. (A-B) Whole brain (top view) image and coronal cross-section of brain showing EB dye leakage into brain tissue post-irradiation. The rounded dashed contour highlights area of EB dye extravasation and the horizontal dashed line indicates the location of the coronal cross section displayed in panel B. (C-D) Control: whole brain image and coronal cross section of brain with EB dye and droplets administered but no laser irradiation applied. Without laser irradiation, EB dye is unable to extravasate across the blood brain barrier, preventing tissue staining. (E-F) Control: whole brain image and coronal cross-section of brain with laser irradiation applied and EB dye administered but no droplets injected. Without droplets, EB dye is unable to extravasate across the blood brain barrier, preventing tissue staining. Reprinted from [84].

2.3.3 US/PA imaging of extravasated photoacoustic dye

US/PA imaging of perfused, excised murine brains was also performed to evaluate BBB opening (Figure 6). The synthesized PFHnDs contain a dye absorbing at 1064 nm, which produces a PA signal at that wavelength. Thus, if droplets containing the dye empty some of their cargo in the process of vaporization, this dye has the potential to extravasate across the BBB. Once extravasation has occurred, PA signal at 1064 nm should be present, allowing for US/PA imaging of the tissue. US imaging provides an anatomical map, while PA imaging provides the localized signal of extravasated dye. In the experimental group

(Figure 6A), where PFHnDs and laser irradiation were present during the BBB opening procedure, PA signal is present on the right side of the brain in a coronal cross section that corresponds to the location of EB staining as seen in the whole brain and cross section photographs (Figure 5A-B). To confirm that the PA signal comes from the 1064 nm absorbing dye extravasated post-laser irradiation, control groups were also US/PA imaged at 1064 nm. One control group involved the administration of droplets but no laser irradiation during the BBB opening procedure (Figure 6B). The second control group included laser irradiation but no administration of droplets (Figure 6C). US/PA imaging of these brains demonstrates that extravasation of dye occurs only if droplets are present and have been irradiated because no PA signal at 1064 nm is produced otherwise (Figure 6B-C). Thus, US/PA imaging can be used to evaluate BBB opening when laser-activated PFHnDs are used.

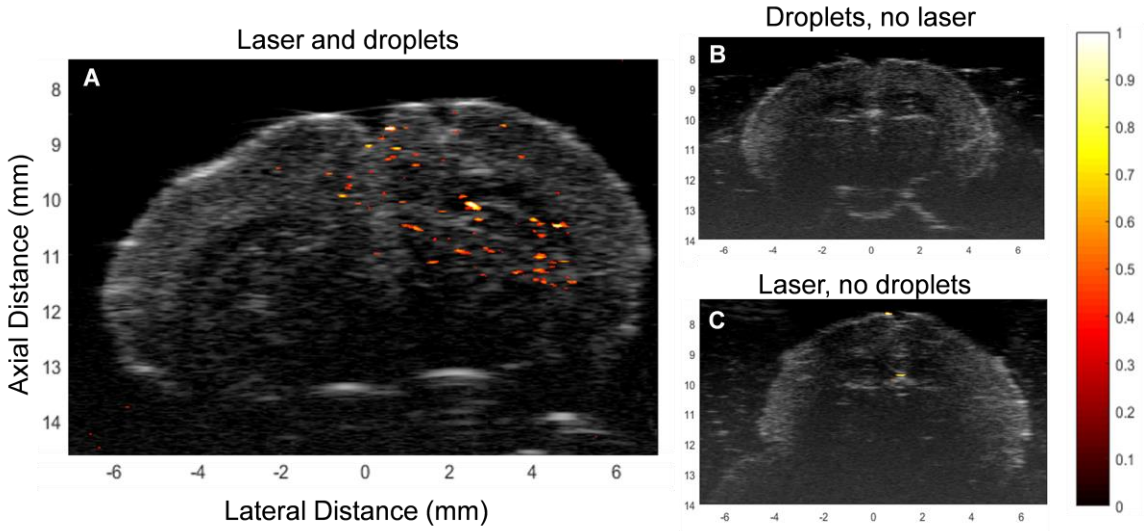

Figure 6. *Ex vivo* photoacoustic and ultrasound (US/PA) imaging of murine brains (A) US/PA imaging of an animal with blood brain barrier opening and release of near-infrared (NIR) dye from PFHnDs after laser irradiation. After opening, the NIR dye has extravasated across the blood brain barrier and provides signal when imaged at 1064 nm. (B) Control: US/PA imaging demonstrating that without laser irradiation to vaporize droplets, no NIR dye has extravasated, resulting in no PA signal produced at the imaging wavelength. (C) Control: US/PA image demonstrating that without droplets to open the blood brain barrier, no NIR dye has extravasated, resulting in no PA signal produced at the imaging wavelength. Reprinted from [84].

2.3.4 Histological and immunohistochemical evaluation of laser-activated PFHnD induced BBB opening

BBB opening was further examined on the cellular level using histological and immunohistochemical methods (Figure 7). For these studies, larger size PFHnDs were synthesized (837 nm ± 229 nm) to ensure significant BBB opening and enable definitive extravasation of biological particles across the BBB. When activated via laser irradiation, these PFHnDs should expand to 3-4 µm in size in their gaseous sate [72]. As a result, these larger bubbles will enable greater BBB opening and illicit a larger biological response [21]. For the studies involving laser irradiation (Figure 7A-C, G-I), irradiation was performed

for 60 seconds at a wavelength of 1064 nm and a fluence of 70 mJ/cm^2. To examine the extravasation of nanosized constructs, fluorescence images captured the extravasation of mouse immunoglobulin G (IgG), which should only cross the BBB when the barrier is opened, due to its width being 13.7 nm (Figure 7A-B, D-E, G-H) [103]. In the experimental group where opening took place (laser irradiation and droplets), staining of IgG is clearly present (Figure 7A-B). In control animals where no laser irradiation was applied but droplets were administered (Figure 7D-E), no extravascular IgG is observed. However, there appears to be low levels of IgG signal in the lateral ventricles in the fluorescent image of the whole brain (Figure 7D), but when a high magnification view of the tissue is examined (Figure 7E), no IgG is present. In the case of laser irradiation but no droplet injection, low levels of IgG are also observed in both the whole brain image and magnified view (Figure 7G-H). From the IHC analysis, it appears that some IgG may be present in the control groups, however, delivery of IgG across the BBB is most obvious in the experimental group containing both laser irradiation and PFHnDs.

Delivery of larger constructs, specifically red blood cells (RBCs), was also examined via H&E staining (Figure 7C, F, I). As seen in the experimental group (Figure 7C), RBCs extravasated across the blood brain barrier and are highlighted by the tissue area stained red. For both controls, however, no RBCs extravasated (Figure 7F, I). Because RBCs were able to extravasate in the experimental group, the result indicates that laser-activated PFHnDs were able to create openings in the BBB that allowed for 6 μm diameter particles to cross the blood brain barrier [104].

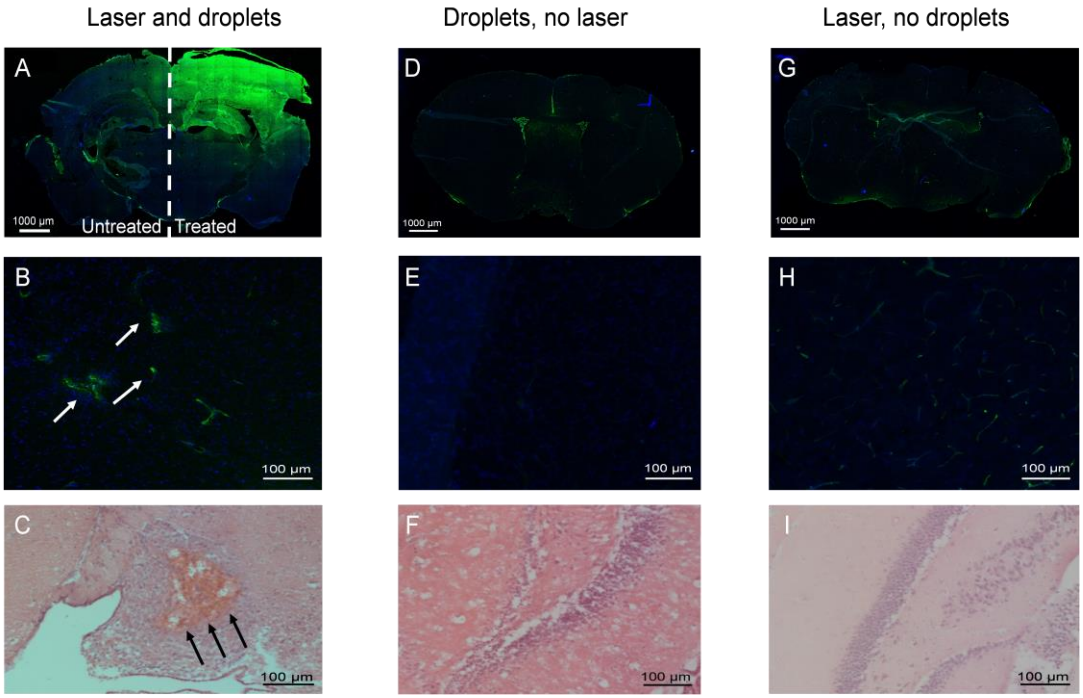

Figure 7. Immunohistochemical and histological analysis of mouse brain tissue. (A-B) Immunohistochemical (IHC) staining of DAPI and secondary antibody IgG of a mouse treated with both droplets and laser irradiation on the right side of the brain. Presence of green fluorescence (white arrows) demonstrates IgG extravasation and opening of the blood brain barrier. (C) Hematoxylin and eosin (H&E) staining of a mouse treated with both droplets and laser irradiation. Presence of red blood cells is indicated by bright red eosin staining (black arrows) and demonstrates extravasation and opening of the blood brain barrier. (D-E) Control: IHC staining of a mouse treated with droplets only and no laser irradiation. (F) H&E staining of a mouse treated with droplets only and no laser irradiation. (G-H) Control: IHC staining of a mouse treated with laser irradiation but with no droplets injected. (I) H&E staining of a mouse treated with laser irradiation but with no droplets injected. (A),(D),(G) are fluorescence images displaying the entire 20 µm tissue slice while (B-C), (E-F), and (H-I) display a close-up view of the tissue section. Reprinted from [84].

2.4 Discussion

In this work, successful delivery of various sized constructs such as RBCs, Evans Blue (EB) visible dye bound to albumin, NIR dye, and IgG was delivered across the BBB using laser-activated perfluorohexane nanodroplets (PFHnDs). The delivery of these particles was verified and evaluated through different methods including EB dye staining,

US/PA imaging, and histological tissue analysis. Thus, droplet parameters play a key part in determining BBB opening. Specifically, droplet size, PFC species, and photoabsorbers selected all play a unique role in the effective size and spread of BBB opening and therefore delivery of substances into the tissue. For example, larger sized PFCnDs can cause an increase in BBB opening volume and potentially damage to the tissue. A lower boiling point perfluorocarbon that does not repeatedly vaporize and recondense such as perfluoropentane may not open the BBB to a similar extent as PFH. Further, a lower wavelength photoabsorber could prevent deeper activation of PFCnDs due to reduced light penetration in the tissue. Thus, by selectively choosing the appropriate droplet components, droplets can be used in and tailored to a diverse set of applications, including delivery of contrast agents and therapeutics to the brain. Furthermore, laser parameters also contribute to BBB opening and can be adjusted based on droplet parameters to achieve the desired volume and location of BBB opening in the brain tissue.

In these studies, PFCnD characteristics were chosen to achieve effective BBB opening. Specifically, PFHnDs were synthesized such that upon laser irradiation, the size of resulting microbubbles would be similar to those that have been used in FUS BBB opening (Figure 4A) [5]. A NIR dye absorbing near 1064 nm was used not only for increased depth penetration of light but also to avoid optical absorption by the Evans Blue dye co-injected with PFHnDs. Evans Blue has a peak absorption of 600 nm, and at 1064 nm, EB absorption is negligible (Figure 4B). Therefore, the negligible interaction of EB and the 1064 nm laser light will not cause BBB opening, and extravasation of the EB across the BBB will only occur when droplets are both present and exposed to laser irradiation. In addition, low EB absorption at 1064 nm indicates that the captured US/PA signal is

produced from NIR dye delivered to the tissue. The US/PA imaging of the NIR dye in comparison to Evans Blue photographs also suggests that different sized particles are able to cross the BBB using laser-activated PFHnD opening (Figure 6A).

Furthermore, the PFC species used in these droplets plays a key role in successful BBB opening. The ability of PFHnDs to repeatedly vaporize under pulsed laser excitation and then recondense potentially makes a PFH droplet core more attractive than lower boiling point PFCs such as perfluorobutane or perfluoropentane [83]. The reactivation of PFHnDs over multiple laser pulses suggests that in combination with an increased number of laser pulses used, lower concentrations of PFHnDs could be used to open the BBB, reducing the injected PFHnD dose. This concentration comparison may also extend to microbubble concentrations used in FUS BBB opening. Based on the rapid expansion and recondensation of PFHnDs, it is supposed that the phase changing droplets interact with the BBB similar to the way microbubbles do in a FUS field (Figure 4D). As PFCnDs have a longer circulation time than microbubbles (i.e., hours vs. minutes, respectively), fewer PFHnDs may be needed to achieve effective BBB opening [70]. As a result, PFC choice plays a key role when designing laser-activated PFCnDs for BBB opening.

To examine BBB opening, EB staining was evaluated grossly and supported the hypothesis that BBB opening would only occur where both laser irradiation and PFHnDs are present (Figure 5). *Ex vivo* US/PA imaging was also performed to co-register PA signal with the area of EB staining, both localized to the right side of the brain (Figure 6). US/PA contrast from delivered NIR dye indicates the potential for future *in vivo* US/PA imaging of laser-activated PFCnD during BBB opening and delivery of PA contrast agents. Finally, histological staining analysis was completed to examine the effect of laser-activated

PFHnD opening on the molecular level. Overall, extravasation was greatest in the experimental group (Figure 7A-C), further demonstrating that BBB opening can be achieved using laser-activated PFHnDs. However, in both control groups (Figure 7D-E, G-H), IgG signal is present. For the control group where PFHnDs were injected but no laser irradiation was applied, IgG signal was visible in the lateral ventricles but not in a magnified view of the brain tissue, suggesting that the signal most likely corresponds to an incomplete perfusion. In the control group with laser irradiation and Evans Blue dye but no PFHnDs administered, there are a few possibilities as to why IgG may be present. Both deoxygenated hemoglobin and oxygenated hemoglobin absorb in the NIR wavelength range and as a result, interaction of the blood with laser energy could cause small openings in the BBB that would allow for IgG to cross the BBB [105]. Additionally, incomplete perfusion of the tissue could also cause a false positive fluorescence in the sample, as there appears to be IgG signal coming from the lateral ventricles (Figure 7G) in addition to fluorescence signal seen in the magnified view of the pictomicrograph (Figure 7H). Despite the fluorescence signal seen in both control samples, IgG signal is greatest in the experimental group showing that localized BBB opening is effective when PFHnDs are irradiated via pulsed laser excitation. Overall, the results of the methods used to evaluate BBB opening (i.e., EB staining, US/PA imaging, and histological tissue analysis), support the hypothesis that laser-activated PFCnDs are capable of opening the BBB.

Not only can droplets cause opening of this particular biological barrier, but they also have the potential to be implemented to open other biological barriers that may be otherwise inhibited and prevent effective, non-invasive treatment. In particular, another barrier that poses challenges in noninvasive delivery is the blood spinal cord barrier

(BSCB) [4]. Recently, the BSCB has been opened using FUS and microbubbles, so investigation into the ability of PFCnDs to open the BSCB is warranted [4, 106]. For opening of both the BBB and BSCB, laser and droplet parameters should be evaluated for safety and efficacy, as opening of these barriers without fully optimized parameters has the potential to damage tissue.

In addition, droplets can be synthesized to as small as 100-200 nm and therefore have the potential to extravasate themselves when the BBB has been opened [76, 107]. Thus, through the administration of one set of small, cargo carrying droplets and a set of larger droplets used for BBB opening, delivery of substances can be contained within cargo carrying PFCnDs until they have reached their desired location. Because droplets can be produced in various sizes and compositions, they are capable of performing as a multiplexed system, enabling subpopulations of droplets to perform different tasks. This multiplexed ability can be harnessed not only via size, but by also using photoabsorbers of different peak wavelengths, different core perfluorocarbons, and different shell compositions.

Consequently, laser-activated droplet adaptability enables a platform for opening of the BBB and delivery of both therapeutics as well as imaging contrast agents to the brain. Furthermore, laser-activated droplets produce localized, temporally modulated ultrasound and photoacoustic contrast and therefore in the future could provide the opportunity for image-guidance of BBB opening as well as image-guidance of delivery of cargo to the tissue [30, 74, 85, 90, 91]. Because the process of optimized BBB opening is transient and reversible, localized delivery of cargo to the brain is reproducible, enabling the potential to treat or image longitudinally. From opening barriers to providing delivery

and imaging contrast, the presented studies provide an initial demonstration of the capabilities and potential of laser-activated PFCnDs in neurological applications.

CHAPTER 3. OPTIMIZATION OF LASER PARAMETERS FOR BLOOD BRAIN BARRIER OPENING INDUCED BY LASER-ACTIVATED PERFLUOROCARBON NANODROPLETS

3.1 Introduction

A major challenge in the monitoring and treatment of various neurological diseases is the blood brain barrier (BBB) [97, 108]. The BBB is a physiological barrier that prevents large molecules (>500 Da) in the vascular system from extravasating to the brain tissue [9, 97]. Due to the selective nature of the BBB, delivery of contrast agents or therapeutics is greatly hindered, making it difficult to monitor and treat neurological diseases [5, 15, 97, 108, 109]. To overcome the BBB, various methods, such as surgical resection, device implantation, and chemical manipulation of the tissue are currently used [5, 9]. However, there are inherent risks with these methods including invasiveness and widespread opening of the BBB, increasing the potential for infection and resulting in limited success for treating diseases such as brain cancers, Alzheimer's, and Huntington's [6, 108]. Thus, the focus for monitoring and treatment of neurological diseases in the brain has shifted towards noninvasive measures, where BBB opening can be performed transiently, locally, and repeatedly [15, 97].

One well-developed, noninvasive method of opening the BBB is microbubble-assisted focused ultrasound (FUS) [11, 15, 97]. This method relies on the interaction of a focused ultrasound field and oscillating microbubbles to stretch endothelial tight junctions and increase uptake through mechanotransduction pathways, allowing larger molecules to

extravasate [12, 97, 98]. Microbubble-assisted FUS for BBB opening is a technique that has been evaluated for safety and efficacy [15-18]. FUS frequency, pulse duration, PRF, and pressure amplitude, as well as microbubble composition and dose have been examined to determine the optimal range of parameters [10, 19-26]. Consequently, this technology is used in applications ranging from small animal studies to clinical trials [27, 28].

Recently, perfluorocarbon nanodroplets (PFCnDs), a descendant of microbubbles, have been investigated as a means to transiently open the BBB [84, 96, 100]. PFCnDs are a phase change nanoagent capable of changing from liquid nanodroplet to gas microbubble when activated via acoustic or electromagnetic energy [72, 73, 75]. PFCnDs are comprised of a shell, perfluorocarbon core, and an optical trigger when activated via an optical energy source [75]. Specifically, laser-activated PFCnDs rely on the interaction between a pulsed laser and an optical trigger within the droplet to induce the phase change from liquid to gas [75]. Because perfluorocarbon itself is not optically absorbing, a highly optically absorbing dye or nanoparticle is encapsulated within the PFCnD to enable PFCnD vaporization. Phase change of the PFCnD occurs due to the localized heating and photoacoustic pressure wave that result from the optical trigger-laser interaction [75]. For laser-activated PFCnD induced BBB opening, perfluorohexane nanodroplets (PFHnDs) were investigated [84]. PFHnDs are attractive for use in BBB opening due to their ability to undergo repeated phase change from liquid to gas [74, 85, 90, 91], creating an oscillatory-like behavior and allowing laser-activated PFHnDs multiple opportunities to interact with the BBB and enable opening.

In addition to enabling BBB opening, laser-activated PFCnDs are also capable of providing localized ultrasound (US) and photoacoustic (PA) image contrast [30, 73, 76,

80, 86]. The phase change of PFCnDs from liquid nanodroplet to gas microbubble provides US contrast while the pulsed laser-optical trigger interaction that initiates the phase change produces PA contrast. The unique US/PA image contrast provided by laser-activated PFCnDs allows for use in various *in vivo* applications from super resolution imaging to multiplexed imaging [30, 74, 82, 90]. Further, PFCnDs are capable of carrying cargo within the droplet or on the shell, making them attractive as controlled release delivery vehicles [70]. Their nanometer size also makes PFCnDs capable of extravasation across barriers such as leaky vasculature within a tumor or an opened BBB [70, 84, 87, 110]. As a result, the versatile nature of PFCnDs shows their potential to be utilized in a wide variety of applications including the central nervous system.

To understand fully the capabilities of laser-activated PFCnDs in BBB opening and in neurological applications, it is necessary to study the effects of the laser parameters used to activate the PFCnDs. In these studies, two particular parameters, laser fluence and number of laser pulses used, were evaluated, with the results demonstrating how BBB opening can be controlled via laser-activated PFCnDs.

3.2 Materials and methods

3.2.1 IR-1048 laser-activated perfluorohexane nanodroplet synthesis and characterization

IR-1048 perfluorohexane nanodroplets (PFHnDs) were synthesized using IR-1048 dye (Sigma-Aldrich), perfluorohexane (PFH, FluoroMed, L.P.), and a lipid shell comprised of 1,2-distearoyl-sn-glycero-3-phosphoethanolamine-N-[amino(polyethylene glycol)-2000] (DSPE-PEG(2000), 25 mg/mL, Avanti Polar Lipids, Inc.) and 1,2-distearoyl-sn-

glycero-3-phosphocholine (18:0 PC (DSPC), 25 mg/mL, Avanti Polar Lipids). To create the lipid shell, 40 µL of DSPE-PEG(2000) and 8 µL of 18:0 PC (DSPC) were added to a 10 mL pear-shaped flask (Sigma-Aldrich). An IR-1048 dye solution was prepared in chloroform (1mg/mL), and 200 µL was added to the flask. An additional 1 mL of chloroform was added to the flask to enable a smooth lipid cake. A rotary evaporator (Rotovapor, Büchi) was used at reduced pressure to remove the chloroform from the flask leaving an IR-1048 dye-coated lipid cake. The lipid cake was resuspended in 1 mL of PBS using a water bath sonicator (VWR, 180W). The solution was placed in a 7 mL scintillation vial, and 150 µL of PFH was added. The vial was vortexed for 10 seconds (Vortex Mixer, Fisher Scientific) and sonicated for five minutes in an ice-cold water bath (VWR, 180 W). The PFHnD solution was transferred to a 2 mL centrifuge tube and centrifuged for 60 seconds in a mini-centrifuge (Mini-Spin, Eppendorf) to remove excess PFH and IR-1048 dye. The supernatant was transferred to a new 2 mL centrifuge tube, and the pellet was discarded. Prior to *in vivo* experiments, droplets were left under UV light for 30 minutes for sterilization.

PFHnD size and zeta potential were measured in PBS (pH 7.4) using a dynamic light scattering instrument (Zetasizer Nano ZS, Malvern Instruments Ltd.). To generate the absorbance spectrum of IR-1048 PFHnDs, a spectrophotometer was used to measure IR-1048 PFHnDs and blank PFHnDs, i.e., PFHnDs synthesized as described above without dye. The blank PFHnD spectrum was then subtracted from the IR-1048 PFHnD spectrum. PFHnD concentration measurements were made using a NanoSight NS300 (Malvern Instruments Ltd.).

3.2.2 In vivo laser-activated PFHnD induced blood brain barrier opening

All animal studies were conducted under the protocol approved by the Institutional Animal Care and Use Committee at Georgia Institute of Technology. Animal studies were performed as described previously [84]. Briefly, an injection of sustained released buprenorphine (IP, 0.8 mg/kg) was administered to each animal (Balb/c mouse, Jax), prior to anesthesia. Mice were anesthetized using a combination of isoflurane (2%, Henry Schein) and medical air (0.6 L/min, Airgas). Mice were positioned in a stereotax in the prone position, on a heating pad (Stoelting Co). Hair from the scalp was removed through shaving and depilatory cream. Proparacaine (0.5%, Henry Schein) was applied to the eyes, and a retro-orbital injection of 50 µL of 3% w/v sterile filtered Evans Blue (EB) (Sigma Aldrich) was administered with a co-injection of 70 µL of IR-1048 PFHnDs (~10^8 droplets). To allow for irradiation of the right side of the brain, animals were positioned underneath an unfocused 1.5 mm core diameter optical fiber (0.39 NA, Thorlabs, Inc.). Irradiation was performed with a Vibrant laser (10 Hz, 5-7 ns pulse length, Opotek Inc.) at a wavelength of 1064 nm (Figure 2).

Six animal groups (n = 3 mice) were treated with a varying number of laser pulses and varying laser fluences. Three animal groups were exposed to a fluence of 56 mJ/cm², with the number of laser pulses being 300, 600, or 1200 pulses. As the PRF of the laser used was 10 Hz, the total laser irradiation time for these three groups was 30, 60, and 120 seconds, respectively. Two additional animal groups were exposed to 600 laser pulses and had laser fluences of 38 or 70 mJ/cm². The sixth group of animals acted as a control group, with no laser irradiation or a co-injection. Other controls of co-injection without laser irradiation or laser irradiation without co-injection have been performed previously and

showed no BBB opening effect, so the control here serves a baseline for the experimental groups [84]. After laser irradiation, mice were allowed to recover, with no gross behavioral damage observed. After four hours, animals were euthanized via an IP Euthatal injection (150 mg/kg) followed by perfusion with 1X PBS (pH 6.8) and 4% paraformaldehyde (PFA). Heads were removed and post-fixed overnight in 4% PFA solution. After 24 hours, brains were excised, and whole brain photographs were taken.

3.2.3 Ex vivo ultrasound and photoacoustic imaging

Brains, excised and fixed, were placed on top of an 8% gelatin base in a container filled with degassed water. Samples were imaged using an ultrasound and photoacoustic (US/PA) imaging system (Vevo LAZR, FUJIFILM VisualSonics Inc.) with a 40 MHz ultrasound and photoacoustic imaging probe (LZ-550, FUJIFILM VisualSonics Inc.). The US/PA imaging system's tunable Nd:YAG laser (20 Hz, 5-7 ns pulse length) was operated at a wavelength of 1064 nm and a fluence of 12-14 mJ/cm^2. Brains were imaged at an US/PA frame rate of 5 frames per second. Coronal and sagittal 3D US/PA images were collected with a distance step size of 0.102 mm for a total of about 14 mm and 12 mm, respectively. US/PA imaging was performed for all six animal groups.

3.2.4 Ultrasound and photoacoustic image processing

Coronal ultrasound and photoacoustic image sets were processed in MATLAB (Mathworks, Inc.). US/PA images were thresholded to reduce noise and exported to generate 3D whole brain images using AMIRA (Thermo Scientific). Top view and corner cut images of the treated (right) side of the brain, viewed from behind the cerebellum, were captured using AMIRA.

To determine the photoacoustic volume from IR-1048 dye for each brain, the photoacoustic data set for each coronal image was co-registered with its respective ultrasound data set, and any PA signal located outside of the co-registered US coronal section was removed. The treated (right side) PA signal area of each coronal section was determined based on the location of the PA signal within the image. Outliers from the location data set were removed as to eliminate any PA signal from the untreated (left) side of the brain that could have resulted from other sources, such as deoxygenated hemoglobin remaining within the vasculature post-perfusion. The area of PA signal was calculated by multiplying the total width and depth of the PA location data set in the image. After the area was calculated for each coronal image, volume was calculated by totaling the PA area for each brain and multiplying by the coronal image step size of 0.102 mm.

3.2.5 Histology and immunohistochemistry

After 3D US/PA imaging, brains were transferred to a solution of 30% sucrose and stored at 4ºC for five days. Brains were snap frozen, and 20 µm coronal sections were cut using a cryostat (Leica CM 1860, Leica Biosystems). For each brain, 48-60 sections were cut and analyzed, spanning a total region of 0.96-1.2 mm within the brain. Standard hematoxylin (Gill No. 2, Sigma-Aldrich) and eosin (VWR) (H&E) was performed. H&E pictomicrographs were captured using the bright field mode of a Zeiss AxioObserver Z1 Microscope. Immunohistochemistry (IHC) was also performed using a secondary antibody of goat anti-mouse immunoglobulin G (IgG, H+L) tagged with Alexa Fluor 488 (Invitrogen) and 4',6-diamidino-2-phenylindole (DAPI, Invitrogen). IHC pictomicrographs were captured with a Zeiss Laser Scanning Confocal Microscope 700.

Zen lite software (Zeiss) was used to evaluate the fluorescence area of the IHC pictomicrographs of each animal. Fluorescence area was calculated using the profile view in the Zen lite software. Using a rectangular profile, IgG fluorescence signal was displayed across each coronal slice and thresholded to remove background noise. The area of IgG fluorescence was then calculated based on the location of above-threshold fluorescence.

3.3 Results

3.3.1 IR-1048 laser-activated PFHnD characterization

Lipid shelled, IR-1048 perfluorohexane nanodroplets (PFHnDs) were characterized by size, charge, and UV-VIS-NIR absorbance as shown below (Figure 8). PFHnDs had an average diameter of 265 ± 64.7 nm and a charge of -5.2 ± 4.4 mV in PBS (pH 7.4) (Figure 8A-B). When activated, PFHnDs are expected to expand to 1.25 μm (5X their nanodroplet diameter), putting theses activated droplets in the size range of microbubbles used for FUS BBB opening [72, 97]. The optical absorbance spectrum measured for IR-1048 PFHnDs shows a peak optical absorption near 1064 nm, the wavelength used for laser-activation of PFHnDs (Figure 8C). Irradiation at 1064 nm allows for increased light penetration in tissue, enabling activation of PFHnDs at increased depths [75, 111]. Evans Blue (EB), the dye co-administered with PFHnDs in *in vivo* experiments to qualitatively and macroscopically evaluate BBB opening, has a peak optical absorption near 600 nm and minimal absorption at 1064 nm. As a result, EB will not interact with the 1064 nm laser light used for laser-activated PFHnD BBB opening and *ex vivo* imaging.

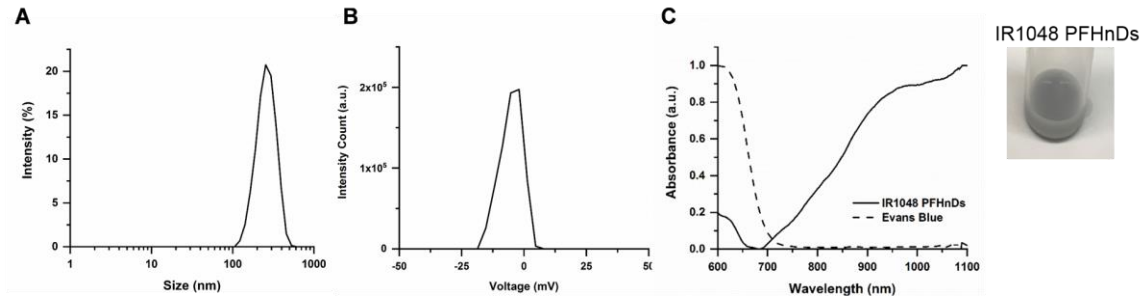

Figure 8. Characterization of IR-1048 perfluorohexane nanodroplets (PFHnDs). (A) IR-1048 PFHnD size distribution, 265 ± 64.7 nm. (B) Zeta potential of IR-1048 PFHnDs, -5.2 ± 4.4 mV. (C) Normalized absorbance spectrum of IR-1048 PFHnDs with a peak optical absorption near 1064 nm and Evans Blue dye with a peak optical absorption near 600 nm. Image to the right shows appearance of IR-1048 PFHnDs, and Evans Blue can be seen in Figure 4. Both IR-1048 PFHnDs and Evans Blue are used for *in vivo* blood brain barrier opening experiments.

3.3.2 Evans Blue extravasation and histological analysis of blood brain barrier opening induced by laser-activated PFHnDs

Evans Blue extravasation and hematoxylin and eosin (H&E) staining was compared for each animal group based on the number of laser pulses used (Figure 9). EB extravasation provides a macroscopic view of BBB opening, and H&E staining evaluates the tissue for damage, with red blood cells (RBCs) in the tissue indicating microhemorrhages [25]. For 0 laser pulses, i.e., no laser irradiation, no EB extravasation was visible nor were there any abnormalities in the stained tissue (Figure 9A). At 300 laser pulses, EB extravasation is visible in the top-view photograph and coronal cross-section photograph, as indicated by the white, dashed oval, outlining the EB extravasation area (Figure 9B). H&E staining shows no differences between the treated (right) and untreated (left) sides of the brain (Figure 9B). When 600 laser pulses are used, EB extravasation is evident, and H&E staining shows some RBC extravasation, denoted by the bright red staining in the tissue slice (Figure 9C). With 1200 laser pulses, EB extravasation is also

apparent in both the top view and coronal cross-section images (Figure 9D). However, in this group, RBC extravasation was not found, and both treated (right) and untreated (left) tissue were the same (Figure 9D). As the number of laser pulses increases from 300 to 600, there is an increase in EB extravasation in both the top view and coronal cross-section photographs (Figure 9B-C). From 600 to 1200 laser pulses, there appears to be a similar EB extravasation footprint from the top view photographs, however, there is an increase in the area of EB extravasation in the coronal cross-section images from 600 to 1200 laser pulses (Figure 9C-D).

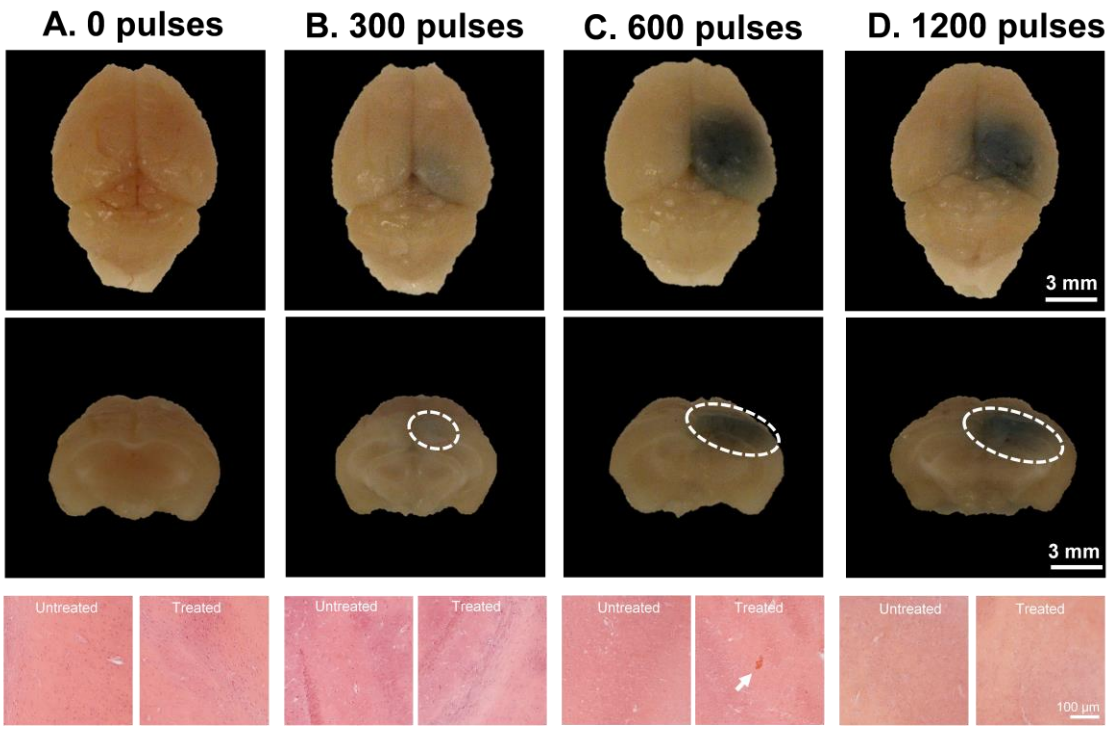

Figure 9. Representative Evans Blue (EB) dye extravasation top view and cross-sectional photographs and hematoxylin & eosin (H&E) pictomicrographs for varying number of laser pulses. EB dye extravasation is outlined on the coronal cross-section with a white, dashed oval. H&E pictomicrographs are shown for both treated (right) and untreated (left) sides of the brain, with presence of red blood cells indicated by a white arrow and bright red staining within the tissue. Number of laser pulses includes (A) 0 laser pulses, (B) 300 laser pulses, (C) 600 laser pulses, and (D) 1200 laser pulses. Note: Laser pulse Figure 9A and Figure 9C use the same images as laser fluence Figure 10A and Figure 10C, and experiments shown in (B-D) were performed at a laser fluence of 56 mJ/cm². Reprinted from [112].

Varying laser fluences were also evaluated for their effect on EB extravasation and H&E staining (Figure 10). As shown with 0 laser pulses, a fluence of 0 mJ/cm² (no laser irradiation) shows no EB extravasation or tissue abnormalities (Figure 9A, Figure 10A). When the laser fluence is increased to 38 mJ/cm², EB extravasation is evident in both the top view photograph and coronal cross-section photograph, where the EB extravasation of the coronal cross-section is outlined by a white, dashed oval (Figure 10B). H&E staining shows no differences between the treated and untreated sides of the brain (Figure 10B). In

the case of 56 mJ/cm², EB extravasation is widespread on the treated side of the brain, and RBC extravasation on the treated side is seen in H&E staining (Figure 9C, Figure 10C). At 70 mJ/cm², EB extravasation occurs, and the treated side of the brain shows RBC extravasation (Figure 10D). By increasing laser fluence, EB extravasation spread increases, and at higher fluences, RBC extravasation is present (Figure 10B-D).

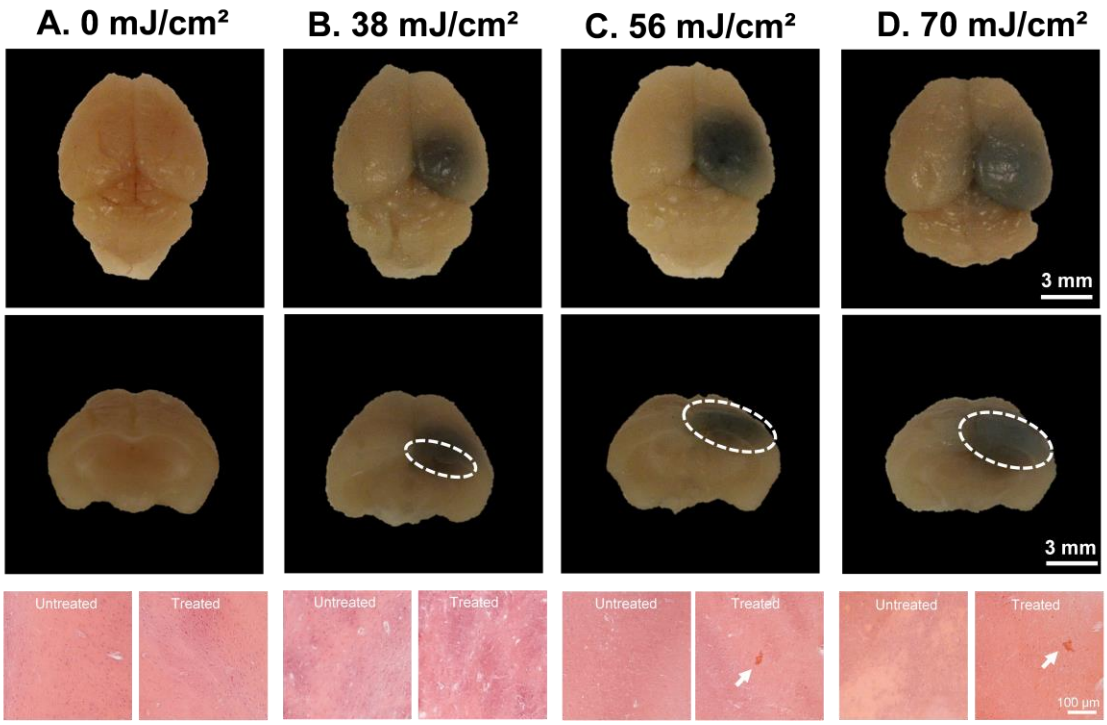

Figure 10. Representative Evans Blue (EB) dye extravasation top view and cross-sectional photographs and hematoxylin & eosin (H&E) pictomicrographs for varying laser fluences. EB dye extravasation is outlined on the coronal cross-section with a white, dashed oval. H&E pictomicrographs are shown for both treated (right) and untreated (left) sides of the brain, with presence of red blood cells indicated by a white arrow and bright red staining within the tissue. Laser fluences include (A) 0 mJ/cm², (B) 38 mJ/cm², (C) 56 mJ/cm², and (D) 70 mJ/cm². Note: Laser fluence Figure 10A and Figure 10C use the same images as laser pulse Figure 9A and Figure 9C, and experiments shown in (B-D) were performed with 600 laser pulses. Reprinted from [112].

In addition to H&E staining, immunohistochemistry was performed to examine the extravasation of the secondary antibody mouse immunoglobulin G (IgG). Mouse IgG has

a molecular weight of 150 kDa and will not extravasate unless the BBB is opened, as the molecular weight limit for the BBB is 500 Da [9, 113]. As can be seen with the whole brain, coronal section and magnified confocal pictomicrographs of the 0 laser pulses/ 0 mJ/cm² (no laser) case, fluorescence from DAPI is present, but there is minimal fluorescence signal from IgG (Figure 11A-B). Minimal fluorescence from IgG is seen in the untreated (left) side of the brain for all laser pulse and laser fluence variations (Figure 11A, C, E, G, I, K). In the animal groups where irradiation occurs, IgG fluorescence is visible throughout the treated (right side) region (Figure 11D, F, H, J, L). When the number of laser pulses is varied, fluorescent intensity from 0 laser pulses to 600 laser pulses increases (Figure 11B, F, H), but from 600 to 1200 laser pulses, the fluorescence signal does not seem to change (Figure 11H, J). A similar trend is observed for increasing laser fluence where fluorescence increases on the treated side from 0 mJ/cm² to 56 mJ/cm² and remains constant from 56 to 70 mJ/cm² (Figure 11B, D, H, L).

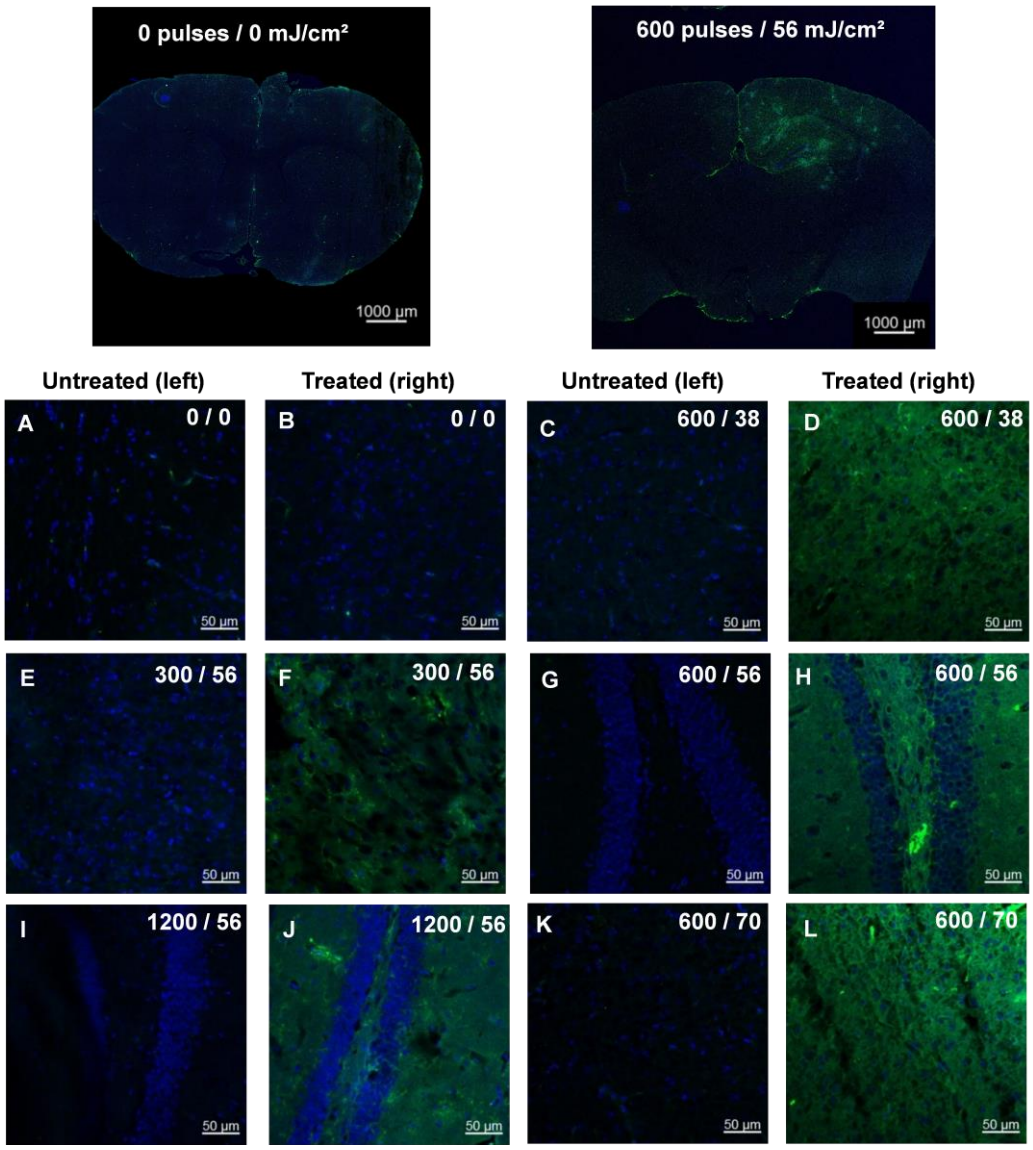

Figure 11. Immunohistochemistry staining for secondary antibody IgG and DAPI. The coronal sections displayed are representative images of overall IgG (green) and DAPI (blue) fluorescence while the magnified images display the difference in IgG fluorescence between the untreated (left) and treated (right) sides. Magnified images are labeled as number of laser pulses/laser fluence (mJ/cm²). Reprinted from [112].

3.3.3 Ultrasound and photoacoustic analysis of IR-1048 dye extravasation

Ex vivo ultrasound and photoacoustic (US/PA) imaging was performed, and 3D whole brain images were reconstructed to evaluate the volume of extravasated IR-1048 dye. This NIR absorbing dye is contained within the PFHnDs; however, when laser-

activated PFHnD BBB opening occurs, dye is able to extravasate across the BBB and produces a PA signal when imaged at its peak wavelength [84]. Reconstructed 3D US images are displayed in grayscale, and the reconstructed 3D PA signal is displayed using a hot colormap (Figure 12). At 0 pulses (no laser), there is minimal background PA signal present, but as the number of laser pulses increases from 300 to 1200 pulses, the volume of PA signal within the brain can be seen to increase in the treated (right side) of the brain.

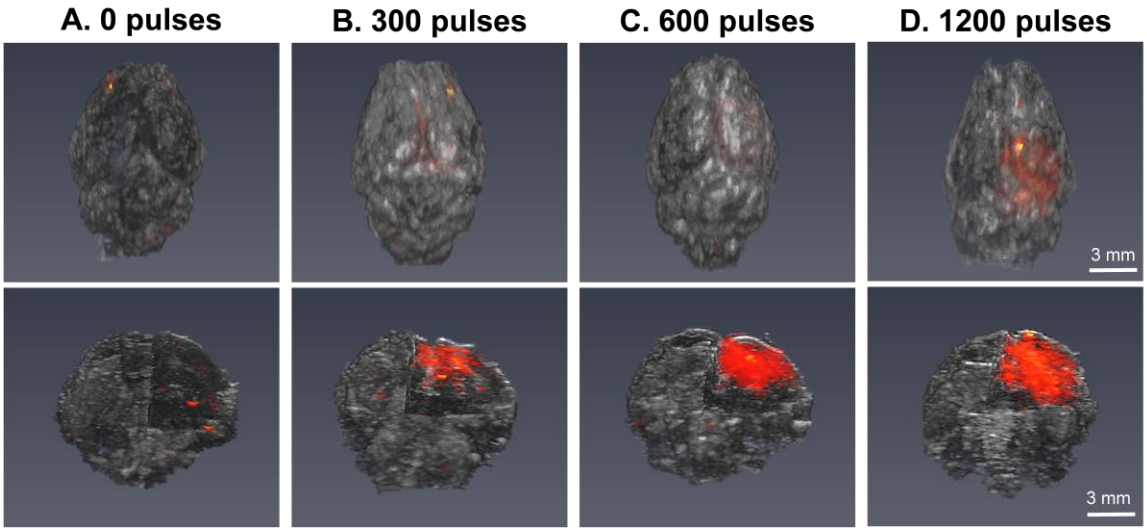

Figure 12. Reconstructed 3D top view and right side, corner cut images of ultrasound (US, grayscale) and photoacoustic (PA, hot colormap) data for varying number of laser pulses: (A) 0 pulses, (B) 300 pulses, (C) 600 pulses, and (D) 1200 pulses. Note: Laser pulse Figure 12A and Figure 12C use the same images as laser fluence Figure 13A and Figure 13C, and experiments shown in (B-D) were performed with a laser fluence of 56 mJ/cm². Reprinted from [112].

The trend in PA signal volume can also be examined as laser fluence is varied (Figure 13). At 0 mJ/cm² (no laser), there is minimal signal, and as laser energy increases from 38 mJ/cm² to 70 mJ/cm², the PA signal volume increases. Although the volume of PA signal at 70 mJ/cm² is increased, the overall PA signal intensity appears to be lower than the intensity at 56 mJ/cm² (Figure 13C-D).

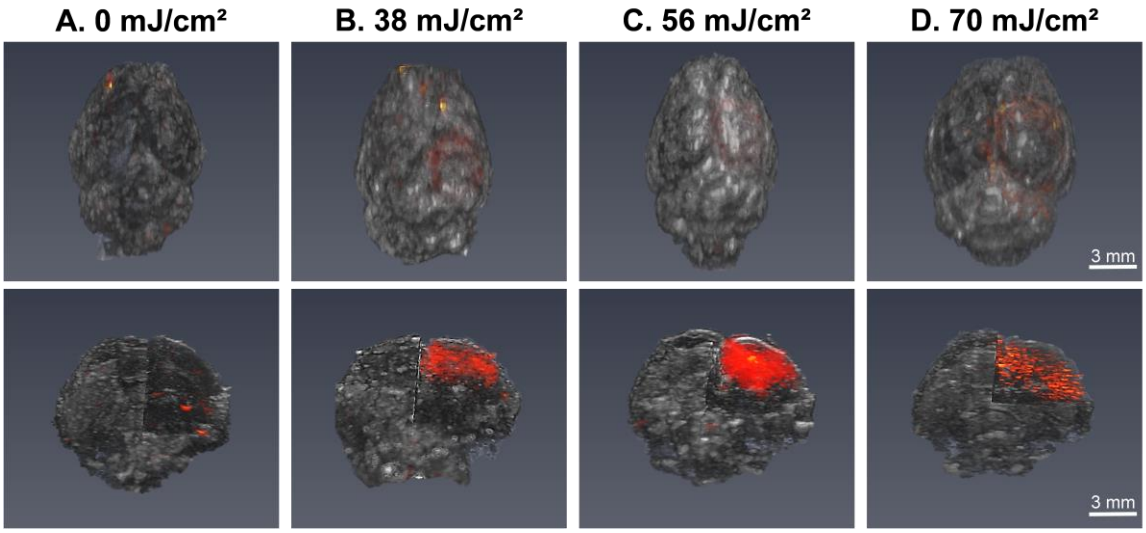

Figure 13. Reconstructed 3D top view and right side, corner cut images of ultrasound (US, grayscale) and photoacoustic (PA, hot colormap) data for varying laser fluences: (A) 0 mJ/cm², (B) 38 mJ/cm², (C) 56 mJ/cm², and (D) 70 mJ/cm². Note: Laser fluence Figure 13A and Figure 13C use the same images as laser pulse Figure 12A and Figure 12C, and experiments shown in (B-D) were performed with 600 laser pulses. Reprinted from [112].

3.3.4 Quantitative fluorescence and photoacoustic analysis

Quantitative analysis of fluorescence signal from IgG and PA signal from IR-1048 dye was completed for the five animal groups where laser irradiation was performed (Figure 14). The fluorescence area and PA volume were not calculated for the no laser (0 laser pulses, 0 mJ/cm²) case, as there is no calculable fluorescence area or PA volume for this animal group. Examining the number of laser pulses from 300 to 600 pulses, there is an increase in fluorescence area (Figure 14A). However, fluorescence area measurements from 600 to 1200 pulses are similar in mean and median, potentially indicating a saturation point with regards to the area over which IgG is delivered to the tissue as the number of laser pulses increases. When the laser fluence is increased, the fluorescence area also increases (Figure 14B). With PA volume measurements, similar trends are seen (Figure

14C-D). There is an increase in PA volume as the number laser pulses increases from 300 to 600 pulses, but there is not an increase when comparing 600 to 1200 laser pulses. As the laser fluence is increased from 38 mJ/cm² to 56 mJ/cm² to 70 mJ/cm², the PA volume increases.

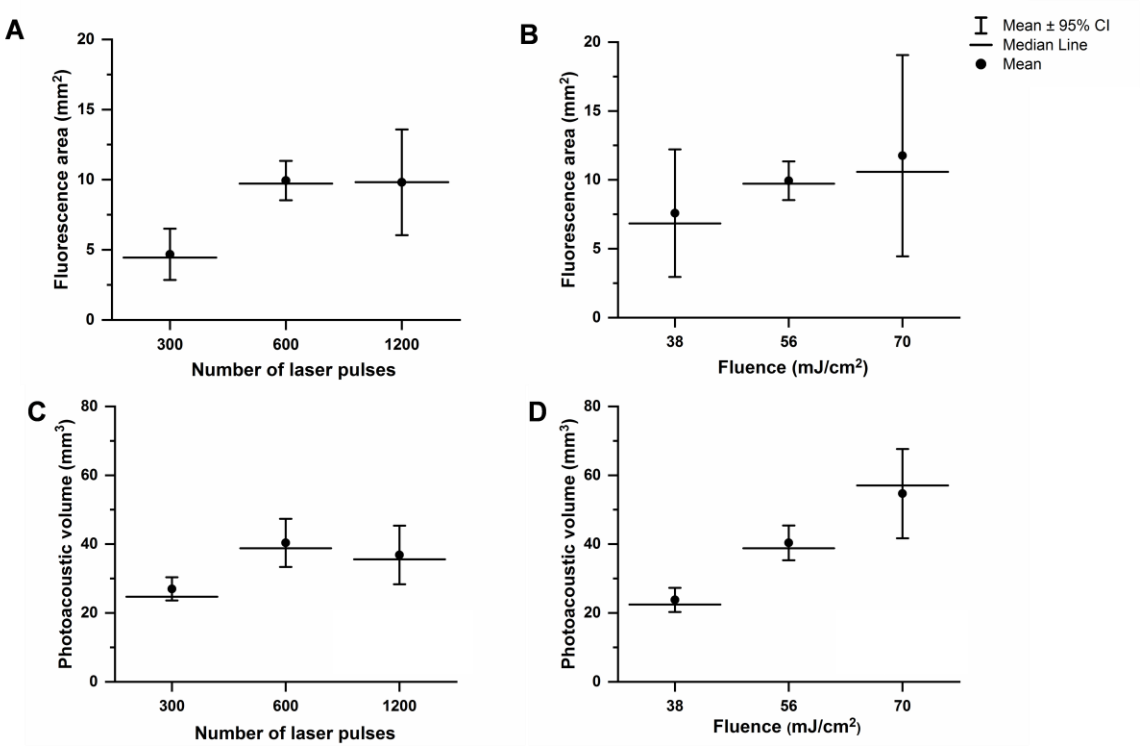

Figure 14. Quantitative evaluation of fluorescence area and photoacoustic volume for the varying number of laser pulses and laser fluences used. (A) Fluorescence area vs. number of laser pulses for 300, 600, and 1200 pulses. (B) Fluorescence area vs. fluence for 38, 56, and 70 mJ/cm². (C) Photoacoustic volume vs. number of laser pulses for 300, 600, and 1200 laser pulses. (D) Photoacoustic volume vs. fluence for 38, 56, and 70 mJ/cm². The circle marker indicates the mean value calculated for each animal group. The horizontal line identifies the median, and the vertical line marked with crossbars identifies the 95% confidence interval. Reprinted from [112].

3.4 Discussion

Through the variation of a range of laser fluences and laser pulses, the extent of laser-activated perfluorohexane nanodroplet (PFHnD) induced blood brain barrier (BBB) opening was controlled. BBB opening was evaluated through Evans Blue (EB) staining of the tissue, fluorescence produced by the secondary antibody IgG, and photoacoustic (PA) signal produced by IR-1048 dye. Damage to the tissue indicated by RBC extravasation was also evaluated to determine which range of laser fluences and laser pulses was safe (Figure 9 - Figure 10). Overall, it was seen that the extent of BBB opening increased with increased laser fluence (Figure 14B, D). When the number of laser pulses was increased from 300 to 600 pulses, there was an increase in fluorescence area and PA volume (Figure 14A, C). However, the trend in BBB opening remained constant when the number of laser pulses was increased from 600 to 1200. The results of these studies show how BBB opening can be modulated through the choice of laser parameters used for activation of PFHnDs.

The increased extent of BBB opening for increased laser fluence used is expected. Due to the optical properties of tissue, the ability of light to penetrate tissue and vaporize the droplets is in part dependent on the amount of laser fluence used [111]. Therefore, an increased laser fluence used in laser-activated PFHnD induced BBB opening can result in increased depth penetration, and this increased fluence will likely activate more PFHnDs, causing BBB opening in a larger volume within the tissue. This tissue-fluence interaction may also explain the trend seen when the number of laser pulses is increased. Although an increased number of pulses will allow for an increased number of PFHnD droplet phase changes or oscillations, which may help to increase BBB opening, the laser fluence footprint is expected to be the same when the same fluence is used. As a result, there is

likely to be a limit to the extent of BBB opening when the same fluence is used but the number of laser pulses is increased.

Furthermore, it is important to note that there were some cases where red blood cell extravasation occurred. When 56 mJ/cm² and 600 laser pulses were used, RBC extravasation was apparent in the tissue (Figure 9C, Figure 10C). In addition, at 70 mJ/cm² and 600 laser pulses, RBC extravasation was visible (Figure 10D). Thus, choosing lower fluences may be optimal to enable effective BBB opening without damage to the tissue. Interestingly, at 1200 laser pulses and a fluence of 56 mJ/cm², RBC extravasation was not seen (Figure 9D). There are a few possibilities as to why 1200 pulses did not show damage, such as variation per animal or slight differences in the PFCnD size distribution synthesized for each set of experiments. However, the trends seen in Evans Blue extravasation, IgG fluorescence, and IR-1048 dye delivery show that these slight differences have not affected the outcome of BBB opening, suggesting that damage should be seen in the 1200 laser pulse group (Figure 9D, Figure 11I, J, Figure 12D). As a result, the upper limit or guideline for safe, laser-activated PFHnD induced BBB opening, given these experiments, should be the lowest laser fluence and laser pulse number to show RBC extravasation, which is 56 mJ/cm² and 600 laser pulses.

Other parameters can also be explored to optimize laser-activated PFCnD induced BBB opening. With regard to laser parameters, the laser pulse repetition frequency (PRF) could be modified. In these studies, a laser PRF of 10 Hz was used. A lower PRF would increase the time between phase change events, potentially reducing the concentration of phase-changing PFHnDs within the laser irradiated volume which may help to reduce tissue damage seen at higher fluences. Laser irradiation wavelength could also be adjusted.

The current wavelength of 1064 nm used was selected for increased depth penetration into tissue, but other NIR absorbing wavelengths could be used. Regardless, effectiveness and extent of BBB opening would be dependent upon the peak absorption wavelength of the optical trigger within PFCnDs, so wavelength used should coincide with the optical trigger. PFCnD parameters would also affect BBB opening [96, 100], similar to how microbubbles affect BBB opening [19, 21, 22, 26]. Parameters such as PFCnD size, concentration, perfluorocarbon core, and encapsulated optical trigger can also affect the safety and efficacy of laser-activated PFHnD induced BBB opening. Overall, these studies focused on laser fluence and laser pulses used and provide a guideline to how PFCnD BBB opening can be controlled through laser irradiation. Nevertheless, there is still space to improve upon laser-activated PFCnD BBB opening, primarily through exploration of PFCnD parameters.

A fully optimized laser-activated PFCnD induced BBB opening would allow laser-activated PFCnDs to act in multiple roles in the monitoring and treatment of neurological diseases. US/PA imaging of extravasated photoacoustic contrast in the brain *in vivo* has been established [81, 114], and therefore PFCnDs could contribute to not only BBB opening but also US/PA contrast within the brain. Contrast provided via laser-activated PFCnDs could enable monitoring of BBB opening as well as monitoring of the delivery of any cargo, therapeutic or diagnostic, contained within PFCnDs. In addition, laser-activated PFCnD induced BBB opening would allow for delivery of other PA contrast agents, possibly furthering the capabilities of longitudinal or multiplexed US/PA imaging within the brain. Altogether, laser-activated PFCnD induced BBB opening and the versatility of

PFCnDs have the potential to play a significant role in US/PA imaging and therapy in the central nervous system.

CHAPTER 4. *IN VITRO* EXAMINATION OF PHOTOACOUSTIC CONTRAST AGENTS FOR ULTRASOUND AND PHOTOACOUSTIC IMAGING OF THE BRAIN

4.1 Introduction

Photoacoustic (PA) imaging relies on the optical absorption properties of the target being imaged [57, 115]. In the case of biomedical imaging, PA contrast can be produced via endogenous absorbers such as hemoglobin and melanin or from exogenous contrast agents such as optically absorbing dyes or metal nanoparticles [50, 51, 53]. In the last decade, PA imaging of the brain has emerged as a neuroscience tool that has relied on both endogenous and exogenous contrast imaging [58-62]. However, PA neuroimaging has often been limited to the vasculature or leaky tumors with limited studies being performed for extravascular contrast agent delivery [63-65, 116, 117]. As a result, there is a need to explore extravascular PA contrast delivery in the brain.

Recently, tools for focused ultrasound (FUS) blood brain barrier (BBB) opening and *in vivo* ultrasound and photoacoustic (US/PA) imaging of delivered PA contrast with gold nanorods (AuNRs) have been developed [81]. Although delivery and imaging were successful, there were some limitations with respect to the PA contrast agent employed, i.e., AuNRs. Specifically, AuNRs are required to be delivered in high concentrations for sufficient PA imaging. These particles are neither biodegradable nor sufficiently cleared which brings concerns with regard to cytotoxicity and safety [118]. Furthermore, due to

their synthesized shape, AuNRs are prone to melting upon repeated pulsed laser irradiation which alters their absorption spectrum and limits their repeated or long term use [86].

Another solid nanoparticle more promising for use as a PA imaging contrast in the brain is the copper sulfide nanoparticle (CuS NP). CuS NPs are photothermally stable, inorganic, semi-conductor nanoparticles that optically absorb in the second optical imaging window, near 1064 nm [119, 120]. CuS NPs are non-cytotoxic, biodegradable, and are cleared in a reasonable time frame [121]. As a nanoparticle providing stable PA contrast, CuS NPs appear promising for extravascular brain imaging.

In addition to dyes or metallic nanoparticles, which produce a stable PA signal when imaged, dynamic nanoparticles, or phase change nanoparticles, can also be utilized for extravascular imaging in the brain. In particular, the phase change behavior of PFCnDs can not only be used to induce BBB opening but can also be used to provide dual US/PA imaging contrast [30, 74, 80, 82, 85, 86, 90]. Two subsets of laser-activated PFCnDs are of particular interest for use as dynamic US/PA contrast agents. Perfluoropentane nanodroplets (PFPnDs) with a bulk boiling point near physiological temperature (29ºC) produce a permanent, single phase change event from liquid droplet to stable gas bubble upon pulsed laser irradiation [83]. The behavior of laser-activated PFPnDs can be imaged over the course of seconds to provide information about the location of droplets in the imaging plane with respect to the background [30, 82]. PA signal of PFPnDs is highest in the first seconds, followed by a steady decline in signal [30, 82]. On the other hand, US signal is lowest in the first seconds, followed by a steady increase in signal and corresponding saturation of signal due to the vaporization of all PFPnDs in the imaging plane [30, 82]. Perfluorohexane nanodroplets (PFHnDs), with a bulk boiling point above

physiological temperature (57ºC) are also of interest for US/PA imaging in the brain, as they provide dynamic US contrast that can be localized through the use of different imaging algorithms due to their ability to repeatedly phase change [74, 91]. Through the use of laser-activated PFCnDs, dual US/PA image contrast is available, a benefit over agents that provide only PA or US image contrast.

To examine the behavior of PA image contrast agents longitudinally, *in vitro* studies can be used to evaluate PA contrast agents in a high throughput manner [122-125]. Incubating nanoparticles with cells followed by US/PA imaging can provide information regarding the interaction of specific nanoparticles and cells. To evaluate PA contrast in the brain with *in vitro* studies, microglial cell lines are of interest. Microglial cells are the innate immune cells within the brain and act similarly to macrophages and lymphocytes in other parts of the body to protect the brain from disease and injury [126-128]. They comprise 12% of the brain and remain predominantly in a resting state unless activated by the surrounding microenvironment [126]. As a result, microglia are likely to be first responders when interacting with foreign materials, such as nanoparticles for PA imaging [126, 128]. One particular microglial cell line that is ideal for yielding a large number of cells quickly, enabling an extensive evaluation of PA contrast agents, is the BV-2 cell line, which originates from murine microglia [127, 129]. BV-2 cells have been evaluated as an appropriate alternative to primary microglia cultures [127, 129] and act as a suitable cell culture model for studying extravascular PA contrast *in vitro*.

In the studies outlined below, two nanoparticle types are incubated with BV-2 cells. CuS NPs provide stable photoacoustic contrast, and laser-activated PFPnDs are evaluated with their dynamic, dual US/PA imaging contrast. These two PA contrast agents are

examined at different time points to determine which particles are ideal for US/PA imaging in the brain.

4.2 Materials and methods

4.2.1 Synthesis and characterization of copper sulfide nanoparticles (CuS NPs)

Copper sulfide nanoparticles (CuS NPs) were synthesized as described previously [130], followed by silica and poly-L-lysine (PLL) coating. Prior to all reactions, glassware was rinsed with nanopure water and cleaned with aqua regia. Into 250 mL of nanopure water, one mmol of Copper(II) chloride (Sigma-Aldrich) was added followed by 0.68 mmol of sodium citrate (Sigma-Aldrich). One molar sodium sulfide (Sigma-Aldrich) was then added to the solution, turning it from a blue to brown color. The reaction was allowed to stir for 5 minutes at room temperature and was then moved to a 90 ºC water bath and stirred at 900 rpm for 15 minutes, with the solution turning a hunter green color. After 15 minutes, the solution was transferred to an ice-cold water bath to cool. Cooling of the CuS NP solution was followed by pegylation of CuS NPs with a 1:1 ratio of PEG-SH (5 kDa, Laysan Bio). CuS NPs and PEG-SH were left to mix overnight.

After mixing, pegylated CuS NPs were washed via centrifugation. Silica coating was then performed by mixing 2 mL of optical density (OD) 15 CuS NPs with 3 mL of isopropyl alcohol (IPA) in a 20 mL scintillation vial at 400 rpm. A 1.2 mL, 3% solution of tetraethyl orthosilicate (Sigma-Aldrich) in IPA was added to the vial followed by 1.2 mL of ammonium hydroxide (VWR). The reaction was allowed to stir for 2 hours. The resulting solution was washed twice at 500 rcf for 15 minutes before being resuspended in 4 mL of nanopure water and sent through a 0.20 µm sterile filter.

Silica coated CuS NPs were then prepared for PLL coating by diluting them to ~2 OD. Following dilution, 0.833 mM PLL (Sigma-Aldrich) was added per milliliter of CuS NPs. The solution was sonicated for one minute and left at room temperature for two hours. PLL coated CuS NPs were then washed twice via centrifugation at 500 rcf for 5 minutes. CuS NPs were then resuspended in PBS and stored at 4ºC prior to cell studies.

CuS NP size and zeta potential were measured in PBS (pH 7.4) using a dynamic light scattering instrument (Zetasizer Nano ZS, Malvern Instruments Ltd.). A spectrophotometer (Evolution 220, Thermo Scientific) was used to measure the absorbance of the CuS NPs.

4.2.2 Synthesis and characterization of laser-activated 760 nm perfluoropentane nanodroplets (PFPnDs)

Perfluoropentane nanodroplets (PFPnDs) were synthesized using a 760 nm absorbing dye (Epolight 9151, Epolin, Inc.), perfluoropentane (FluoroMed, L.P.), and a lipid shell comprised of 1,2-distearoyl-sn-glycero-3-phosphoethanolamine-N-[amino(polyethylene glycol)-2000] (DSPE-PEG(2000), 25 mg/mL, Avanti Polar Lipids, Inc.) and 1,2-distearoyl-sn-glycero-3-phosphocholine (18:0 PC (DSPC), 25 mg/mL, Avanti Polar Lipids). To create the lipid shell, 40 µL of DSPE-PEG(2000) and 8 µL of 18:0 PC (DSPC) were added to a 10 mL pear-shaped flask (Sigma-Aldrich). A 760 nm dye solution was prepared in chloroform (1 mg/mL), and 200 µL was added to the flask. An additional 1 mL of chloroform was added to the flask to enable a smooth lipid cake. A rotary evaporator (Rotovapor, Büchi) was used at reduced pressure to remove the chloroform from the flask leaving a 760 nm dye-coated lipid cake. The lipid cake was

resuspended in 1 mL of PBS using a water bath sonicator (VWR, 180W). The solution was placed in a 7 mL scintillation vial, and 150 µL of PFP was added. The vial was vortexed for 10 seconds (Vortex Mixer, Fisher Scientific) and sonicated for five minutes in an ice-cold water bath (VWR, 180 W). The PFPnD solution was transferred to a 2 mL centrifuge tube and centrifuged for 60 seconds in a mini-centrifuge (Mini-Spin, Eppendorf) to remove excess PFP and 760 nm dye. The supernatant was transferred to a new 2 mL centrifuge tube, and the pellet was discarded. Prior to cell studies, 760 nm PFPnDs were stored at 4ºC.

The PFPnD size and zeta potential were measured in PBS similarly to CuS NPs as mentioned in section 4.2.1. 760 nm dye in chloroform was also measured to characterize the absorbance spectrum (Evolution 220, Thermo Scientific) of the 760 nm PFPnDs.

4.2.3 BV-2 cell culture and nanoparticle incubation

BV-2 cells were cultured in a 1:1 Dulbecco's Modified Eagle Medium and Ham's F-12 (DMEM:F12) + L-glutamine media (VWR) supplemented with 5% heat-inactivated fetal bovine serum (FBS) and 1% penicillin-streptomycin. Heat-inactivation of FBS was performed by leaving FBS in 56ºC water for 30 minutes. Cells were passaged every 3 days using a cell scrapper at a subcultivation ratio of 1:20. For incubation with nanoparticles, cells were cultured to 60% confluence.

CuS NPs and 760 nm PFPnDs were prepared in PBS for incubation with BV-2 cells. All nanoparticles were sterilized via UV light for 30 minutes. Three cell groups were cultured for the US/PA imaging experiments – cells containing CuS NPs, cells containing 760 nm PFPnDs, and control cells with no incubated nanoparticles. One mL of CuS NPs were incubated with BV-2 cells at an OD of 1.8 (~3×10^{13} nanoparticles/mL [130]) while

one mL of 760 nm PFPnDs were incubated with BV-2 cells at a ratio of 1:1000 from stock solution (~10^{10} nanoparticles/mL [84]). At cell and nanoparticle incubation time points of t = 4 hours and 24 hours, cells were fixed and prepared for ultrasound and photoacoustic imaging.

4.2.4 Ultrasound and photoacoustic imaging of PA labeled BV-2 cells

Ultrasound and photoacoustic imaging were performed using a tissue-mimicking gelatin inclusion phantom. Cell-containing gelatin inclusions were made by diluting cells 1:1 in a 16% solution of gelatin such that 20 µL of the solution contained 2.5 x 10^4 cells. The cell-gelatin mixture was then pipetted onto an 8% gelatin base in a plastic container to form a dome-shaped cell inclusion (Figure 15). For the cell and nanoparticle incubation time point t = 4 hours, nanoparticle labeled cell inclusions of CuS NPS, 760 nm PFPnDs, and control cells without nanoparticles were prepared. For the incubation time point of t = 24 hours, only nanoparticle containing cell inclusions were prepared.

US/PA imaging at the two incubation time points was performed by filling the phantom container with degassed water. Phantom inclusions were imaged with a photoacoustic and ultrasound imaging system (Vevo LAZR, FUJIFILM VisualSonics Inc.) with a 40 MHz ultrasound and photoacoustic imaging probe (LZ-550, FUJIFILM VisualSonics Inc.). The system's tunable ND:YAG laser (20 Hz, 5-7 ns pulse length) was operated at two wavelengths. US/PA imaging of the CuS NP labeled cells was performed at a wavelength of 1064 nm and at a fluence of 24 mJ/cm². US/PA imaging of the 760 nm PFPnD labeled cells was performed at a wavelength of 760 nm and at a fluence of 22 mJ/cm². Imaging was performed at a US/PA frame rate of 5 frames per second.

Spectroscopic US/PA imaging was also performed for labeled cells at t = 4 hours. Each set of labeled cells was imaged at a range of wavelengths from λ = 680 nm to 970 nm at increments of 5 nm using the Vevo LAZR system described previously. Data acquired from US/PA imaging was exported and processed using MATLAB (Mathworks). Data was collected for multiple inclusions of each labeled cell group (n = 3 imaged gelatin inclusions per group).

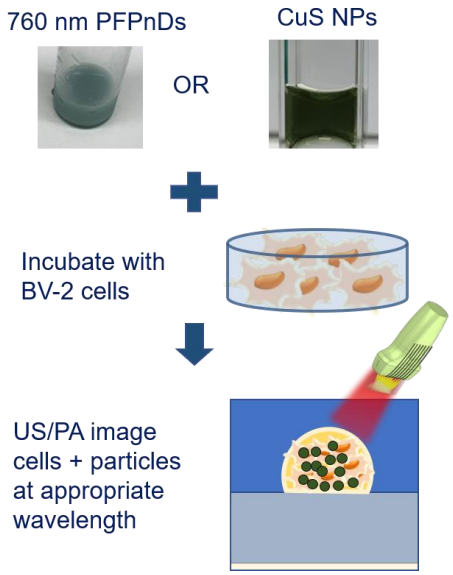

Figure 15. Depiction of ultrasound and photoacoustic (US/PA) imaging of labeled BV-2 cells. Two types of nanoparticles were incubated with BV-2 cells for various time points, followed by US/PA imaging of the nanoparticle labeled cells.

4.3 Results

4.3.1 Characterization of dynamic and stable nanoparticles

Prior to incubation with cells, the two nanoparticles were characterized by absorbance, size, and zeta potential (Figure 16). CuS NPs have peak absorbance near 1064 nm, making 1064 nm a suitable wavelength for laser irradiation of these particles. PFPnDs

have a peak absorbance near 760 nm, making 760 nm a preferred wavelength for laser irradiation of the 760 nm PFPnDs (Figure 16A) . With respect to size, 760 nm PFPnDs had the largest diameter, at 342 nm. PLL, silica coated CuS NPs had a peak diameter of 164 nm (Figure 16B). Zeta potential for the nanoparticles varied slightly, with the lipid-based nanoparticle being negatively charged (760 nm PFPnDs peak voltage = -10.3 mV) and the solid nanoparticle being positively charged (CuS NP peak voltage = 6.03 mV) (Figure 16C).

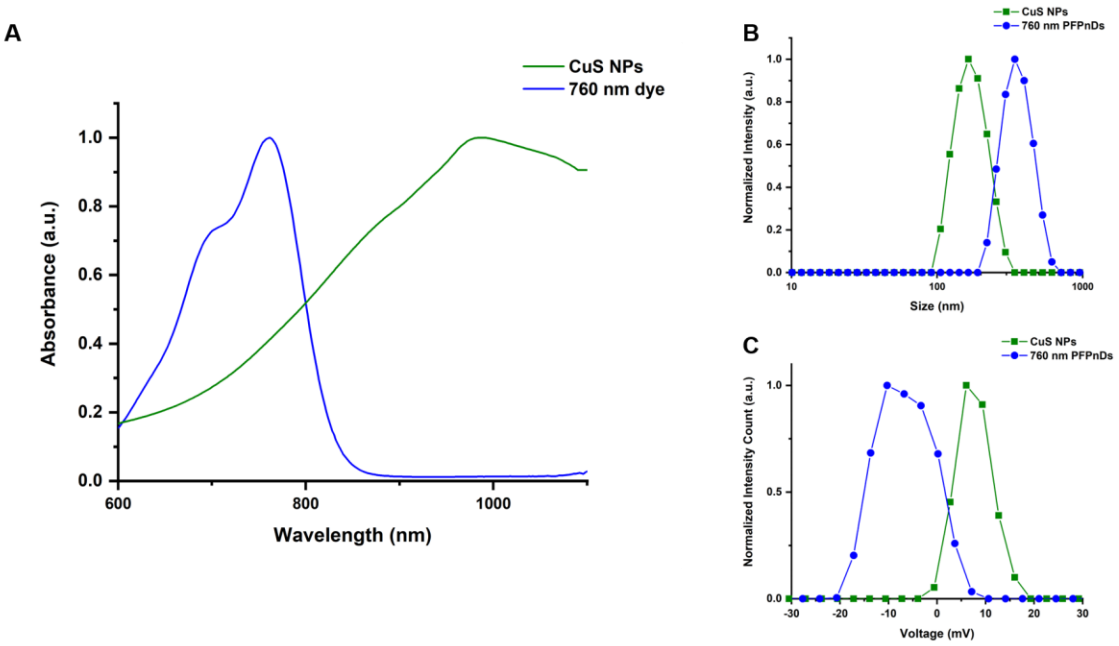

Figure 16. Characterization of copper sulfide nanoparticles (CuS NPs) and 760 nm perfluoropentane nanodroplets (760 nm PFPnDs). (A) Absorbance spectrum of CuS NPs having a peak absorption around 1064 nm and the 760 nm dye used in PFPnDs having a peak absorption near 760 nm. (B) Size distributions for the two nanoparticle types. (C) Zeta potential for the two nanoparticle types.

4.3.2 Evaluation of the photoacoustic signal from dynamic and stable nanoparticles

US/PA imaging of the BV-2, nanoparticle labeled cell inclusions allowed for evaluation of nanoparticle behavior at different time points. Specifically, PA signal, as

denoted by the hot colormap, evaluated for 760 nm PFPnDs over the nanoparticle incubation time points of t = 4 hours and 24 hours shows a decrease in signal as incubation time increases (Figure 17, Figure 18). On the other hand, the PA signal for CuS NPs from 4 to 24 hours remains approximately constant. The control cells, imaged at laser irradiation wavelengths of 760 nm and 1064 nm, show minimal to no signal within the dome shaped gelatin inclusion. For the different nanoparticles incubated with cells, PA signal intensity does vary, with 760 nm PFPnDs producing the higher intensity PA signals qualitatively in comparison to CuS NPs (Figure 17).

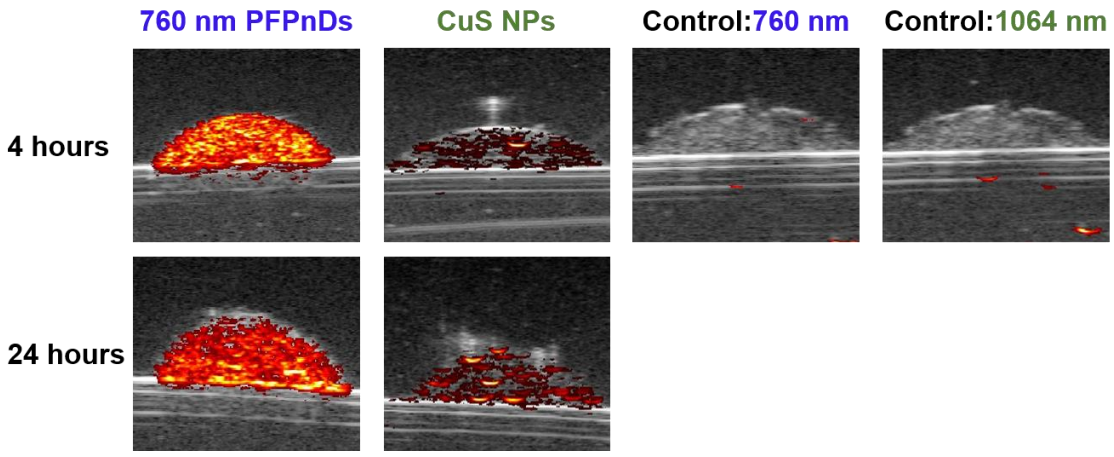

Figure 17. Ultrasound and photoacoustic imaging of BV-2 cells incubated with 760 nm perfluoropentane nanodroplets (PFPnDs) and copper sulfide nanoparticles (CuS NPs) and imaged at time points t = 4 and 24 hours. Cells were imaged at the peak wavelength of the incubated photoacoustic nanoparticle. i.e., 760 nm for 760 nm PFPnDs and 1064 nm for CuS NPs. Control cells (i.e., cells without photoacoustic nanoparticles) were imaged at both 760 nm and 1064 nm.

Looking at PA signal quantitatively can also show the trends seen above in Figure 17. Mean photoacoustic signal was calculated by averaging a PA region of interest (ROI) within the cell containing inclusion of the first image frame collected. This mean PA signal was then averaged with the PA ROIs of the first image frame collected from two other cell

containing inclusions of the same nanoparticle type. Thus, three cell inclusions were imaged for each nanoparticle group. PA signal was also normalized for each nanoparticle group to highlight the trends in signal change from 4 hours to 24 hours. Due to the size of the data sets, photoacoustic signal and normalized photoacoustic signal was plotted, showing the mean, median, and 95% confidence interval for each nanoparticle labeled group (CuS NPs, 760 nm PFPnDs, and Control Cells) and time point (4 and 24 hours).

Overall, average PA signal is the highest for the 760 nm PFPnDs incubated with BV-2 cells (Figure 18A). However, there is a decrease in the mean PA signal from t = 4 hours to 24 hours for 760 nm PFPnDs, approximately a 30% decrease (Figure 18B). CuS NPs incubated with BV-2 cells produce a lower PA signal at both t = 4 hours and t = 24 hours compared to 760 nm PFPnDs. However, from t = 4 hours to 24 hours, signal from CuS NPs is approximately constant (Figure 18). In comparison to t = 4 hours, the mean CuS NP PA signal increases at 24 hours. Control cells imaged at t = 4 hours at laser irradiation wavelengths of 760 nm and 1064 nm show minimal PA signal coming from control cells incubated without PA sensitive nanoparticles.

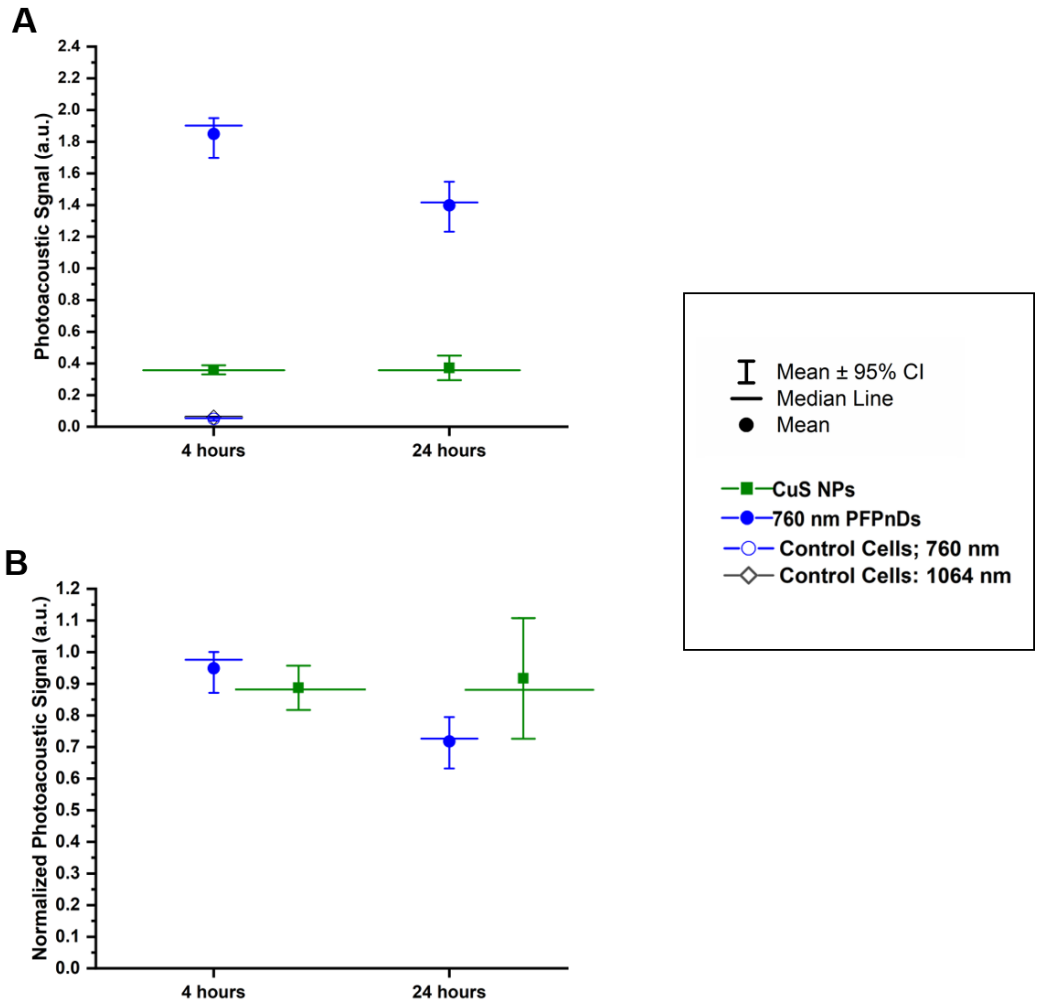

Figure 18. Photoacoustic (PA) signal for BV-2 cells incubated with 760 nm PFPnDs and CuS NPs and imaged at time points t = 4 and 24 hours. (A) PA signal is shown for each group of labeled cells, including both sets of control cells at t = 4 hours, and is described by the mean, median, and 95% confidence interval for each nanoparticle labeled cell group and time point. (B) Normalized PA signal is shown for each group of labeled cells and is described by the mean, median, and 95% confidence interval.

Photoacoustic signal for each set of labeled cells was also examined spectroscopically at t = 4 hours. Each set of labeled cells was imaged at a range of wavelengths from λ = 680 nm to 970 nm at increments of 5 nm. PA spectroscopic imaging was performed to evaluate the behavior of the nanoparticles when incubated with cells and

how this signal compares to the nanoparticle signal measured using the UV-VIS spectrophotometer for optical absorption (Figure 16A). Overall, the captured PA spectroscopic signals trend similarly to the absorbance spectra measured with the UV-VIS spectrometer with a few exceptions. CuS NPs have a broad PA spectrum, with relatively high PA signals from 680 nm to 970 nm. This trend is similar to the absorbance spectrum; however, relative absorbance is lower at wavelengths of 680-800 nm. Also, in comparison to the absorbance spectrum, peak PA signal for CuS NPs is slightly red-shifted, with peak PA signal falling in the 900 nm range. For 760 nm PFPnDs, PA signal has the two-peak behavior seen with the 760 nm dye absorbance spectrum, with peaks near 700 nm and 760 nm. However, both PA signal peaks from 760 nm PFPnDs are similar in relative PA signal in comparison to the absorbance spectra of 760 nm dye. The 760 nm PFPnDs show a sharp decrease in PA signal after 800 nm, also seen with the absorbance spectrum. Overall, examining both groups of nanoparticles labeled cells shows that each set of cells can be distinguished spectroscopically.

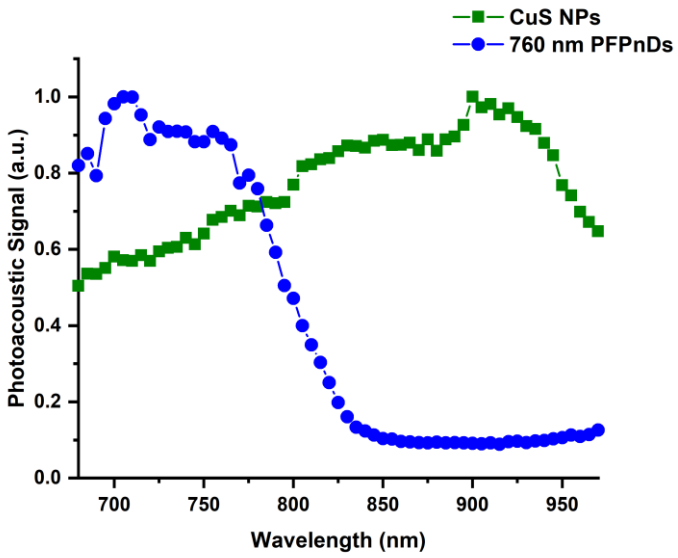

Figure 19. Spectroscopic photoacoustic signal for nanoparticle labeled cell inclusions at t = 4 hours. The CuS NP PA spectrum is shown in green squares while the 760 nm PFPnD spectrum is shown in blue circles.

In addition to longitudinal evaluation of US/PA signal from nanoparticle labeled cell inclusions, US/PA signal can also be evaluated over a shorter period of time, i.e., seconds. PA signal and ultrasound difference signal for each nanoparticle labeled cell inclusion was plotted over 4 seconds (Figure 20). US difference signal (ΔUS) was calculated by subtracting the US signal of cell inclusions before US/PA imaging and laser irradiation from the US signal acquired during US/PA imaging. In the case of cells labeled with a stable nanoparticle, such as CuS NPs, there should be little difference in US signal before and during irradiation. However, with dynamic nanoparticles like 760 nm PFPnDs which produce US contrast with laser irradiation, US signal should change. Thus, calculating the ΔUS provides information regarding how the US signal changes while removing any US signal that arises from the background.

Over the 4 second time interval, control cells imaged at 760 nm and 1064 nm show minimal PA signal due to the lack of an incubated PA sensitive particle, and therefore PA signal acquired at these wavelengths for control cells is due to noise (Figure 20). ΔUS is also minimal and relatively unchanging over time as the control cells experience no dynamic behavior. For the CuS NP labeled cells, both ΔUS and PA signals are constant (Figure 20). PA signals at t = 4 hours and 24 hours are similar over the 4 second interval in both behavior and signal intensity. The same can be said for ΔUS for CuS NP labeled cells. The difference in US signal of the CuS NP labeled cells is minimal and consistent over time. As a result, in an imaging session, CuS NPs produce stable PA contrast and no US contrast and continue to behave this way regardless of the imaging time point, t = 4 or 24 hours.

The PA and ΔUS signal of 760 nm PFPnD labeled cells show dynamic trends over time. PA signal for cells labeled with 760 nm PFPnDs steadily decreases over time, after an initial peak PA signal. This initial peak PA signal occurs with the first few laser pulses in PA imaging and results from the single phase change behavior of the PFPnDs. After PFPnDs in the imaging plane phase change, the PA signal appears lower and constant and is the result of the nanoparticle's photoabsorber producing PA signal [30, 75]. In addition, the PA signal produced at t = 4 hours is higher than the signal produced at t = 24 hours. ΔUS for 760 nm PFPnDs increases as time increases due to the phase change of these particles from liquid to gas, resulting in an echogenic US signal [30, 75]. Over time, the US signal begins to saturate due to laser irradiation of all of the particles in the imaging plane [30]. The ΔUS of 760 nm PFPnD labeled cells reduces at t = 24 hours in comparison to t = 4 hours. However, both time points show an initial ΔUS increase from 0 to 1 seconds,

followed by the signal saturating to a steady state. As a result, these nanoparticles continue to display characteristic dynamic US/PA behavior regardless of imaging time point.

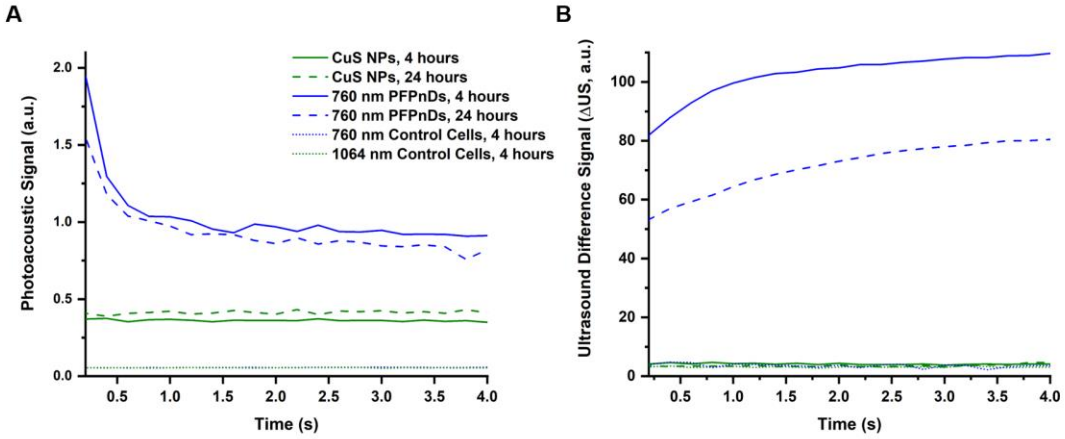

Figure 20. Photoacoustic and ultrasound difference signal (ΔUS) for each group of labeled BV-2 cells at t = 4 hours and 24 hours and for control cell groups imaged at 760 nm and 1064 nm for t = 4 hours. (A) PA signal tracked over 4 seconds of US/PA imaging. (B) ΔUS signal tracked over 4 seconds of US/PA imaging.

4.4 Discussion

By analyzing the interaction of different PA nanoparticles with BV-2 cells, an understanding of how these nanoparticles may react *in vivo* can be gained. Overall, CuS NPs maintained PA signal over time, with a slight increase in mean PA signal from t = 4 hours to t = 24 hours (Figure 18). The 760 nm PFPnDs produced the highest PA signal values, however, mean PA signal from t = 4 hours to t = 24 hours decreased. Furthermore, the behavior of nanoparticle labeled BV-2 cells was also evaluated over the course of seconds within the individual imaging session (Figure 20). CuS NPs showed no changes in PA or ΔUS signal when imaged over this short time scale. On the other hand, 760 nm PFPnDs showed dynamic behavior. That is, their PA and ΔUS signals showed identifiable

trends in signal change over time. Overall, the studies help to highlight the usefulness of each PA nanoparticle type for different imaging time scales.

Copper sulfide nanoparticles appear to be most promising for long-term US/PA imaging studies. PA signal from CuS NPs over the 24 hour time point compared to that of 760 nm PFPnDs remained steady, thus making them better potential candidates for imaging in situations where multi-day time points are used. Although there are advantages to using copper sulfide nanoparticles, there also appear to be a few disadvantages. For example, the PA contrast produced by CuS NPs was significantly reduced in comparison to that of 760 nm PFPnDs. The total number of CuS NPs incubated with BV-2 cells was estimated to be near 3×10^{13} nanoparticles, while the number of droplets used was estimated to be 1×10^{10} nanoparticles. The lower PA signal provided by CuS NPs suggests that an increase in concentration delivered to the cells would be required, creating some concern for future studies regarding nanoparticle overdose to obtain sufficient PA signal. Additionally, the synthesized CuS NPs used in these studies had a peak zeta potential that was positively charged, which may have affected the optimal uptake by BV-2 cells (Figure 16C). As phagocytic cells, like activated microglia, act preferentially with negatively charged particles, the positively charged CuS NPs uptake may have been reduced [131, 132]. As a result, CuS NPs appear to be favorable for long-term US/PA imaging studies of extravascularly delivered contrast agents but require further optimization prior to use.

The characteristics of 760 nm PFPnDs appear to be most ideal as a short term extravascular imaging agent. Their dynamic phase change behavior provides sufficient US/PA imaging contrast, allowing for localization of 760 nm PFPnDs within the tissue. They are also triggered and imaged at 760 nm whereas PFHnDs used for BBB opening are

triggered at 1064 nm, reducing overlap between the PA signal used to evaluate extravasation (1064 nm) and the PA signal of the 760 nm PFPnDs. The 760 nm PFPnDs present a few limitations for longitudinal study but could also be optimized to improve their utility. The current peak diameter of 342 nm does reduce the number of PFPnDs capable of extravasating across the BBB. However, laser-activated PFHnD induced BBB opening has shown extravasation of micron sized red blood cells under certain conditions [84]. PFPnDs should be optimized for smaller diameters to improve extravasation of PFPnDs across the BBB when safe (i.e., without RBC extravasation) laser-activated PFHnD BBB opening is performed. In addition, improved loading of 760 nm PFPnDs with an increased concentration of 760 dye could improve longitudinal image contrast. Similar to the laser-activated PFHnDs used for BBB opening, PA sensitive dye is released when PFPnDs are vaporized, thus allowing the optically triggered dye to remain available for imaging after nanodroplet phase change. The 760 nm optically triggered dye could then be used for PA imaging contrast once the vaporized PFP gas bubble has diffused and is no longer detectable as US imaging contrast. As a result, 760 nm PFPnDs provide advantages for short term (hours) *in vivo* US/PA imaging of extravascular contrast and have the potential to be optimized for longitudinal imaging purposes.

CHAPTER 5. DELIVERY OF PHOTOACOUSTIC CONTRAST VIA LASER-ACTIVATED PERFLUOROCARBON NANODROPLET INDUCED BLOOD BRAIN BARRIER OPENING FOR *IN VIVO* IMAGING OF THE BRAIN

5.1 Introduction

Ultrasound (US) and photoacoustic (PA) imaging of the brain has made progress in recent years, however, both modalities still have limitations. US imaging has limitations with respect to the acoustic impedance mismatch between the ultrasound transducer and skull as well as due to the attenuation of ultrasound signal from the skull to the brain tissue [32]. In many cases, partial removal of the skull is required to achieve adequate US imaging [43]. PA neuroimaging has been able to overcome some of the limitations it shares with US imaging due to the photoacoustic effect and therefore the use of light to interrogate the brain [45, 46]. Unfortunately, a drawback of PA imaging is its limited depth penetration due to optical absorption and scattering of the tissue. Thus, achievements in PA neuroimaging are currently limited to the pre-clinical space [58-62].

In pre-clinical imaging, combined US/PA imaging has the potential to be a resourceful neuroimaging tool. US/PA imaging is cost-effective, efficient, portable, and capable of noninvasive, whole brain imaging unlike other optically based imaging techniques [47, 67, 68]. As a result, US/PA imaging has the potential to monitor development of neurological diseases and disorders through functional molecular imaging of US/PA imaging contrast.

As US/PA imaging contrast agents, laser-activated perfluorocarbon nanodroplets (PFCnDs) provide dual contrast, making them advantageous over only PA or US contrast agents. For neuroimaging, where both US and PA imaging face challenges, laser-activated PFCnDs present themselves as a contrast agent resolvable by information provided by both imaging modalities. Incorporating laser-activated PFCnDs with bulk boiling points near or above physiological temperature, such as perfluoropentane (PFP) and perfluorohexane (PFH), enables uncomplicated US/PA signal analysis to easily localize PFCnD signal within the imaged target [30, 74, 82, 85, 91]. In particular, laser-activated PFPnDs can be monitored via their US and PA signals over short periods of time to distinguish their phase change event from liquid nanodroplet to stable gas bubble from the background [30, 82]. Laser-activated PFHnDs produce PA signal but are more characteristically defined by their repeated phase change behavior which results in a distinct ultrasound signal that enables super-resolution imaging [74, 85, 90, 91]. In addition, lipid shelled PFCnDs are biocompatible and can be functionalized with targeting moieties [82]. Consequently, PFCnDs present themselves as an attractive US/PA imaging tool in pre-clinical neuroimaging.

Recently, a multiplexed system consisting of color-coded laser-activated perfluoropentane nanodroplets for US/PA imaging was developed [82]. PFPnDs were labled with different photoabsorbers of narrow bandwidth optical absorption spectra. This labeling allowed for subpopulations of PFPnDs to be tuned to specific laser wavelengths and therefore selectively phase changed. By employing the optical properties of the PFPnD subpopulations along with the algorithms developed to localize the PFPnDs based on their dynamic US/PA imaging signals, PFPnD subpopulations could be distinguished from one

another. Thus, this multiplexed system can be incorporated in a variety of applications through the functionalization of PFCnDs to target specific biomarkers of interest.

The studies described in this chapter focus on *in vivo* US/PA neuroimaging. Delivery of the laser-activated PFHnD optical trigger, IR-1048 dye, is imaged at 1064 nm at various time points to monitor extravasation over time. In addition, utilizing the core characteristics of the previous multiplexed US/PA imaging studies, PFCnDs are incorporated in a multi-stage opening and delivery system. This demonstration is performed first by opening the BBB using laser-activated PFHnDs optically triggered at 1064 nm (1064 nm PFHnDs) followed by an injection of PFPnDs optically triggered at 760 nm (760 nm PFPnDs). PFPnDs for US/PA imaging can then be triggered at a given time point to allow for localization of PFPnD signal within the brain.

5.2 Materials and methods

5.2.1 Synthesis and characterization of perfluorocarbon nanodroplets (PFCnDs)

IR-1048 PFHnDs (1064 nm PFHnDs) were synthesized as described previously in section 3.2.1. Synthesis of 760 nm PFPnDs was described in section 4.2.2. To characterize both nanodroplets, size and zeta potential were measured in PBS (pH 7.4) using a dynamic light scattering instrument (Zetasizer Nano ZS, Malvern Instruments Ltd.). A spectrophotometer (Evolution 220, Thermo Scientific) was used to measure the absorbance of the PFCnDs. To generate the absorbance spectrum of 1064 nm PFHnDs, a spectrophotometer was used to measure 1064 nm PFHnDs and blank PFHnDs, i.e., PFHnDs synthesized as described above without dye. The blank PFHnD spectrum was then

subtracted from the 1064 nm PFHnD spectrum. The same procedure was performed to generate the absorbance spectrum of 760 nm PFPnDs.

5.2.2 Laser-activated PFHnD induced blood brain barrier opening

All animal studies were conducted under the protocol approved by the Institutional Animal Care and Use Committee at Georgia Institute of Technology. Animal studies were performed as described previously [84, 112]. Briefly, an injection of sustained released buprenorphine (IP, 0.8 mg/kg) was administered to each animal (Balb/c mouse, Jax) prior to anesthesia. Mice were anesthetized using a combination of isoflurane (2%, Henry Schein) and medical air (0.6 L/min, Airgas). Mice were positioned in a stereotax in the prone position on a heating pad (Stoelting Co). Hair from the scalp was removed through shaving and depilatory cream. Proparacaine (0.5%, Henry Schein) was applied to the eyes, and a retro-orbital injection of 50 µL of 3% w/v sterile filtered Evans Blue (EB) (Sigma Aldrich) was administered with a co-injection of 70 µL of IR-1048 PFHnDs (~10^8 droplets). To allow for irradiation of the right side of the brain, animals were positioned underneath an unfocused 1.5 mm core diameter optical fiber (0.39 NA, Thorlabs, Inc.). Irradiation was performed with a Vibrant laser (10 Hz, 5-7 ns pulse length, Opotek Inc.) at a wavelength of 1064 nm (Figure 2). Animals (n = 5) were irradiated at a laser fluence of 38 mJ/cm² for 600 pulses (t = 60 seconds) as to prevent laser irradiation damage [112].

5.2.3 In vivo imaging of extravasated 1064 nm dye

In vivo imaging was performed twice, immediately after the blood brain barrier (BBB) opening procedure and four hours after, prior to animal euthanasia (Figure 21).

Animals were imaged using a photoacoustic and ultrasound imaging system (Vevo LAZR, FUJIFILM VisualSonics Inc., Figure 23) with a 21 MHz ultrasound and photoacoustic imaging probe (LZ-250, FUJIFILM VisualSonics Inc.). The system's tunable Nd:YAG laser (20 Hz, 5-7 ns pulse length) was operated at a wavelength of 1064 nm and a laser fluence of 24 mJ/cm². Imaging was performed at a US/PA frame rate of 5 frames per second. Coronal 3D US/PA images were collected with a distance step size of 0.102 mm for a total of about 13 mm for both US/PA imaging time points.

After the first *in vivo* imaging session, mice were allowed to recover, with no gross behavioral damage observed. After four hours, mice were imaged again followed by animal euthanasia via an IP Euthatal injection (150 mg/kg) and perfusion with 1X PBS (pH 6.8) and 4% paraformaldehyde (PFA). Heads were removed and post-fixed overnight in 4% PFA solution. After 24 hours, brains were excised, and *ex vivo* US/PA imaging was performed.

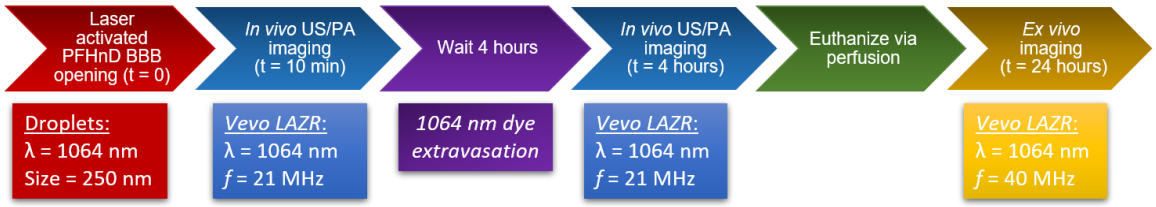

Figure 21. Timeline of laser-activated PFHnD induced BBB opening and *in vivo* and *ex vivo* imaging sessions.

5.2.4 In vivo imaging of 760 nm perfluoropentane nanodroplets

Immediately after the laser-activated PFHnD induced BBB opening, mice under anesthesia were taken out of the stereotax and placed in the supine position (Figure 22). A

jugular injection of 75 µL 760 nm PFPnDs was administered and mice were allowed to recover, with no gross behavioral damage observed. After four hours, animals were anesthetized and imaged using using a photoacoustic and ultrasound imaging system (Vevo LAZR, FUJIFILM VisualSonics Inc., Figure 23) with a 21 MHz ultrasound and photoacoustic imaging probe (LZ-250, FUJIFILM VisualSonics Inc.) and a custom built fiber jacket used to increase the US/PA system's laser focus depth from 9-11 mm to 11-13 mm. The system's tunable ND:YAG laser (20 Hz, 5-7 ns pulse length) was operated at two wavelengths. Animals were first imaged at 760 nm at a laser fluence of 22 mJ/cm² followed by imaging at 1064 nm and a laser fluence of 24 mJ/cm². Imaging was performed at a US/PA frame rate of 5 frames per second. Coronal 3D US/PA images at each wavelength were collected with a distance step size of 0.102 mm for a total of about 13 mm.

After *in vivo* imaging, animals were euthanized via an IP Euthatal injection (150 mg/kg) followed by perfusion with 1X PBS (pH 6.8) and 4% paraformaldehyde (PFA). Heads were removed and post-fixed overnight in 4% PFA solution. After 24 hours, brains were excised, and *ex vivo* US/PA imaging was performed.

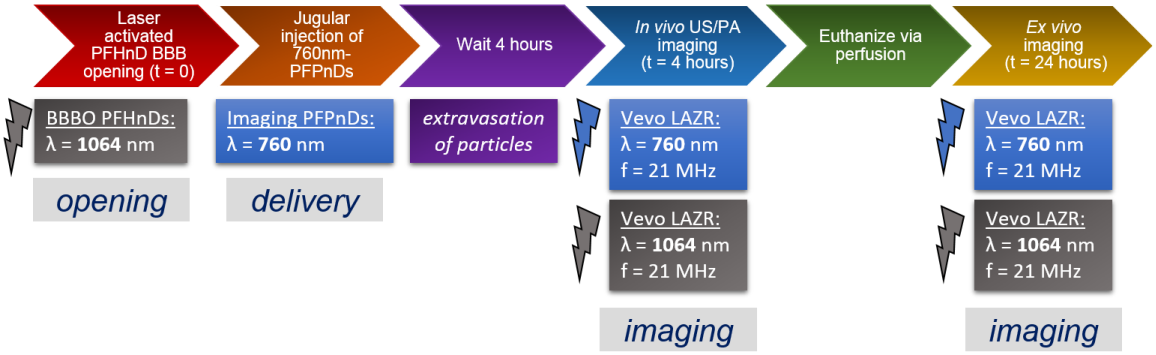

Figure 22. Timeline of laser-activated PFHnD induced BBB opening and injection of 760 nm PFPnDs, followed by *in vivo* and *ex vivo* imaging.

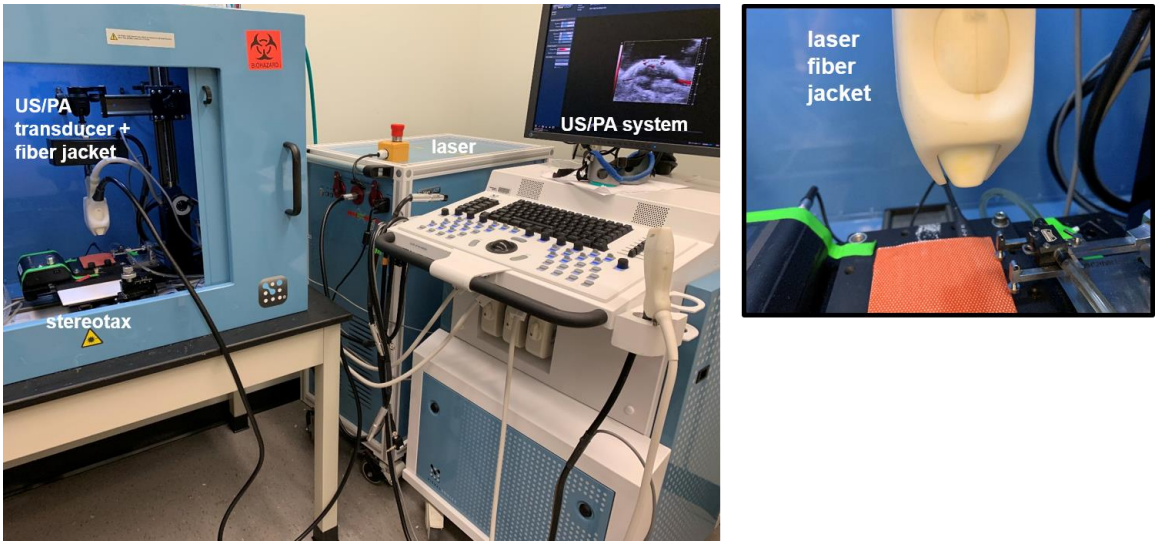

Figure 23. *In vivo* imaging setup for brain imaging. For studies mentioned in section 5.2.3, *in vivo* imaging was performed without the laser fiber jacket as shown in the zoomed-in view of the transducer to the right. Studies conducted as described in section 5.2.4 utilize the fiber jacket as shown.

5.2.5 Ex vivo ultrasound and photoacoustic imaging

Brains, excised and fixed, were placed on top of an 8% gelatin base in a container filled with degassed water. Samples were imaged using an ultrasound and photoacoustic imaging system (Vevo LAZR, FUJIFILM VisualSonics Inc.) with a 40 MHz ultrasound

and photoacoustic imaging probe (LZ-550, FUJIFILM VisualSonics Inc.). The US/PA imaging system's tunable Nd:YAG laser (20 Hz, 5-7 ns pulse length) was operated at two wavelengths. Brains were imaged at 760 nm at a laser fluence of 22 mJ/cm² and at 1064 nm at a laser fluence of 24 mJ/cm². Imaging was performed at a US/PA frame rate of 5 frames per second. Coronal 3D US/PA images at each wavelength were collected with a distance step size of 0.102 mm for a total of about 14 mm.

5.2.6 US/PA image processing

Coronal ultrasound and photoacoustic image sets were processed in MATLAB (Mathworks, Inc.). US/PA images were thresholded to reduce noise. US/PA image sets were also exported to generate 3D whole brain images using AMIRA (Thermo Scientific). For *ex vivo* images, transverse view and corner cut images of the treated (right) side of the brain, viewed from behind the cerebellum, were captured using AMIRA. *In vivo* images were also captured using AMIRA, with corner cut views of the treated (right) side of the brain shown.

Image processing of 760 nm PFPnDs employed an algorithm previously described [30, 82]. Briefly, pixel-wise linear regression was performed on the ultrasound data sets captured in one 2D image plane of the brain over time. In the case of ultrasound-based analysis, pixels that had an increase in ultrasound signal amplitude over time corresponded to PFPnDs that were phase transitioning from liquid nanodroplets to gas microbubbles. Pixels with ultrasound signal amplitude increase rates above a certain threshold were identified, and a map of the above-threshold pixel rates was displayed over a co-registered ultrasound image, highlighting the location of PFPnDs within the image. All pixels

identified as vaporizing PFPnDs outside of the brain were rejected. From this method, US signal from PFPnDs within the brain can be localized.

5.3 Results

5.3.1 Characterization of perfluorocarbon nanodroplets

Both PFCnD types, 760 nm PFPnDs and 1064 nm PFHnDs, were characterized by absorbance, size, and zeta potential (Figure 24). The absorbance of 760 nm PFPnDs was near 760 nm and the absorbance of 1064 nm PFPnDs was near 1064 nm (Figure 24A). These absorbance peaks correspond to absorption spectra of the optically absorbing dyes used in the synthesis of the PFCnDs, Epolight 9151 for 760 nm PFPnDs and IR-1048 for 1064 nm PFHnDs (Figure 16A). In terms of size, 760 nm PFPnDs had a peak diameter of 342 nm while 1064 nm PFHnDs had a peak diameter of 255 nm (Figure 24B). Zeta potential distributions of both PFCnDs were similar, with 760 nm PFPnDs having zeta potential peak of -10.3 mV and 1064 nm PFHnDs having a peak zeta potential of -1.98 mV.

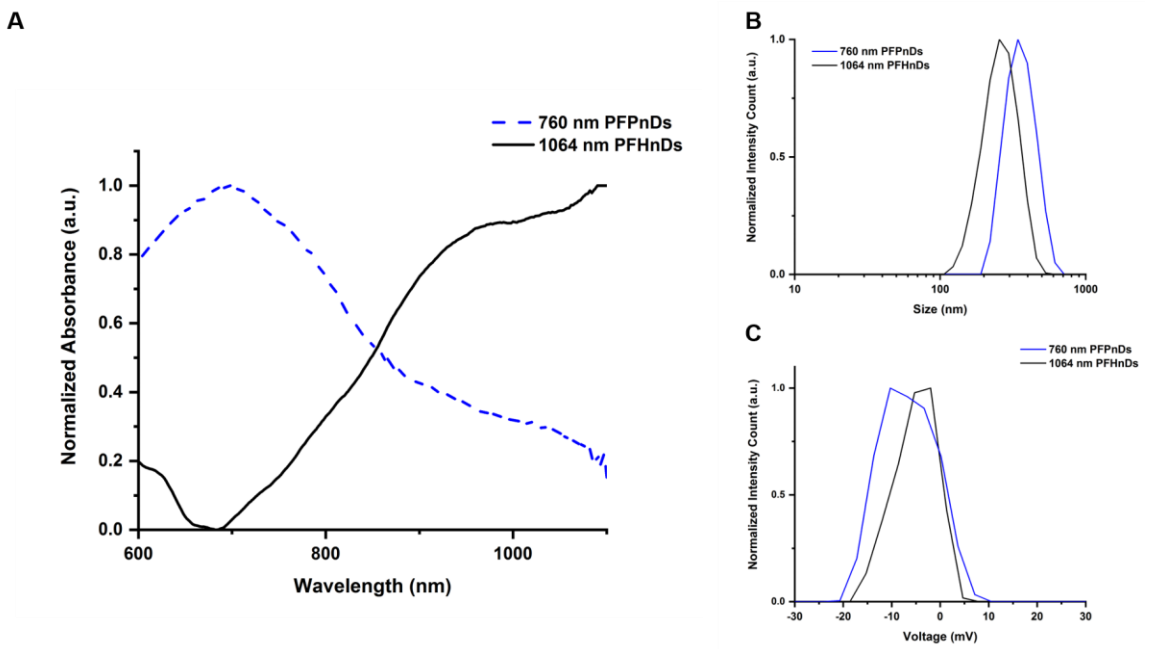

Figure 24. Characterization of perfluorocarbon nanodroplets used for *in vivo* imaging. (A) Absorbance spectra for 760 nm perfluoropentane nanodroplets (PFPnDs) and for 1064 nm perfluorohexane nanodroplets (PFHnDs). (B) Size distribution of 760 nm PFPnDs and 1064 nm PFHnDs. (C) Zeta potential of 760 nm PFPnDs and 1064 nm PFHnDs.

5.3.2 Ultrasound and photoacoustic imaging of extravasated IR-1048 dye

For animals who only received optimized laser-activated PFHnD BBB opening, *in vivo* US/PA imaging was conducted (Figure 25). US/PA imaging at 1064 nm and conducted at t = 10 min showed little to no PA signal, denoted by the hot colormap overlaid on the US image, within the brain (Figure 25A). PA signal is visible near the skin and skull interface due to scattering of the laser light with the skin which can produce PA signal [133]. At t = 4 hours, PA signal within the brain is visible on the treated (right) side of the brain (Figure 25B) in addition to scattered signal from the skin. Further, *ex vivo* imaging of the fixed, excised brain also shows PA signal concentrated on the treated (right) side of the brain (Figure 25C).

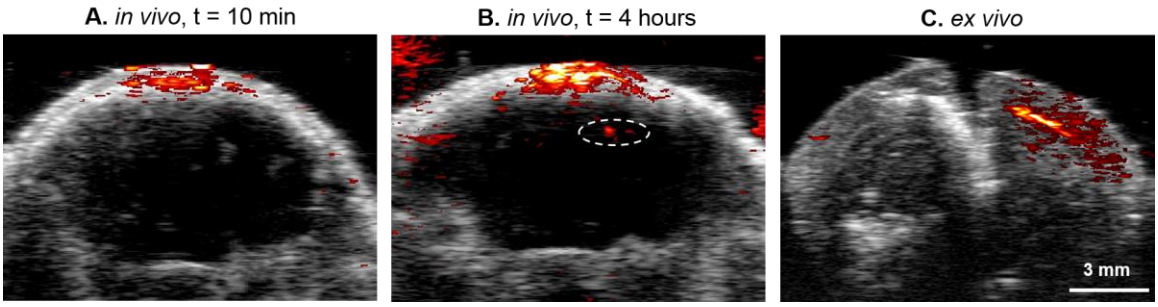

Figure 25. Coronal 2D US/PA imaging at 1064 nm. (A) *In vivo* US/PA imaging at t = 10 min. (B) *In vivo* US/PA imaging at t = 4 hours, showing localized 1064 nm PA signal within the dotted white circle on the treated (right) side of the brain. (C) *Ex vivo* imaging of the fixed, excised brain at 1064 nm, showing PA signal on the treated (right) side of the brain.

Both *in vivo* and *ex vivo* US/PA images were reconstructed using 3D visualization software (AMIRA) to examine the extent of PA signal within the brain. *In vivo* 3D US/PA images agree with the 2D coronal images (Figure 25) in regards to the amount of dye delivered in the treated (right) side of the brain at the two different time points (Figure 26). US/PA imaging at t = 10 min shows minimal PA signal within the brain while at t = 4 hours an increase in PA signal volume is visible. Reconstructed *ex vivo* images also display the localized PA signal at 1064 nm on the treated (right) side of the brain which can be seen in the transverse and corner cut views of the *ex vivo* US/PA images (Figure 26).

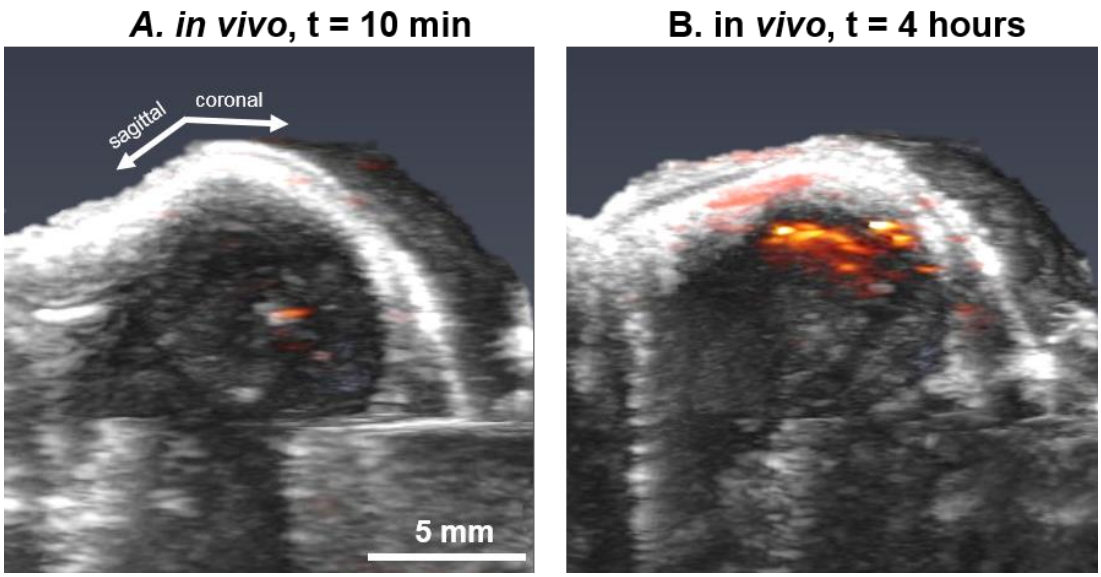

Figure 26. Reconstructed *in vivo* 3D US/PA images at 1064 nm. Corner cut views of the treated (right) side of the brain are shown. (A) Reconstructed 3D US/PA image at t = 10 min. (B) Reconstructed 3D US/PA image at t = 4 hours.

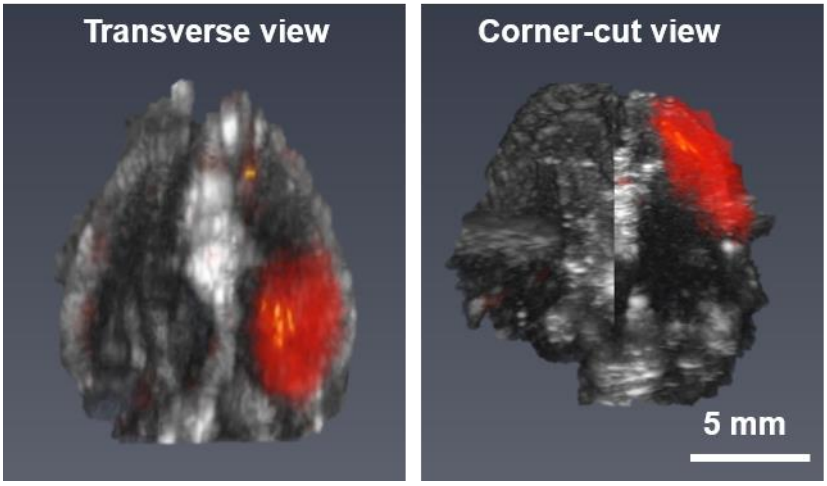

Figure 27. Reconstructed *ex vivo* 3D US/PA images at 1064 nm. Image views include the transverse view and the corner cut view of the treated (right) side of the brain shown.

Ex vivo imaging for animals who received optimized laser-activated PFHnD BBB opening were imaged at two wavelengths, 1064 nm and 760 nm, to examine the PA intensity of 1064 nm extravasated dye at 760 nm (Figure 28). PA signal intensity of 1064

nm dye needs to be considered when other PA contrast agents, such as those described in section 5.2.4, are to be delivered to the tissue. If the PA contribution of the 1064 nm dye delivered is too high, then it could prevent accurate localization of PA signal from the second contrast agent delivered without using methods such as PA spectroscopic analysis. Evaluating the signal of 1064 nm dye at 760 nm shows PA signal is present when the brain is imaged at 760 nm. However, in comparison to the average PA signal intensity at 1064 nm and over the same region of interest, the PA signal intensity and spread is less at 760 nm than at 1064 nm.

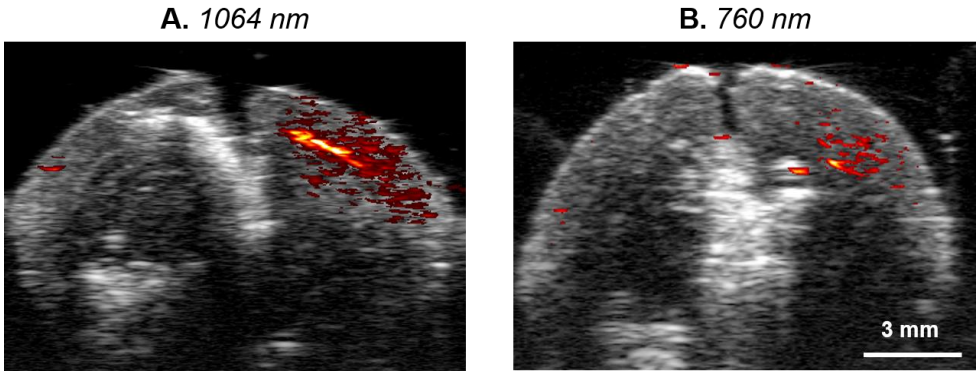

Figure 28. *Ex vivo* imaging at two wavelengths, 760 nm and 1064 nm. (A) *Ex vivo* imaging at 1064 nm. (B) *Ex vivo* imaging at 760 nm.

5.3.3 Ultrasound and photoacoustic imaging of delivered 760 nm perfluoropentane nanodroplets

For animals where 760 nm PFPnDs were delivered via jugular injection after the BBB opening procedure was performed, *in vivo* US/PA imaging was only performed at t = 4 hours. PFPnDs are single phase change nanoparticles and therefore the dynamic US/PA imaging properties of a delivered set of PFPnDs can only be captured in one US/PA imaging session [75]. The results of the US/PA imaging and US signal processing of the

laser-activated 760 nm PFPnDs shows localization of 760 nm PFPnDs within the brain (Figure 29), in the region where echogenic contrast and US/PA signal are present below the skin and skull. US/PA imaging at both 760 nm and 1064 nm shows scattered PA signal from the laser interaction with the skin, while US/PA imaging at both wavelengths also shows an image artifact caused by the metal stereotax ear bars [134].

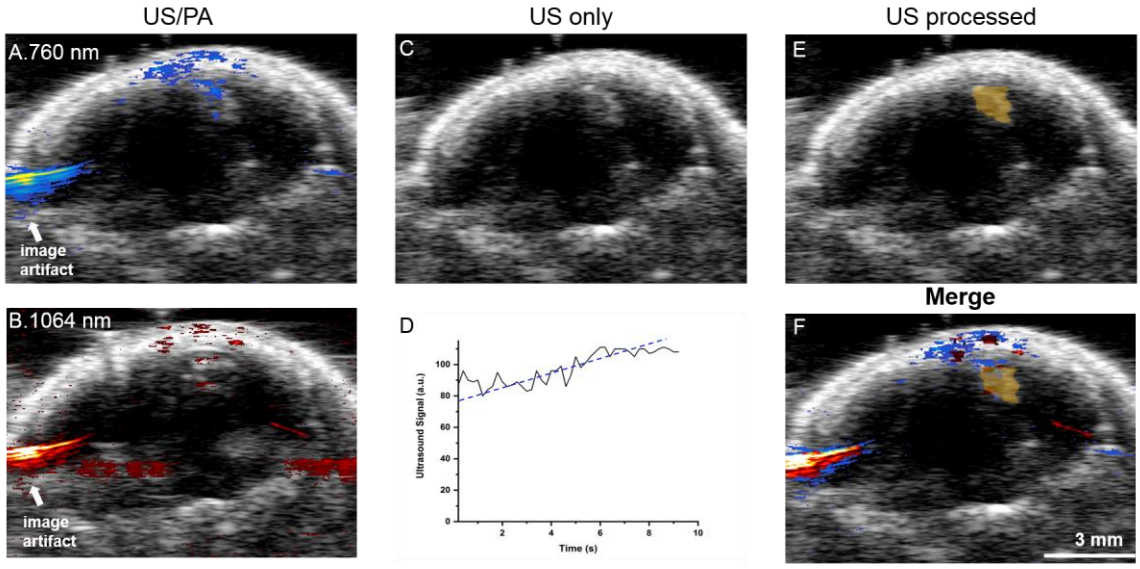

Figure 29. *In vivo* 2D US/PA imaging showing the localization of PFPnD signal within the brain. (A) US/PA imaging at 760 nm showing localized PA signal, designated by the blue overlay, near the echogenic region inside the brain. (B) US/PA imaging at 1064 nm showing localized PA signal, designated by the red overlay, near the echogenic region inside the brain. (C) US imaging of the brain highlighting the echogenic region on the treated (right) side of the brain. (D) Plot of the US signal as frame number (i.e., time) increases over the echogenic region in (C) showing an increase in US signal amplitude over time. (E) US processed image using the algorithm mentioned in section 5.2.6, overlaying PFPnD pixels in yellow with the US image. (F) Merge of the US/PA signal at 760 nm (blue), US/PA signal at 1064 nm (red), and US processed signal (yellow).

Reconstructed 3D US/PA images of PA imaging at 760 nm, 1064 nm, and US signal processing were also generated (Figure 30). In the reconstructed images, PA signal at 760 nm and 1064 nm and the US signal processed for laser-activated 760 nm PFPnD behavior localizes the volume of 760 nm PFPnDs within the brain. In the reconstructed 3D US/PA images, scattered PA signal at 760 nm and 1064 nm is present, however, PA signal

at both wavelengths is also visible within the volume designated by the US processed 760 nm PFPnD signal (highlighted in yellow).

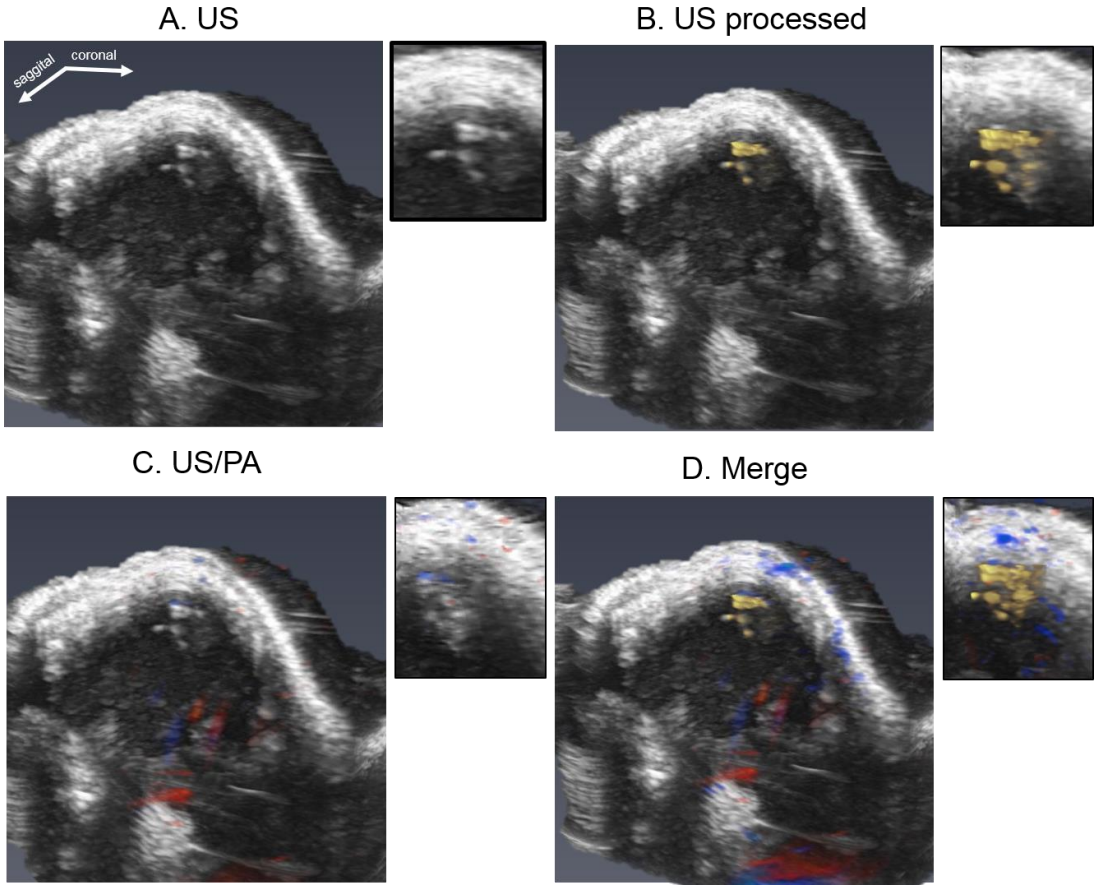

Figure 30. Reconstructed *in vivo* 3D US/PA images showing the localization of PFPnD signal within the brain. Corner cut views of the treated (right) side of the brain are shown. The zoomed-in image to the right of each whole brain image highlights the 3D reconstructed region of interest within the brain. (A) US image of the brain highlighting the echogenic region on the treated (right) side of the brain. (B) US processed image using the algorithm mentioned in section 5.2.6, overlaying PFPnD pixels in yellow with the US image. (C) US/PA imaging at 760 nm (blue overlay) and 1064 nm (red overlay) showing localized PA signal, near the echogenic region inside the brain. (D) Merge of the US/PA signal at 760 nm (blue), US/PA signal at 1064 nm (red), and US processed signal (yellow).

Ex vivo images were also reconstructed at both PA imaging wavelengths (Figure 31). Transverse and corner cut view images of the treated (right) side of the brain show the overlap between PA signal at 760 nm and 1064 nm.

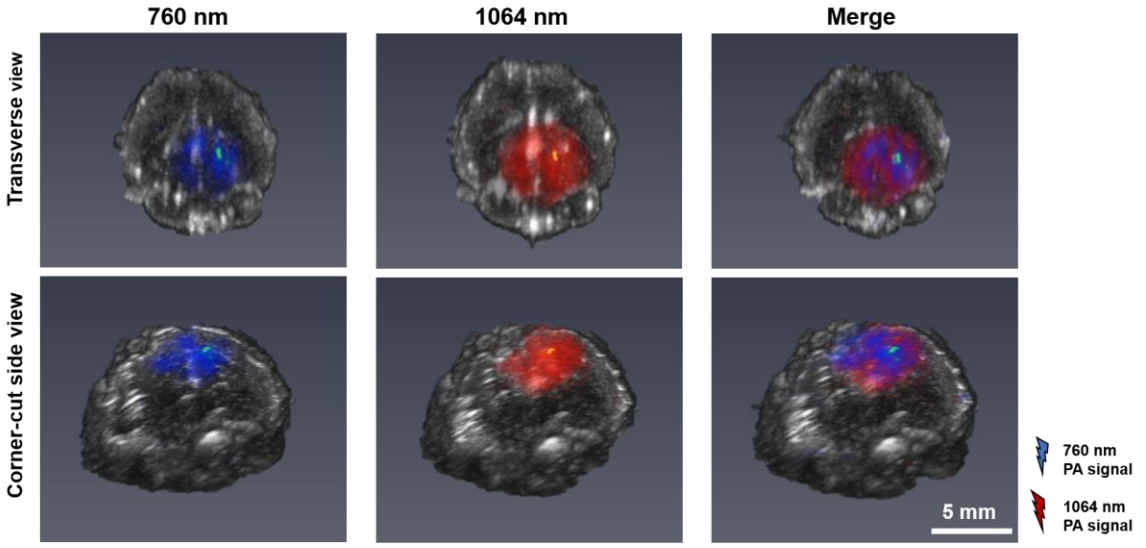

Figure 31. Reconstructed *ex vivo* 3D US/PA images at 760 nm (blue), 1064 nm (red), and merge of PA signal captured at both wavelengths. Image views include the transverse view and the corner cut view of the treated (right) side of the brain shown.

5.4 Discussion

The imaging studies performed show how laser-activated PFHnD induced BBB opening enables delivery of US/PA contrast to the tissue. Further, US/PA contrast is delivered in sufficient quantities to allow for *in vivo* neuroimaging. *In vivo* imaging at 1064 nm and t = 4 hours shows PA contrast from IR-1048 dye localized within the treated (right) side of the brain (Figure 25). In addition, the difference in PA imaging contrast from t = 10 min to t = 4 hours on the treated side of the brain demonstrates how PA signal can change over time based on extravasation of PA contrast into the tissue. *Ex vivo* imaging at 1064 nm confirms the delivery of 1064 nm dye to the tissue. US/PA signals are also reconstructed to 3D volumes to give a volumetric representation of the delivered PA signal (Figure 26, Figure 27). Further, when comparing *ex vivo* imaging at 1064 nm and 760 nm, it can be seen that PA signal intensity is less at 760 nm (Figure 28). This trend corresponds

to the IR-1048 dye having reduced optical absorption at 760 nm. As a result, if other PA absorbers are delivered to the tissue, such as 760 nm PFPnDs, PA signal at 760 nm should result primarily from the 760 nm PFPnDs. In addition, the PA signal intensity trend of IR-1048 is expected to correspond with the absorbance spectrum of IR-1048 dye. Although these studies only evaluate IR-1048 dye at two wavelengths, future studies could include spectroscopic PA analysis. *In vivo* and *ex vivo* US/PA imaging could include spectral unmixing analysis to distinguish multiple photoabsorbers, endogenous and exogenous, found in the tissue [81].

For delivery and imaging of 760 nm PFPnDs, PA signal at 760 nm and 1064 nm is evident; however, in these studies, PFPnDs are distinctly characterized by their US image contrast. Algorithms developed to track the US signal of the 760 nm PFPnDs over time allows for localization of PFPnD signal (Figure 29). Reconstructed *in vivo* 3D US/PA images also show the overlap in PA signal with US PFPnD signal (Figure 30), and 3D US/PA images reconstructed after *ex vivo* imaging show the volumetric footprint of PA signal delivered to the tissue at 1064 nm and 760 nm (Figure 31).

Laser-activated PFHnD induced BBB opening and *in vivo* US/PA imaging combined is a useful tool for neuroimaging. US/PA imaging after laser-activated PFHnD induced BBB opening enables monitoring of BBB opening and extravasation. Although only two time points were used in the imaging sessions described above, BBB opening could be monitored over multiple time points, providing insight about the characteristic nature of laser-activated PFHnD induced BBB opening. Much like magnetic resonance (MR) guided focused ultrasound, the rate of opening can be examined using *in vivo* US/PA imaging as well as characteristics regarding BBB closing such as time of closing and rate

of closing [5]. Overall, US/PA *in vivo* imaging can be used to augment and improve the current methods used for laser-activated PFHnD induced BBB opening.

Furthermore, *in vivo* US/PA imaging after delivery of additional contrast agents to the brain after laser-activated PFHnD induced BBB opening demonstrates the utility of US/PA imaging in neuroimaging. As laser-activated PFPnDs produce a single phase change event, they were allowed to circulate for four hours before US/PA imaging was conducted. As seen with *in vivo* imaging of the 760 nm PFPnDs, droplets were localized to the treated side of the brain, producing both US and PA contrast at a laser irradiation wavelength of 760 nm. This US and PA signal was also co-registered with the PA signal at 1064 nm, the peak wavelength of the optically triggered dye within the laser-activated PFHnD used for BBB opening. Although these imaging studies did not demonstrate distinctive spatial differences in signal for 760 nm PFPnDs and 1064 nm PFHnDs, they did demonstrate the ability to image the subpopulations of PA and US image contrast. To further resolve the location of droplets within the brain, histological staining can be performed. Specifically, laser-activated PFCnDs can be fluorescently tagged to determine their location within the tissue, providing insight regarding the ability of droplets to extravasate [82]. Thus, the use of multiplexed PFCnDs within neuroimaging has the ability to provide spatial information regarding US/PA image contrast over longer periods of time.

In addition, there appears to be multiple benefits of laser-activated PFCnDs as a US/PA neuroimaging contrast agent. Although other PA contrast agents can be used, PFCnDs have advantages regarding their dual US/PA contrast. As seen in section 4.3, 760 nm PFPnDs showed distinct US/PA contrast that produced a higher US and PA signal in comparison to CuS NPS. The 760 nm PFPnDs were also incubated at a lower concentration

than CuS NPs, which suggests better contrast can be obtained using 760 nm PFPnDs and at a lower dose. In addition, PFCnDs can be synthesized for biocompatibility and can contain already approved FDA components, expediting their translation to clinical applications in comparison to constructs made without FDA compliant materials. Targeting moieties are easily attachable to PFCnDs, making further steps toward molecular *in vivo* neuroimaging possible with laser-activated PFCnDs.

Finally, as seen with the laser-activated PFHnDs used for BBB opening, a subpopulation of PFCnDs delivered for *in vivo* US/PA imaging can also be used for therapy. By relying on the phase change mechanisms and resulting cavitation-like behavior produced by laser-activated PFCnDs, a subpopulation of droplets could be used to destroy tumor cells or improve uptake of viral vectors for gene transfection [70, 71]. Additionally, extravasated PFCnDs can be used to carry therapeutics to the brain tissue for localized delivery, with delivery confirmation via US/PA imaging of therapeutic PFCnDs [70]. Therefore, PFCnDs present themselves not only as a promising contrast agent for US/PA neuroimaging but also as a multi-facetted therapeutic vehicle.

CHAPTER 6. CONCLUSIONS AND FUTURE WORK

6.1 Laser-activated PFCnDs for BBB opening

6.1.1 Conclusions

In this work, blood brain barrier opening induced by laser-activated perfluorocarbon nanodroplets (PFCnDs) was evaluated on both the macroscopic and microscopic scales. Through evaluation of the technique via qualitative measurements of Evans Blue extravasation, histology, and ultrasound and photoacoustic (US/PA) imaging, it was demonstrated that laser-activated perfluorohexane nanodroplets (PFHnDs) can be used to open the blood brain barrier (BBB) and allow for various sized constructs, including antibodies, dyes, and red blood cells, to extravasate. Further, laser parameters, such as laser fluence and number of laser pulses used, involved in laser-activated PFHnD induced BBB opening were optimized for safety and efficacy. Using a quantitative analysis of fluorescence area produced from immunoglobulin (IgG) extravasation and volumetric PA signal from PA dye extravasation, trends in BBB opening were determined. Overall, laser-activated PFCnDs were shown to successfully open the BBB, and opening can be tuned through adjustment of laser parameters used.

6.1.2 Improving laser-activated PFCnD BBB opening

Although these studies show the effectiveness of laser-activated PFHnD induced BBB opening, there is also opportunity to further optimize PFCnDs as a mechanical agent. In particular, laser-activated PFCnD parameters should also be explored. Parameters such as PFCnD size, concentration, perfluorocarbon core, and encapsulated optical trigger are

worth examining to determine the optimal setup for laser-activated PFCnD induced BBB opening.

Furthermore, laser-activated PFCnD induced BBB opening should be compared to acoustically activated PFCnD induced BBB opening with focused ultrasound. Direct evaluation of the two different energy sources for PFCnD phase change allows for a clearer understanding of the advantages and disadvantages of focused ultrasound (FUS) and laser light in the process of BBB opening using PFCnDs. In particular, laser-activated PFCnD induced BBB opening will experience limitations in comparison to FUS with respect to depth penetration. Laser depth penetration is limited due to the scattering and absorption of light in tissue [57]. The laser energy used in these experiments obeys Beer's Law, which states that the energy deposited decays exponentially with distance. Using wavelengths at the far end of the near-infrared spectrum, such as 1064 nm, can increase this depth penetration to ~1 cm [57]. However, if a deeper opening depth is desired, laser-activated PFCnDs will fall short in efficacy. In the case of PFCnD induced BBB opening at greater depths, FUS induced BBB opening has been demonstrated [96]. Therefore, a main advantage of BBB opening by FUS vaporized PFCnDs is its ability to create a focal opening in the BBB at depths greater than that of laser-activated droplets. However, this FUS PFCnD activation often requires high ultrasonic pressures, which can cause damage to the tissue [73, 96]. Thus, FUS PFCnD induced BBB opening also has limitations.

To overcome these challenges, it is hypothesized that a FUS field simultaneously triggered with a laser pulse will enable PFCnD activation and allow opening to occur locally in the FUS field. PFCnDs circulating will be sensitive to both the FUS field and laser energy, enabling vaporization at lower laser energies and at increased depths while

maintaining lower and safer ultrasound pressures. Combined phase change of PFCnDs with laser light and FUS energy has been demonstrated previously for imaging purposes and is described as sono-photoacoustic activation [135, 136]. In sono-photoacoustic activation, laser irradiation is synchronized with the peak rarefractional phase of the acoustic pulse to enable phase change at significantly lower thresholds [135, 136]. As result, this dual energy activation can be translated to BBB opening, allowing for a reduction in the intensity of energies used to phase change PFCnDs and initiate BBB opening.

6.1.3 Examining physiological response caused by BBB opening

As laser-activated PFCnDs are an exogeneous agent, the immune response of the body to PFCnDs should be examined. Although damage to the tissue can be assessed using histological stains such as hematoxylin and eosin, further investigation into changes in morphology and behavior of different cells within the brain is warranted. For example, immunohistochemical staining of ionized calcium-binding adapter molecule 1 (IBA1) can provide information regarding microglial activation. Because microglia play a key role in the immune response within the brain, changes to their behavior after BBB opening are important to examine [126, 132]. Preliminary studies of IBA1 staining show that for unoptimized laser-activated PFHnD induced BBB opening, there appears to be a difference in microglial activation on the treated side of the brain in comparison to a control where no laser-activated PFHnD induced BBB opening occurred (t = 4 hours post BBB opening, Figure 32).

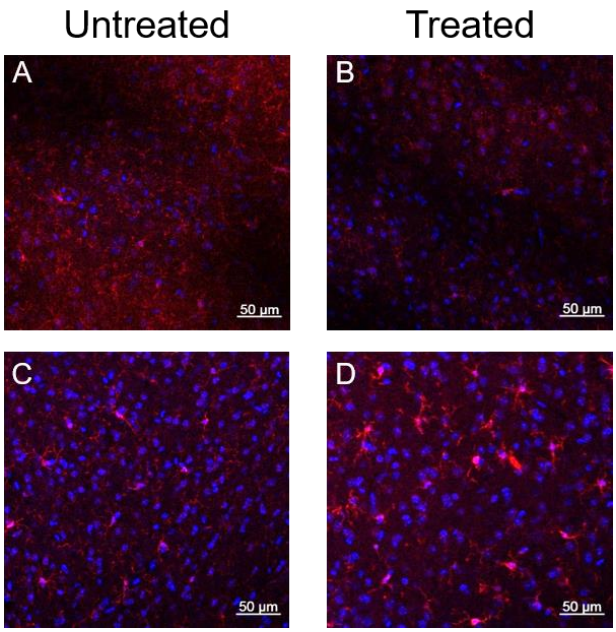

Figure 32. Immunohistochemical staining for IBA1 (red), a microglial marker, and DAPI (blue). Control pictomicrographs (A-B), where no BBB opening occurred, show no microglial activation on either the left (untreated) or right (treated) side of the brain. However, when laser-activated BBB opening occurs, microglial activation is visible on the right (treated) side of the brain (C-D).

Furthermore, the effects of laser-activated PFCnD induced BBB opening should be studied for time points of longer than t = 4 hours, the time point of euthanasia for the *in vivo* studies described. After performing laser-activated PFCnD induced BBB opening, animals should be evaluated over time points of days or weeks. These longer time points will not only allow for further evaluation of microglia but also other cells within the brain such as astrocytes or neurons. As seen with studies with microbubble assisted FUS BBB opening, an acute inflammatory response occurs at certain microbubble doses and acoustic pressures used [137]. Therefore, it is likely laser-activated PFCnD induced BBB opening will have a similar immune response.

Not only is immune response important for understanding for laser-activated PFCnD induced BBB opening, but the characteristic nature of the BBB opening is also important to examine. Specifically, the rates of BBB opening and closing are important parameters to determine the treatment window available using laser-activated PFHnDs. For microbubble assisted FUS, the time window ranges from 4 to 24 hours [5, 102]. Although the laser-activated PFCnD induced BBB opening is expected to follow this trend, it is important to experimentally validate this behavior.

6.1.4 Laser-activated PFCnDs to open other biological barriers

In addition to the blood brain barrier, it seems promising to utilize laser-activated PFCnDs in opening other biological barriers. Specifically, laser-activated PFCnDs can be utilized to open the blood spinal cord barrier (BSCB). This other neurological barrier is a major challenge for many diseases and disorders of the CNS. One example includes effective delivery of gene therapy to the spinal cord, which has been a challenge for clinicians and researchers [4]. Gene therapy in the spinal cord has long been a challenge due not only to the BSCB but also to the spinal column. Traditional methods used to treat spinal cord injury or ALS involve removal of the spinal bone and direct injections [4]. Laser-activated PFCnDs induced BSCB opening has the potential to noninvasively and locally deliver viral vectors to the spinal cord for gene therapy. In particular, AAV9 crosses the BBB and BSCB, however, microbubble assisted FUS BSCB opening has shown to enable localized and more concentrated delivery of this virus [4]. Thus, laser-activated PFCnDs can be implemented similarly, with laser light only or combined with FUS, to permeabilize the BSCB and allow for therapeutic treatments.

Laser-activated PFCnDs can also be implemented to create pores in cell membranes similarly to sonoporation, a method that uses microbubbles and FUS to create openings in cell membranes [138]. Laser-activated PFCnDs have been shown to increase uptake of intracellularly specific fluorescent dyes, highlighting the potential for laser-activated PFCnDs in a wide range of treatments including enhanced drug delivery for tumor treatment [138, 139].

6.2 Laser-activated PFCnDs for US/PA neuroimaging

6.2.1 Conclusions

Laser-activated PFCnDs are shown in this work as a useful US/PA imaging contrast agent for neuroimaging. Specifically, laser-activated PFPnDs were used to produce dynamic imaging contrast within the brain. Laser-activated PFPnDs were evaluated for their dynamic, enhanced dual US/PA contrast, producing sufficient US/PA signal up to 24 hours in *in vitro* studies. In addition, the *in vivo* US signal produced by laser-activated PFPnDs was tracked and co-registered with the PA signal produced by the droplets to enable localization of PFPnDs within the brain. Furthermore, laser-activated PFHnDs used for BBB opening were able to deliver PA sensitive dye in sufficient amounts to allow for imaging of extravasation over time. As a result, laser-activated PFCnDs are presented as a promising tool to enhance US/PA neuroimaging.

6.2.2 Improving US/PA neuroimaging methods

Although *in vivo* US/PA imaging methods were able to detect PA contrast within the brain, there are a few areas in which US/PA imaging can be improved. Specifically,

US/PA imaging systems can be improved. The current imaging setup relies on a US/PA imaging system that limits user modification of the imaging sequences and parameters. However, other imaging systems such as a tunable laser source and user-programmable ultrasound imaging setup would allow for more versatile imaging techniques [140]. In addition, hardware for signal amplification could be added to enable improved receive of US and PA signals as they travel across the skull to the US receiver. Not only can hardware changes improve the acquisition capabilities for US/PA neuroimaging, but improved signal processing techniques are also possible. In particular, methods can be developed to reduce artifacts from the scattering at the skin and metal ear bars, allowing for improved visualization of PA signal from within the brain.

Additionally, *in vivo* US/PA imaging can be improved through spectroscopic photoacoustic analysis. In addition to PA signal produced via exogenous contrast, endogenous absorbers, such as oxygenated and deoxygenated hemoglobin, could be considered. Because PA contrast agents have unique optical signatures related to their absorption spectra, they can be separated from any endogenous PA contrast [57]. Through spectroscopic unmixing, separate imaging contrast provided by subpopulations of laser-activated PFCnDs could not only be identified via their dynamic US and PA imaging behavior but also by their optical absorption spectra.

6.2.3 Applications of US/PA neuroimaging

Through the combination of laser-activated PFCnDs induced BBB opening and US/PA imaging of delivered PA contrast agents, the ability to quantitatively and longitudinally measure PA signal in the brain is possible. This capability enables real time

monitoring of brain function and how this may change with a disease state. One specific application of this particular method is for use in Alzheimer's disease. By functionalizing, via antibody conjugation or other targeting moiety, the PA contrast agent, whether that be optimized PFCnDs, CuS NPs, or another PA sensitive contrast agent, can target plaques or tau proteins within the brain allowing the state of Alzheimer's disease to be evaluated *in vivo* [141, 142]. As the disease progresses, PA signal can be monitored longitudinally to see how the distribution of the disease state changes within the tissue [142, 143]. This data is of particular interest as current imaging techniques are unable to capture this information and provide insight into the disease progression on a molecular level in a way US/PA imaging with PA contrast agents can [115, 144]. Not only can PA contrast agents be used to monitor diseased tissue changes, but it also can be used to provide an improved understanding of the clearance system of the brain [143]. Thus, in the area of basic science, PA imaging has the potential to provide more insight into how the normal brain functions. Overall, this technique could enable an improved understanding of neurological function in both normal and diseased brain states.

6.3 Summary of conclusions and future directions

These studies demonstrate the usefulness of laser-activated PFCnDs in neurological applications. Specifically, laser-activated PFHnDs have been shown to open the BBB, allowing for extravasation of various sized constructs. The laser parameters for laser-activated PFHnD induced BBB opening have been optimized to enable safe and efficient opening. Furthermore, laser-activated PFCnDs have been evaluated as a US/PA imaging contrast agent for *in vivo* neuroimaging. Thus, these studies establish laser-activated PFCnDs in neurological imaging and therapy, demonstrating laser-activated PFCnDs as a

versatile tool with the potential to impact treatment and monitoring of neurological diseases.

REFERENCES

1. M. Jucker, "The benefits and limitations of animal models for translational research in neurodegenerative diseases," Nat Med **16**, 1210-1214 (2010).

2. J. O. Rinne, D. J. Brooks, M. N. Rossor, N. C. Fox, R. Bullock, W. E. Klunk, C. A. Mathis, K. Blennow, J. Barakos, A. A. Okello, S. Rodriguez Martinez de Liano, E. Liu, M. Koller, K. M. Gregg, D. Schenk, R. Black, and M. Grundman, "11C-PiB PET assessment of change in fibrillar amyloid-beta load in patients with Alzheimer's disease treated with bapineuzumab: a phase 2, double-blind, placebo-controlled, ascending-dose study," Lancet Neurol **9**, 363-372 (2010).

3. J. Dong, R. Revilla-Sanchez, S. Moss, and P. G. Haydon, "Multiphoton in vivo imaging of amyloid in animal models of Alzheimer's disease," Neuropharmacology **59**, 268-275 (2010).

4. D. Weber-Adrian, E. Thevenot, M. A. O'Reilly, W. Oakden, M. K. Akens, N. Ellens, K. Markham-Coultes, A. Burgess, J. Finkelstein, A. J. Yee, C. M. Whyne, K. D. Foust, B. K. Kaspar, G. J. Stanisz, R. Chopra, K. Hynynen, and I. Aubert, "Gene delivery to the spinal cord using MRI-guided focused ultrasound," Gene Ther **22**, 568-577 (2015).

5. N. Vykhodtseva, N. McDannold, and K. Hynynen, "Progress and problems in the application of focused ultrasound for blood-brain barrier disruption," Ultrasonics **48**, 279-296 (2008).

6. T. D. Azad, J. Pan, I. D. Connolly, A. Remington, C. M. Wilson, and G. A. Grant, "Therapeutic strategies to improve drug delivery across the blood-brain barrier," Neurosurg Focus **38**, E9 (2015).

7. E. M. Kemper, W. Boogerd, I. Thuis, J. H. Beijnen, and O. van Tellingen, "Modulation of the blood-brain barrier in oncology: therapeutic opportunities for the treatment of brain tumours?," Cancer Treat Rev **30**, 415-423 (2004).

8. T. Siegal, R. Rubinstein, F. Bokstein, A. Schwartz, A. Lossos, E. Shalom, R. Chisin, and J. M. Gomori, "In vivo assessment of the window of barrier opening after osmotic blood-brain barrier disruption in humans," J Neurosurg **92**, 599-605 (2000).

9. M. Aryal, C. D. Arvanitis, P. M. Alexander, and N. McDannold, "Ultrasound-mediated blood-brain barrier disruption for targeted drug delivery in the central nervous system," Adv Drug Deliv Rev **72**, 94-109 (2014).

10. H. Chen and E. E. Konofagou, "The size of blood-brain barrier opening induced by focused ultrasound is dictated by the acoustic pressure," J Cereb Blood Flow Metab **34**, 1197-1204 (2014).

11. K. Hynynen, N. McDannold, N. Vykhodtseva, and F. A. Jolesz, "Non-invasive opening of BBB by focused ultrasound," Acta Neurochir Suppl **86**, 555-558 (2003).

12. Y. S. Tung, F. Vlachos, J. A. Feshitan, M. A. Borden, and E. E. Konofagou, "The mechanism of interaction between focused ultrasound and microbubbles in blood-brain barrier opening in mice," J Acoust Soc Am **130**, 3059-3067 (2011).

13. R. Medel, S. J. Monteith, W. J. Elias, M. Eames, J. Snell, J. P. Sheehan, M. Wintermark, F. A. Jolesz, and N. F. Kassell, "Magnetic resonance-guided focused ultrasound surgery: Part 2: A review of current and future applications," Neurosurgery **71**, 755-763 (2012).

14. J. Jagannathan, N. T. Sanghvi, L. A. Crum, C. P. Yen, R. Medel, A. S. Dumont, J. P. Sheehan, L. Steiner, F. Jolesz, and N. F. Kassell, "High-intensity focused ultrasound surgery of the brain: part 1--A historical perspective with modern applications," Neurosurgery **64**, 201-210; discussion 210-201 (2009).

15. E. E. Konofagou, "Optimization of the ultrasound-induced blood-brain barrier opening," Theranostics **2**, 1223-1237 (2012).

16. J. Shin, C. Kong, J. S. Cho, J. Lee, C. S. Koh, M. S. Yoon, Y. C. Na, W. S. Chang, and J. W. Chang, "Focused ultrasound-mediated noninvasive blood-brain barrier modulation: preclinical examination of efficacy and safety in various sonication parameters," Neurosurg Focus **44**, E15 (2018).

17. T. Kobus, N. Vykhodtseva, M. Pilatou, Y. Zhang, and N. McDannold, "Safety Validation of Repeated Blood-Brain Barrier Disruption Using Focused Ultrasound," Ultrasound Med Biol **42**, 481-492 (2016).

18. J. H. Hwang, J. Tu, A. A. Brayman, T. J. Matula, and L. A. Crum, "Correlation between inertial cavitation dose and endothelial cell damage in vivo," Ultrasound Med Biol **32**, 1611-1619 (2006).

19. G. Samiotaki, F. Vlachos, Y. S. Tung, and E. E. Konofagou, "A quantitative pressure and microbubble-size dependence study of focused ultrasound-induced blood-brain barrier opening reversibility in vivo using MRI," Magn Reson Med **67**, 769-777 (2012).

20. J. J. Choi, M. Pernot, S. A. Small, and E. E. Konofagou, "Noninvasive, transcranial and localized opening of the blood-brain barrier using focused ultrasound in mice," Ultrasound Med Biol **33**, 95-104 (2007).

21. J. J. Choi, J. A. Feshitan, B. Baseri, S. Wang, Y. S. Tung, M. A. Borden, and E. E. Konofagou, "Microbubble-size dependence of focused ultrasound-induced blood-brain barrier opening in mice in vivo," IEEE Trans Biomed Eng **57**, 145-154 (2010).

22. N. McDannold, N. Vykhodtseva, and K. Hynynen, "Blood-brain barrier disruption induced by focused ultrasound and circulating preformed microbubbles appears to be characterized by the mechanical index," Ultrasound Med Biol **34**, 834-840 (2008).

23. M. A. O'Reilly, A. C. Waspe, M. Ganguly, and K. Hynynen, "Focused-ultrasound disruption of the blood-brain barrier using closely-timed short pulses: influence of sonication parameters and injection rate," Ultrasound Med Biol **37**, 587-594 (2011).

24. N. McDannold, N. Vykhodtseva, and K. Hynynen, "Effects of acoustic parameters and ultrasound contrast agent dose on focused-ultrasound induced blood-brain barrier disruption," Ultrasound Med Biol **34**, 930-937 (2008).

25. R. Chopra, N. Vykhodtseva, and K. Hynynen, "Influence of exposure time and pressure amplitude on blood-brain-barrier opening using transcranial ultrasound exposures," ACS Chem Neurosci **1**, 391-398 (2010).

26. C. Bing, Y. Hong, C. Hernandez, M. Rich, B. Cheng, I. Munaweera, D. Szczepanski, Y. Xi, M. Bolding, A. Exner, and R. Chopra, "Characterization of different bubble formulations for blood-brain barrier opening using a focused ultrasound system with acoustic feedback control," Scientific Reports **8**, 7986 (2018).

27. A. Carpentier, M. Canney, A. Vignot, V. Reina, K. Beccaria, C. Horodyckid, C. Karachi, D. Leclercq, C. Lafon, J. Y. Chapelon, L. Capelle, P. Cornu, M. Sanson, K. Hoang-Xuan, J. Y. Delattre, and A. Idbaih, "Clinical trial of blood-brain barrier disruption by pulsed ultrasound," Sci Transl Med **8**, 343re342 (2016).

28. N. Lipsman, S. Ironside, R. Alkins, A. Bethune, Y. Huang, J. Perry, A. Sahgal, M. Trudeau, K. Hynynen, and T. Mainprize, "SCDT-51. Initial experience of blood-brain barrier opening for chemotherapeutic-drug delivery to brain tumors by MR-guided focused ultrasound," Neuro-Oncology **19**, vi275-vi275 (2017).

29. S. Meairs and A. Alonso, "Ultrasound, microbubbles and the blood-brain barrier," Prog Biophys Mol Biol **93**, 354-362 (2007).

30. D. Y. Santiesteban, D. S. Dumani, D. Profili, and S. Y. Emelianov, "Copper Sulfide Perfluorocarbon Nanodroplets as Clinically Relevant Photoacoustic/Ultrasound Imaging Agents," Nano Lett **17**, 5984-5989 (2017).

31. T. L. Szabo, *Diagnostic Ultrasound Imaging: Inside Out* (Elsevier Academic Press, 2004).

32. H. Azhari, *Basics of Biomedical Ultrasound for Engineers* (Wiley, 2010).

33. E. G. Grant and E. M. White, "Pediatric neurosonography," J Child Neurol **1**, 319-337 (1986).

34. M. Riccabona, "Neurosonography in neonates, infants and children," in *Pediatric Ultrasound* (Springer, 2014), pp. 77-136.

35. K. Barlinn and A. V. Alexandrov, "Transcranial Doppler Sonography," in *Noninvasive Vascular Diagnosis: A Practical Guide to Therapy*, A. F. AbuRahma and D. F. Bandyk, eds. (Springer London, London, 2013), pp. 133-155.

36. A. J. Gardner, C. O. Tan, P. N. Ainslie, P. van Donkelaar, P. Stanwell, C. R. Levi, and G. L. Iverson, "Cerebrovascular reactivity assessed by transcranial Doppler ultrasound in sport-related concussion: a systematic review," Br J Sports Med **49**, 1050-1055 (2015).

37. J. D. Kirsch, M. Mathur, M. H. Johnson, G. Gowthaman, and L. M. Scoutt, "Advances in transcranial Doppler US: imaging ahead," Radiographics **33**, E1-E14 (2013).

38. M. Weber, P. Grolimund, and R. W. Seiler, "Evaluation of posttraumatic cerebral blood flow velocities by transcranial Doppler ultrasonography," Neurosurgery **27**, 106-112 (1990).

39. N. A. Martin, R. V. Patwardhan, M. J. Alexander, C. Z. Africk, J. H. Lee, E. Shalmon, D. A. Hovda, and D. P. Becker, "Characterization of cerebral hemodynamic phases following severe head trauma: hypoperfusion, hyperemia, and vasospasm," J Neurosurg **87**, 9-19 (1997).

40. M. Czosnyka, B. F. Matta, P. Smielewski, P. J. Kirkpatrick, and J. D. Pickard, "Cerebral perfusion pressure in head-injured patients: a noninvasive assessment using transcranial Doppler ultrasonography," J Neurosurg **88**, 802-808 (1998).

41. G. Kumar, R. B. Shahripour, and M. R. Harrigan, "Vasospasm on transcranial Doppler is predictive of delayed cerebral ischemia in aneurysmal subarachnoid hemorrhage: a systematic review and meta-analysis," Journal of Neurosurgery **124**, 1257-1264 (2016).

42. M. Belzberg, N. B. Shalom, E. Yuhanna, A. Manbachi, A. Tekes, J. Huang, H. Brem, and C. R. Gordon, "Sonolucent Cranial Implants: Cadaveric Study and Clinical Findings Supporting Diagnostic and Therapeutic Transcranioplasty Ultrasound," J Craniofac Surg **30**, 1456-1461 (2019).

43. E. Macé, G. Montaldo, I. Cohen, M. Baulac, M. Fink, and M. Tanter, "Functional ultrasound imaging of the brain," Nature Methods **8**, 662-664 (2011).

44. M. A. O'Reilly and K. Hynynen, "A super-resolution ultrasound method for brain vascular mapping," Med Phys **40**, 110701 (2013).

45. P. Beard, "Biomedical photoacoustic imaging," Interface focus, rsfs20110028 (2011).

46. V. Ntziachristos, J. Ripoll, L. V. Wang, and R. Weissleder, "Looking and listening to light: the evolution of whole-body photonic imaging," Nature biotechnology **23**, 313-320 (2005).

47. A. de la Zerda, "Photoacoustic Imaging: Development of Imaging Systems and Molecular Agents," in *Engineering in Translational Medicine*, W. Cai, ed. (Springer London, London, 2014), pp. 799-833.

48. R. Weissleder, "A clearer vision for in vivo imaging," Nature biotechnology **19**, 316-316 (2001).

49. A. M. Smith, M. C. Mancini, and S. Nie, "Bioimaging: Second window for in vivo imaging," Nat Nano **4**, 710-711 (2009).

50. H. F. Zhang, K. Maslov, G. Stoica, and L. V. Wang, "Functional photoacoustic microscopy for high-resolution and noninvasive in vivo imaging," Nature biotechnology **24**, 848-851 (2006).

51. L. V. Wang and S. Hu, "Photoacoustic tomography: in vivo imaging from organelles to organs," Science **335**, 1458-1462 (2012).

52. G. P. Luke, D. Yeager, and S. Y. Emelianov, "Biomedical applications of photoacoustic imaging with exogenous contrast agents," Ann. Biomed. Eng. **40**, 422-437 (2012).

53. N. P. Dana, Diego S. Dumani, Jason R. Cook, and Stanislav Emelianov, "Overview of Photoacoustic Imaging," in *Advances in Medical Physics*, J. V. D. Devon J. Godfrey, Shiva K. Das, Bruce H. Curran and Anthony B. Wolbarst, ed. (Medical Physics Publishing, Madison, WI, 2016), pp. 47-70.

54. M. Mehrmohammadi, S. Joon Yoon, D. Yeager, and S. Y Emelianov, "Photoacoustic imaging for cancer detection and staging," Current molecular imaging **2**, 89-105 (2013).

55. S. Mallidi, G. P. Luke, and S. Emelianov, "Photoacoustic imaging in cancer detection, diagnosis, and treatment guidance," Trends in biotechnology **29**, 213-221 (2011).

56. A. Taruttis and V. Ntziachristos, "Advances in real-time multispectral optoacoustic imaging and its applications," Nature Photonics **9**, 219-227 (2015).

57. M. Xu and L. V. Wang, "Photoacoustic imaging in biomedicine," Review of Scientific Instruments **77**, 041101 (2006).

58. J. Yao and L. V. Wang, "Photoacoustic Brain Imaging: from Microscopic to Macroscopic Scales," Neurophotonics **1**(2014).

59. J. Xia and L. V. Wang, "Photoacoustic Tomography of the Brain," in *Optical Methods and Instrumentation in Brain Imaging and Therapy*, S. J. Madsen, ed. (Springer New York, New York, NY, 2013), pp. 137-156.

60. S. Hu and L. V. Wang, "Neurovascular photoacoustic tomography," Front Neuroenergetics **2**, 10 (2010).

61. A. Ray, X. Wang, Y.-E. K. Lee, H. J. Hah, G. Kim, T. Chen, D. A. Orringer, O. Sagher, X. Liu, and R. Kopelman, "Targeted blue nanoparticles as photoacoustic contrast agent for brain tumor delineation," Nano Research **4**, 1163-1173 (2011).

62. M. Kneipp, J. Turner, H. Estrada, J. Rebling, S. Shoham, and D. Razansky, "Effects of the murine skull in optoacoustic brain microscopy," J Biophotonics **9**, 117-123 (2016).

63. E. W. Stein, K. Maslov, and L. V. Wang, "Noninvasive, in vivo imaging of blood-oxygenation dynamics within the mouse brain using photoacoustic microscopy," J Biomed Opt **14**, 020502 (2009).

64. J. Yao, J. Xia, K. I. Maslov, M. Nasiriavanaki, V. Tsytsarev, A. V. Demchenko, and L. V. Wang, "Noninvasive photoacoustic computed tomography of mouse brain metabolism in vivo," Neuroimage **64**, 257-266 (2013).

65. Q. Fan, K. Cheng, Z. Yang, R. Zhang, M. Yang, X. Hu, X. Ma, L. Bu, X. Lu, X. Xiong, W. Huang, H. Zhao, and Z. Cheng, "Perylene-diimide-based nanoparticles as highly efficient photoacoustic agents for deep brain tumor imaging in living mice," Adv Mater **27**, 843-847 (2015).

66. S. Hu, P. Yan, K. Maslov, J. M. Lee, and L. V. Wang, "Intravital imaging of amyloid plaques in a transgenic mouse model using optical-resolution photoacoustic microscopy," Opt Lett **34**, 3899-3901 (2009).

67. S. Y. Emelianov, P.-C. Li, and M. O'Donnell, "Photoacoustics for molecular imaging and therapy," Physics today **62**, 34 (2009).

68. J. Xia, J. Yao, and L. V. Wang, "Photoacoustic tomography: principles and advances," Electromagnetic waves (Cambridge, Mass.) **147**, 1 (2014).

69. P. S. Sheeran and P. A. Dayton, "Improving the performance of phase-change perfluorocarbon droplets for medical ultrasonography: current progress, challenges, and prospects," Scientifica (Cairo) **2014**, 579684 (2014).

70. N. Rapoport, "Drug-Loaded Perfluorocarbon Nanodroplets for Ultrasound-Mediated Drug Delivery," Adv Exp Med Biol **880**, 221-241 (2016).

71. H. Lea-Banks, M. A. O'Reilly, and K. Hynynen, "Ultrasound-responsive droplets for therapy: A review," J Control Release **293**, 144-154 (2019).

72. E. Strohm, M. Rui, I. Gorelikov, N. Matsuura, and M. Kolios, "Vaporization of perfluorocarbon droplets using optical irradiation," Biomed Opt Express **2**, 1432-1442 (2011).

73. P. S. Sheeran and P. A. Dayton, "Phase-change contrast agents for imaging and therapy," Curr Pharm Des **18**, 2152-2165 (2012).

74. H. Yoon, S. K. Yarmoska, A. S. Hannah, C. Yoon, K. A. Hallam, and S. Y. Emelianov, "Contrast-enhanced ultrasound imaging in vivo with laser-activated nanodroplets," Med Phys **44**, 3444-3449 (2017).

75. K. Wilson, K. Homan, and S. Emelianov, "Biomedical photoacoustics beyond thermal expansion using triggered nanodroplet vaporization for contrast-enhanced imaging," Nat Commun **3**, 618 (2012).

76. P. S. Sheeran, N. Matsuura, M. A. Borden, R. Williams, T. O. Matsunaga, P. N. Burns, and P. A. Dayton, "Methods of Generating Submicrometer Phase-Shift Perfluorocarbon Droplets for Applications in Medical Ultrasonography," IEEE Trans Ultrason Ferroelectr Freq Control **64**, 252-263 (2017).

77. K. C. Schad and K. Hynynen, "In vitro characterization of perfluorocarbon droplets for focused ultrasound therapy," Phys Med Biol **55**, 4933-4947 (2010).

78. P. A. Mountford, A. N. Thomas, and M. A. Borden, "Thermal activation of superheated lipid-coated perfluorocarbon drops," Langmuir **31**, 4627-4634 (2015).

79. N. Y. Rapoport, A. M. Kennedy, J. E. Shea, C. L. Scaife, and K. H. Nam, "Controlled and targeted tumor chemotherapy by ultrasound-activated nanoemulsions/microbubbles," J Control Release **138**, 268-276 (2009).

80. A. Hannah, G. Luke, K. Wilson, K. Homan, and S. Emelianov, "Indocyanine green-loaded photoacoustic nanodroplets: dual contrast nanoconstructs for enhanced photoacoustic and ultrasound imaging," ACS Nano **8**, 250-259 (2014).

81. R. K. Hartman, K. A. Hallam, E. M. Donnelly, and S. Y. Emelianov, "Photoacoustic imaging of gold nanorods in the brain delivered via microbubble-assisted focused ultrasound: a tool for in vivo molecular neuroimaging," Laser Physics Letters **16**, 025603 (2019).

82. D. Y. Santiesteban, K. A. Hallam, S. K. Yarmoska, and S. Y. Emelianov, "Color-coded perfluorocarbon nanodroplets for multiplexed ultrasound and photoacoustic imaging," Nano Research (2019).

83. C. Y. Lin and W. G. Pitt, "Acoustic droplet vaporization in biology and medicine," Biomed Res Int **2013**, 404361 (2013).

84. K. A. Hallam, E. M. Donnelly, A. B. Karpiouk, R. K. Hartman, and S. Y. Emelianov, "Laser-activated perfluorocarbon nanodroplets: a new tool for blood brain barrier opening," Biomed Opt Express **9**, 4527-4538 (2018).

85. A. S. Hannah, G. P. Luke, and S. Y. Emelianov, "Blinking Phase-Change Nanocapsules Enable Background-Free Ultrasound Imaging," Theranostics **6**, 1866-1876 (2016).

86. A. S. Hannah, D. VanderLaan, Y. S. Chen, and S. Y. Emelianov, "Photoacoustic and ultrasound imaging using dual contrast perfluorocarbon nanodroplets triggered by laser pulses at 1064 nm," Biomed Opt Express **5**, 3042-3052 (2014).

87. D. S. Li, S. Schneewind, M. Bruce, Z. Khaing, M. O'Donnell, and L. Pozzo, "Spontaneous Nucleation of Stable Perfluorocarbon Emulsions for Ultrasound Contrast Agents," Nano Lett **19**, 173-181 (2019).

88. J. D. Dove, P. A. Mountford, T. W. Murray, and M. A. Borden, "Engineering optically triggered droplets for photoacoustic imaging and therapy," Biomed Opt Express **5**, 4417-4427 (2014).

89. P. S. Sheeran, J. E. Streeter, L. B. Mullin, T. O. Matsunaga, and P. A. Dayton, "Toward ultrasound molecular imaging with phase-change contrast agents: an in vitro proof of principle," Ultrasound Med Biol **39**, 893-902 (2013).

90. G. P. Luke, A. S. Hannah, and S. Y. Emelianov, "Super-Resolution Ultrasound Imaging in Vivo with Transient Laser-Activated Nanodroplets," Nano Letters **16**, 2556-2559 (2016).

91. H. Yoon, Hallam, K.A., Yoon, C. and Emelianov, S.Y., "Super-resolution imaging with ultrafast ultrasound imaging of optically triggered perfluorohexane nanodroplets," IEEE Transactions on Ultrasonics, Ferroelectrics, and Frequency Control. (2018).

92. E. C. Unger, T. Porter, W. Culp, R. Labell, T. Matsunaga, and R. Zutshi, "Therapeutic applications of lipid-coated microbubbles," Advanced drug delivery reviews **56**, 1291-1314 (2004).

93. N. Rapoport, A. Marin, Y. Luo, G. D. Prestwich, and M. Muniruzzaman, "Intracellular uptake and trafficking of Pluronic micelles in drug-sensitive and MDR cells: Effect on the intracellular drug localization," Journal of pharmaceutical sciences **91**, 157-170 (2002).

94. J. G. Riess, "Oxygen Carriers ("Blood Substitutes") Raison d'Etre, Chemistry, and Some Physiology Blut ist ein ganz besondrer Saft 1," Chemical Reviews **101**, 2797-2920 (2001).

95. J. G. Riess, "Understanding the fundamentals of perfluorocarbons and perfluorocarbon emulsions relevant to in vivo oxygen delivery," Artificial cells, blood substitutes, and biotechnology **33**, 47-63 (2005).

96. C. C. Chen, P. S. Sheeran, S. Y. Wu, O. O. Olumolade, P. A. Dayton, and E. E. Konofagou, "Targeted drug delivery with focused ultrasound-induced blood-brain barrier opening using acoustically-activated nanodroplets," J Control Release **172**, 795-804 (2013).

97. C. Poon, D. McMahon, and K. Hynynen, "Noninvasive and targeted delivery of therapeutics to the brain using focused ultrasound," Neuropharmacology **120**, 20-37 (2017).

98. N. Sheikov, N. McDannold, N. Vykhodtseva, F. Jolesz, and K. Hynynen, "Cellular mechanisms of the blood-brain barrier opening induced by ultrasound in presence of microbubbles," Ultrasound Med Biol **30**, 979-989 (2004).

99. N. Lipsman, S. Ironside, R. Alkins, A. Bethune, Y. Huang, J. Perry, A. Sahgal, M. Trudeau, K. Hynynen, and T. Mainprize, "SCDT-51. INITIAL EXPERIENCE OF BLOOD-BRAIN BARRIER OPENING FOR CHEMOTHERAPEUTIC-DRUG DELIVERY TO BRAIN TUMOURS BY MR-GUIDED FOCUSED ULTRASOUND," Neuro-Oncology **19**, vi275-vi275 (2017).

100. S. Y. Wu, S. M. Fix, C. B. Arena, C. C. Chen, W. Zheng, O. O. Olumolade, V. Papadopoulou, A. Novell, P. A. Dayton, and E. E. Konofagou, "Focused ultrasound-facilitated brain drug delivery using optimized nanodroplets: vaporization efficiency dictates large molecular delivery," Phys Med Biol **63**, 035002 (2018).

101. F.-Y. Yang, W.-M. Fu, R.-S. Yang, H.-C. Liou, K.-H. Kang, and W.-L. Lin, "Quantitative Evaluation of Focused Ultrasound with a Contrast Agent on Blood-Brain Barrier Disruption," Ultrasound in Medicine & Biology **33**, 1421-1427 (2007).

102. N. McDannold, N. Vykhodtseva, and K. Hynynen, "Use of ultrasound pulses combined with Definity for targeted blood-brain barrier disruption: a feasibility study," Ultrasound Med Biol **33**, 584-590 (2007).

103. Y. H. Tan, M. Liu, B. Nolting, J. G. Go, J. Gervay-Hague, and G. Y. Liu, "A nanoengineering approach for investigation and regulation of protein immobilization," ACS Nano **2**, 2374-2384 (2008).

104. K. Namdee, M. Carrasco-Teja, M. B. Fish, P. Charoenphol, and O. Eniola-Adefeso, "Effect of variation in hemorheology between human and animal blood on the binding efficacy of vascular-targeted carriers," Sci Rep **5**, 11631 (2015).

105. A. Roggan, M. Friebel, K. Do Rschel, A. Hahn, and G. Mu Ller, "Optical Properties of Circulating Human Blood in the Wavelength Range 400-2500 nm," J Biomed Opt **4**, 36-46 (1999).

106. A. H. Payne, G. W. Hawryluk, Y. Anzai, H. Odeen, M. A. Ostlie, E. C. Reichert, A. J. Stump, S. Minoshima, and D. J. Cross, "Magnetic resonance imaging-guided focused ultrasound to increase localized blood-spinal cord barrier permeability," Neural Regen Res **12**, 2045-2049 (2017).

107. M. Seo, R. Williams, and N. Matsuura, "Size reduction of cosolvent-infused microbubbles to form acoustically responsive monodisperse perfluorocarbon nanodroplets," Lab Chip **15**, 3581-3590 (2015).

108. W. M. Pardridge, "The blood-brain barrier: bottleneck in brain drug development," NeuroRx **2**, 3-14 (2005).

109. U. Tosi, C. S. Marnell, R. Chang, W. C. Cho, R. Ting, U. B. Maachani, and M. M. Souweidane, "Advances in Molecular Imaging of Locally Delivered Targeted Therapeutics for Central Nervous System Tumors," Int J Mol Sci **18**(2017).

110. S. K. Yarmoska, H. Yoon, and S. Y. Emelianov, "Lipid Shell Composition Plays a Critical Role in the Stable Size Reduction of Perfluorocarbon Nanodroplets," Ultrasound Med Biol **45**, 1489-1499 (2019).

111. S. L. Jacques, "Optical properties of biological tissues: a review," Phys Med Biol **58**, R37-61 (2013).

112. K. A. Hallam and S. Y. Emelianov, "Toward optimization of blood brain barrier opening induced by laser-activated perfluorocarbon nanodroplets," Biomed Opt Express **10**, 3139-3151 (2019).

113. H. M. Grey, J. W. Hirst, and M. Cohn, "A new mouse immunoglobulin: IgG3 " The Journal of Experimental Medicine **133**, 289 (1971).

114. P. H. Wang, H. L. Liu, P. H. Hsu, C. Y. Lin, C. R. Wang, P. Y. Chen, K. C. Wei, T. C. Yen, and M. L. Li, "Gold-nanorod contrast-enhanced photoacoustic micro-imaging of focused-ultrasound induced blood-brain-barrier opening in a rat model," J Biomed Opt **17**, 061222 (2012).

115. G. P. Luke, D. Yeager, and S. Y. Emelianov, "Biomedical applications of photoacoustic imaging with exogenous contrast agents," Ann Biomed Eng **40**, 422-437 (2012).

116. J. Tang, J. E. Coleman, X. Dai, and H. Jiang, "Wearable 3-D Photoacoustic Tomography for Functional Brain Imaging in Behaving Rats," Sci Rep **6**, 25470 (2016).

117. J. Tang, L. Xi, J. Zhou, H. Huang, T. Zhang, P. R. Carney, and H. Jiang, "Noninvasive high-speed photoacoustic tomography of cerebral hemodynamics in awake-moving rats," J Cereb Blood Flow Metab **35**, 1224-1232 (2015).

118. Y.-S. Chen, W. Frey, S. Kim, K. Homan, P. Kruizinga, K. Sokolov, and S. Emelianov, "Enhanced thermal stability of silica-coated gold nanorods for photoacoustic imaging and image-guided therapy," Optics express **18**, 8867-8878 (2010).

119. M. Zhou, R. Zhang, M. Huang, W. Lu, S. Song, M. P. Melancon, M. Tian, D. Liang, and C. Li, "A chelator-free multifunctional [64Cu] CuS nanoparticle platform for simultaneous micro-PET/CT imaging and photothermal ablation therapy," Journal of the American Chemical Society **132**, 15351-15358 (2010).

120. Y. Li, W. Lu, Q. Huang, C. Li, and W. Chen, "Copper sulfide nanoparticles for photothermal ablation of tumor cells," Nanomedicine **5**, 1161-1171 (2010).

121. L. Guo, I. Panderi, D. D. Yan, K. Szulak, Y. Li, Y.-T. Chen, H. Ma, D. B. Niesen, N. Seeram, and A. Ahmed, "A comparative study of hollow copper sulfide nanoparticles and hollow gold nanospheres on degradability and toxicity," ACS nano **7**, 8780-8793 (2013).

122. E. Chung, S. Y. Nam, L. M. Ricles, S. Y. Emelianov, and L. J. Suggs, "Evaluation of gold nanotracers to track adipose-derived stem cells in a PEGylated fibrin gel for dermal tissue engineering applications," Int J Nanomedicine **8**, 325-336 (2013).

123. E. M. Donnelly, K. P. Kubelick, D. S. Dumani, and S. Y. Emelianov, "Photoacoustic Image-Guided Delivery of Plasmonic-Nanoparticle-Labeled Mesenchymal Stem Cells to the Spinal Cord," Nano Lett **18**, 6625-6632 (2018).

124. S. Y. Nam, L. M. Ricles, L. J. Suggs, and S. Y. Emelianov, "Nonlinear photoacoustic signal increase from endocytosis of gold nanoparticles," Opt Lett **37**, 4708-4710 (2012).

125. S. Y. Nam, L. M. Ricles, L. J. Suggs, and S. Y. Emelianov, "In vivo ultrasound and photoacoustic monitoring of mesenchymal stem cells labeled with gold nanotracers," PLoS One **7**, e37267 (2012).

126. M. E. Lull and M. L. Block, "Microglial activation and chronic neurodegeneration," Neurotherapeutics **7**, 354-365 (2010).

127. A. Henn, S. Lund, M. Hedtjarn, A. Schrattenholz, P. Porzgen, and M. Leist, "The suitability of BV2 cells as alternative model system for primary microglia cultures or for animal experiments examining brain inflammation," ALTEX **26**, 83-94 (2009).

128. H. H. Gustafson, D. Holt-Casper, D. W. Grainger, and H. Ghandehari, "Nanoparticle Uptake: The Phagocyte Problem," Nano Today **10**, 487-510 (2015).

129. B. Stansley, J. Post, and K. Hensley, "A comparative review of cell culture systems for the study of microglial biology in Alzheimer's disease," J Neuroinflammation **9**, 115 (2012).

130. G. Ku, M. Zhou, S. Song, Q. Huang, J. Hazle, and C. Li, "Copper sulfide nanoparticles as a new class of photoacoustic contrast agent for deep tissue imaging at 1064 nm," ACS Nano **6**, 7489-7496 (2012).

131. E. Frohlich, "The role of surface charge in cellular uptake and cytotoxicity of medical nanoparticles," Int J Nanomedicine **7**, 5577-5591 (2012).

132. R. Fu, Q. Shen, P. Xu, J. J. Luo, and Y. Tang, "Phagocytosis of microglia in the central nervous system diseases," Mol Neurobiol **49**, 1422-1434 (2014).

133. R. J. Gush, T. A. King, and M. I. Jayson, "Aspects of laser light scattering from skin tissue with application to laser Doppler blood flow measurement," Phys Med Biol **29**, 1463-1476 (1984).

134. J. Su, A. Karpiouk, B. Wang, and S. Emelianov, "Photoacoustic imaging of clinical metal needles in tissue," J Biomed Opt **15**, 021309 (2010).

135. B. Arnal, C. Perez, C. W. Wei, J. Xia, M. Lombardo, I. Pelivanov, T. J. Matula, L. D. Pozzo, and M. O'Donnell, "Sono-photoacoustic imaging of gold nanoemulsions: Part I. Exposure thresholds," Photoacoustics **3**, 3-10 (2015).

136. B. Arnal, C. W. Wei, C. Perez, T. M. Nguyen, M. Lombardo, I. Pelivanov, L. D. Pozzo, and M. O'Donnell, "Sono-photoacoustic imaging of gold nanoemulsions: Part II. Real time imaging," Photoacoustics **3**, 11-19 (2015).

137. D. McMahon and K. Hynynen, "Acute Inflammatory Response Following Increased Blood-Brain Barrier Permeability Induced by Focused Ultrasound is Dependent on Microbubble Dose," Theranostics **7**, 3989-4000 (2017).

138. H. D. Liang, J. Tang, and M. Halliwell, "Sonoporation, drug delivery, and gene therapy," Proc Inst Mech Eng H **224**, 343-361 (2010).

139. J. A. St George, "Gene therapy progress and prospects: adenoviral vectors," Gene Ther **10**, 1135-1141 (2003).

140. H. Yoon, Y. I. Zhu, S. K. Yarmoska, and S. Y. Emelianov, "Design and Demonstration of a Configurable Imaging Platform for Combined Laser, Ultrasound, and Elasticity Imaging," IEEE Trans Med Imaging **38**, 1622-1632 (2019).

141. A. Alzheimer's, "2015 Alzheimer's disease facts and figures," Alzheimers Dement **11**, 332-384 (2015).

142. D. K. Lahiri, M. R. Farlow, K. Sambamurti, N. H. Greig, E. Giacobini, and L. S. Schneider, "A critical analysis of new molecular targets and strategies for drug developments in Alzheimer's disease," Curr Drug Targets **4**, 97-112 (2003).

143. J. M. Tarasoff-Conway, R. O. Carare, R. S. Osorio, L. Glodzik, T. Butler, E. Fieremans, L. Axel, H. Rusinek, C. Nicholson, B. V. Zlokovic, B. Frangione, K. Blennow, J. Menard, H. Zetterberg, T. Wisniewski, and M. J. de Leon, "Clearance systems in the brain-implications for Alzheimer disease," Nat Rev Neurol **11**, 457-470 (2015).

144. S. Kim, Y. S. Chen, G. P. Luke, and S. Y. Emelianov, "In vivo three-dimensional spectroscopic photoacoustic imaging for monitoring nanoparticle delivery," Biomed Opt Express **2**, 2540-2550 (2011).